UNIVERSITÀ DEGLI STUDI DI MILANO

FACOLTÀ DI SCIENZE E TECNOLOGIE

Dipartimento di Chimica

PhD School in Chemistry - Cycle XXVI

From Synthesis to Application: Porphyrins as Versatile Compounds in Energy, Sensing, and Catalysis

PhD Candidate: Cecilia ALBANESE

R13119

Tutor: prof. Francesca TESSORE

Co-tutor: prof. Gabriele DI CARLO

Director of the School: prof. Daniele PASSARELLA

Academic Year 2022-2023

THIS PAGE IS INTERNATIONALLY LEFT BLANC

TABLE OF CONTENTS

PORPHYRINS: A GENERAL INTRODUCTION

Porphyrins are a unique class of heterocyclic tetrapyrrolic organic compounds which represent the most ubiquitous compounds found in nature. These macrocycles derive their name from "*porphura*" which was used for the first time by ancient Greeks for the intense purple colour.[1] From a structural perspective, a porphyrin consists of four pyrrolic units interconnected in a coplanar manner through four methene bridges (=CH−), resulting in a flat macrocyclic configuration. This molecular structure possesses an extensive conjugated system of 18 π-electrons, responsible for its aromatic properties. Furthermore, its central cavity can accommodate sizable metal cations, with a maximum core cavity diameter of approximately 3.7 *Å*. During metal coordination, two protons are extracted from the nitrogen atoms in the pyrrole rings, resulting in the formation of two negative charges.[2] Notably, porphyrin complexes with transition metal ions exhibit exceptional stability. Furthermore, they can be effectively modified to finely adjust their electronic proprieties, thanks to the availability of four *meso*, eight β-*pyrrolic*, and up to two *axial* positions for functionalization (*figure 1*).[3]
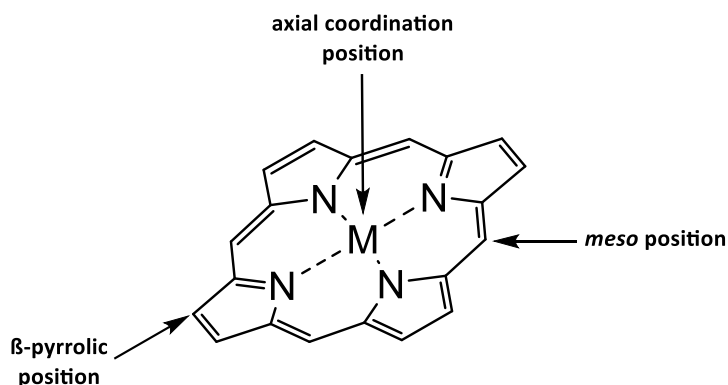
Figure 1: *porphyrin's functionalizable positions*

Characterization

Porphyrin-based compounds exhibit vivid colours ranging from red to green, their colouring is influenced by the presence of a metal ion, the surrounding environment or solvent, and the degree of functionalization. This striking coloration arises from strong absorption within the visible spectrum. Consequently, UV-Vis absorption spectroscopy is a fundamental tool to study the light harvesting properties and the energy levels of

these compounds. *Figure 2* displays the absorption spectra of a generic porphyrin, presented in both its free base and metal complex forms.
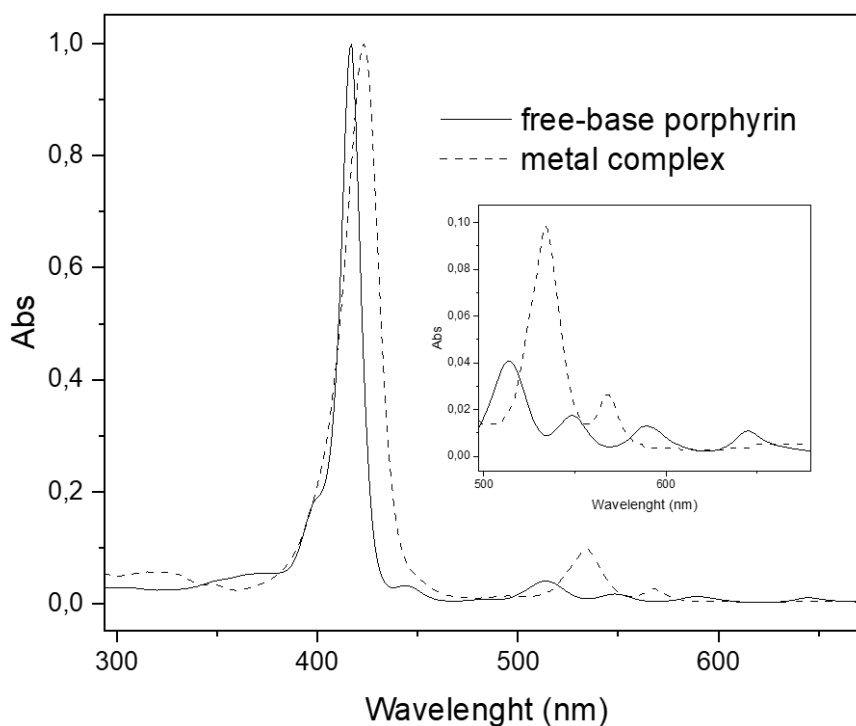
Figure 2: absorption spectra of a generic free-base porphyrin and his metal complex, with enlargement on Q bands region

Typically, the spectra exhibit a prominent Soret or B band at wavelengths ranging from approximately 400 to 500 nm, characterized by a high extinction coefficient (ε = 105 M^{-1} cm^{-1}) for both the free base and metal complex. Additionally, there are one or more broader and less intense Q bands (ε = 104 M^{-1} cm^{-1}) observed at longer wavelengths (500-600 *nm*). Specifically, free base porphyrins commonly exhibit four distinct Q bands, which tend to merge into two upon metalation of the porphyrin (see enlargement of *figure 2)*. This absorption pattern has been clarified by the introduction of the so-called "four orbital model" proposed by M. Gouterman at the beginning of the '60s.[4] According to this model, the B and the Q bands depend on the transition of two HOMOs (*Highest Occupied Molecular Orbitals*) and two LUMOs (*Lowest Unoccupied Molecular Orbitals*) energy levels calculated by the Hückel theory. The HOMOs are two accidentally degenerate orbitals with $a_{1u}(\pi)$ and $a_{2u}(\pi)$ symmetry and an electronic density mainly located on the *meso*-positions and on the nitrogen atoms of the ring, whilst the LUMOs are a double degenerate orbital with $e_g(\pi^*)$ symmetry and an electron density on the β-*pyrrolic* and *meso*-positions (*figure 3*).
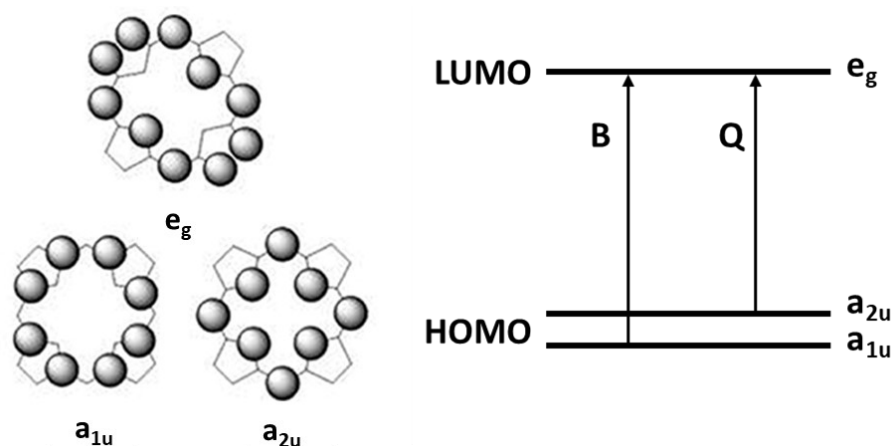
Figure 3: HOMO and LUMO orbitals according to the ''four orbital model'' of Gouterman [5]

The electronic configuration of the ground state is $(a_{1u})^2(a_{2u})^2$, yielding a singlet ground state (S_0). The lowest excited state configurations are $(a_{1u})^2(a_{2u})^1(e_g)^1$ and $(a_{1u})^1(a_{2u})^2(e_g)^1$, giving rise to singlet and triplet excited states. The electronic transitions between the HOMO and LUMO orbitals produce then two excited states. The B or Soret band, with higher energy state and higher oscillator strength, is strongly allowed and can be indicated as the $S_0 \rightarrow S_2$ transition (from the ground state to the second excited state), whereas the Q bands, with a lower energy and oscillator strength, are weakly allowed and can be indicated as the $S_0 \rightarrow S_1$ transition (from the ground state to the first excited state). [5] Aside from UV-Visible methods, the HOMO-LUMO energy gap can be deduced using DFT (*Density Functional Theory*) and TDDFT (*Time-Dependent Density Functional Theory*) calculations or by electrochemical measurements. The electrochemical behaviour of porphyrins typically involves two oxidation and two reduction processes. In these processes, one electron is successively removed or added to the π system of the molecule. Specifically, the HOMO energy level corresponds to the first oxidation process, while the LUMO corresponds to the initial reduction process that is observed.[5] These approaches offer insights into the redox characteristics of molecules by determining both ground-state and excited-state oxidation potentials. A profound understanding of the HOMO-LUMO gap in porphyrins facilitates precise chemical adjustments when incorporating peripheral substituents and conducting various structural adjustments. This characteristic makes porphyrins exceptionally suitable for numerous applications: diseases treatment and biological imaging,[6] sensors,[7] catalysis and photocatalysis,[8,9] nonlinear optics (NLO)[10], molecular photovoltaics[11] and fuel cells.[12]

Synthesis of the Tetrapyrrolic Core

In view of the high interest in these compounds, substantial efforts have been dedicated to the synthesis of artificial porphyrins.[13] Traditional synthetic routes are typically employed on a small (milligram) scale. The initial synthetic method for porphyrin production was suggested by Rothemund et al., which involved a reaction between pyrrole and aldehyde in pyridine within a sealed tube at 220°C. Nevertheless, the reaction yielded a mere 5% in the case of *meso*-tetraphenylporphyrin. [14] The most employed methods today include: (i) The Adler-Longo process, a one-step procedure utilizing acetic or propionic acid as a solvent under aerobic conditions at approximately 141°C[15] yielding the desired porphyrin in the range of 10-30% [15]; (ii) Lindsey's one-flask two-step methodology, which has proven highly effective in synthesizing a wide variety of porphyrin derivatives with yields ranging from 10% to 60%.[16,17] The primary challenges hindering the broad adoption of these methodologies regard the generation of undesirable by-products, including aldehyde-pyrrole oligocondensates and polypyrroles. These by-products not only diminish reaction yields, but also add complexity to the purification step.[13] Additionally, the Lindsay method depends on chlorinated solvents and necessitates the use of 2,3-dichloro-5,6-dicyanobenzoquinone (DDQ), which can produce highly toxic hydrogen cyanide (HCN) upon contact with water. The methods discussed above have mainly been used for producing symmetric A_4-porphyrins with four identical phenyl groups at the 5,10,15, 20 *meso* positions of the macrocycle. Complexity arises when attempting to synthesize *trans*-A_2B_2-porphyrins. These compounds are typically formed via a MacDonald-type [2 + 2] condensation reaction.[18] Yet, a significant challenge here is the tendency to yield a mixture of various porphyrin derivatives instead of the intended product, complicating subsequent purification. In recent years, there have been endeavours to improve *meso*-arylporphyrin synthesis efficiency and scalability. Strategies encompass cleaner processes by replacing conventional organic solvents with ionic liquids and supercritical water, increasing yields via solid microporous catalysts and microwave irradiation, and reducing energy consumption by shortening reaction times.[19] Once synthetized, the porphyrinic core can undergo further changes, such as coordinating a metal ion at the core centre, modifying

phenyl groups in the *meso*-positions, introducing functional groups into the β-positions, or coordinating axial ligands (*figure 4*).
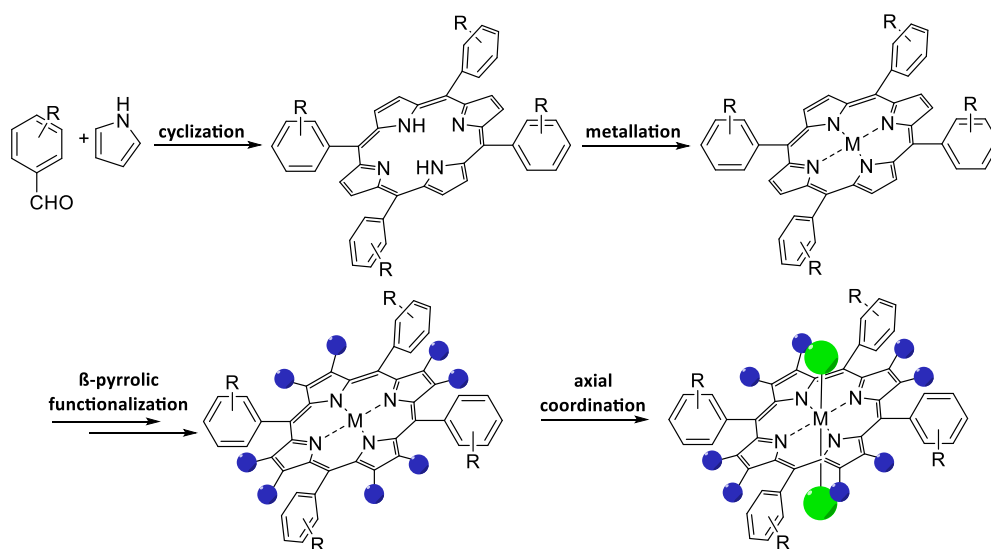
Figure 4*: multistep porphyrin synthesis*

These steps are integral to a carefully designed, multistep process for creating a macrocycle with finely tuned electronic, chemical, and/or physical characteristics in view of a specific application. Consequently, porphyrin synthesis is inherently intricate, but meticulously orchestrate.

PROJECT OVERVIEW

Throughout my three-year PhD program, I delved deeply into the world of porphyrin synthesis. The SunLab group, renowned for its expertise in this field, provided an invaluable environment. During my time with it, my main focus was on the systematic design, synthesis, and characterization of innovative porphyrin-based compounds for applications across various pivotal fields, as previously mentioned. In the initial phase of my PhD research, I centred my work on the synthesis of perfluorinated porphyrins characterized by a unique structure that exhibited enhanced charge-transfer properties due to the incorporation of donor groups. The objective was to create compounds that could function as a *push-pull* system with improved charge separation capabilities, making them suitable as sensitizers in Dye-Sensitized Photoelectrochemical Cells (DSPEC). After optimizing the synthetic procedure, we obtained the desired compounds with a good yield. Subsequently, we focused on their comprehensive characterization and performance evaluation as sensitizers in collaboration with Professor Caramori from University of Ferrara. Given the inherent hydrophobic nature resulting from the perfluorinated structure, we also considered potential applications for these compounds where the influence of water needed to be minimized, such as in chemiresistive sensors designed to detect volatile organic compounds (VOCs). This line of thinking led to a collaboration with Professor Cappelletti's group at the University of Milan, which is currently engaged in developing sensors for VOCs detection. We partnered with them to assess and compare the performance of our compounds when coupled with SnO_2 in chemiresistive sensors designed for the detection of acetone at mild temperatures under UV light. Furthermore, during my second year of PhD, I also had the valuable opportunity to spend six months in the *Laboratoire d'Electrochimie Molèculaire*, *Université Paris Cité*, under the guidance of professor M. Robert and doctor C. Fave. This experience allowed me to examine in deep another application area of porphyrin: electrocatalysis. Professor Robert is a prominent expert in the field of electrochemistry and one of his research focuses is the development of new catalysts capable of electrochemically convert CO_2 into valuable products, like CO, CH_4, CH_3OH. During my time there I synthetized, characterized, and subsequently evaluated a novel series of iron porphyrins specifically designed to enhance their catalytical performances in CO_2 reduction. The approach we

aimed to employ for achieving this enhancement, considering the strong experience of doctor Fave in this field, involves exploiting halogen bonding interactions, which we believed could facilitate the interaction between CO_2 and the porphyrin catalyst. Finally, the SunLab group possesses a significant expertise in the preparation and characterization of porphyrins for second order Nonlinear Optics (NLO). Indeed, the Department of Chemistry is equipped with an experimental apparatus able to measure the second order NLO molecular response by the Electric Field Induced Second Harmonic generation (EFISH) technique, providing us with the capability to characterize compounds exhibiting an intense *push-pull* configuration from this perspective as well. In the forthcoming sections of this thesis, I will then try to provide in a comprehensive exploration of the three-year endeavour, which has been divided into four primary sections, corresponding to the application of the synthesized porphyrins:

i) **Porphyrins for Dye-Sensitized Photo-Electrochemical Cells (DSPEC) Applications**: this section will delve into the word of Dye-Sensitized Photo-Electrochemical Cells, analysing design and structure-optimization strategies that permits to tailor an effective sensitizer. The core of this section will be the optimization of the synthetic routes to obtain the desired sensitizers, followed by their characterization and application in DSPEC devices.

ii) **Porphyrins in Chemiresistive Gas Sensors**: the subsequent section will centre on the utilization of porphyrins, originally designed for DSPEC application, in sensor technologies, elucidating their role in augmenting sensor response in order to apply them in mild (ambient) conditions. A mechanism of sensing supported by theoretical calculation is also proposed.

iii) **Porphyrins as Catalysts for CO_2 Reduction**: the third part of this thesis will revolve around the pivotal role played by porphyrins as catalysts in CO_2 reduction, highlighting the role of halogen bond as *through-space* interaction.

iv) **Porphyrins for Second Order NLO:** in the concluding section of the thesis, we will delve into the investigation of two novel hybrid materials comprising Graphene Nanoplates and Zn(II) porphyrins for their NLO properties. This segment relies on the combination of experimental data through the EFISH technique and DFT calculations, with the aim to unravel the characteristics of a prospective new nonlinear material.

SECTION I

PORPHYRINS FOR DSPEC

1.1| THE DSPEC TECHNOLOGY

1.1.1 The Current Energy Problem

Contemporary society relies on energy consumption, which represents a crucial factor in advancing the society development. However, this energy usage is intricately related to environmental challenges, as nearly every aspect of energy production, transportation, and consumption carries substantial ecological issues. The predominant issue that dominates the public concern regarding energy is undeniably climate change. Climate change refers to long-term shifts in temperatures and weather patterns. Natural shifts can occur due to variations in solar activity or significant volcanic eruptions. However, since the 1800s, human activities, primarily the burning of fossil fuels like coal, oil, and gas, have become the primary driver of climate change. This has led to greenhouse gas emissions, causing global warming at an unprecedented rate over the past two millennia. With a $1.5°C$ increase in global temperatures, we can expect more frequent heatwaves, longer warm seasons, and shorter cold seasons. At $2°C$ of global warming, heat extremes are likely to surpass critical thresholds for agriculture and public health. Yet, the impacts go beyond temperature. Climate change brings a multitude of regional changes that intensify with further warming, including more intense rainfall and consequent flooding, alterations in monsoon patterns, rising sea levels leading to increased coastal flooding and erosion in low-lying areas, diminished seasonal snow cover, glacier and ice sheet melting, loss of summer Arctic Sea ice, and ocean acidification. These changes affect entire ecosystems and the people that rely on them. However, strong and sustained reductions in emissions of CO_2 and other greenhouse gases would limit climate change.[20–22]

1.1.2 Solar Energy and Photovoltaic (PV)

Sunlight is our ultimate energy source. Sunlight is abundant, inexhaustible (considering that the Sun will last for more than 4 billion *years*), and fairly well distributed over the planet. The rate of energy consumption of our civilization (22.8 *TWh in 2019)* is almost four orders of magnitude smaller than the solar energy irradiating the surface of the Earth.[23,24] However, solar energy in order to be effectively used, needs to be transformed into other energy forms as heat, electricity, and other fuels.

Photovoltaics (PV) gets its name from the process of converting light (photons) to electricity (voltage), which is called the PV effect. The PV effect was first reported by Alexandre Edmond Becquerel in 1839, who observed the generation of an electric current by a silver coated platinum electrode immersed in an electrolyte solution. In the last 15 *years*, solar cell production has grown at about 30% per annum.[25] The conventional solar cells, as known as first-generation solar cells, are based on silicon. The production cost is highly dependent on the price of the silicon material, and China is now the world leader in producing crystalline silicon (c-Si) based PV cells and modules. Second-generation solar cells employ thin film technologies, offering easier production, cost reduction, versatile applications, and aesthetics. Drawbacks include material toxicity, limited abundance, temperature-dependent efficiency, and moderate light tolerance. Both generations are based on a p-n junction in a doped semiconductor enabling electron-hole movement generated by incident light. Third-generation photovoltaics maintain thin-film semiconductor deposition, featuring an organic sensitizer which absorbs solar radiation, exciting electrons and injecting them into the semiconductor, converting solar energy into electrical current.[25,26] Among the different types of third-generation solar cells, the most renowned are Dye-Sensitized Solar Cells (DSSCs). In fact, since the publication of the fist paper by Grätzel in 1991,[27] DSSCs appeared to be very promising for building integrated photovoltaics (BiPVs). DSSCs are transparent devices with tuneable colours which can be applied as ''smart" windows in PV glasses integrated to the building facades. *Figure 5* shows the scheme of a DSSC.[28]
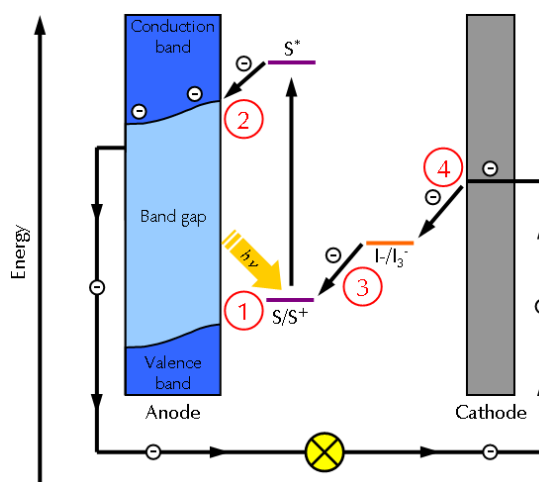
Figure 5: *schematic representation of a DSSC*

The functioning of a Dye-Sensitized Solar Cell can be summarised as follows:[29]

- STEP 1: The dye molecule is initially in its ground state (S). The semiconductor material of the anode is at this energy level (near the valence band) non-conductive. When light shines on the cell, dye molecules get excited from their ground state to a higher energy state (S*). The excited dye molecule has now a higher energy content and overcomes the band gap of the semiconductor.

- STEP 2: The excited dye molecule (S*) is oxidized to S^+ and an electron is injected into the conduction band of the semiconductor. Electrons can now move freely as the semiconductor is conductive at this energy level. Electrons are then transported to the current collector of the anode via diffusion processes. An electrical load can be powered if connected.

- STEP 3: The oxidized dye molecule (S^+) is again regenerated by electron donation from the iodide in the electrolyte to form again S species. Iodide is converted to triiodide.

- STEP 4: In return, iodide is regenerated by reduction of triiodide on the cathode and the circuit is closed.

1.1.3 Artificial Photosynthesis and Solar Fuels Production

A primary limitation of harnessing solar energy directly is linked to the intermittent nature of sunlight, with only approximately 6 *hours* of usable input on average each day.[30] To establish solar energy as a dependable energy source, the incorporation of advanced energy storage technologies that surpass the capabilities of current battery technologies is mandatory.[31] In nature, energy conversion and storage occur during natural photosynthesis, the solar-driven reduction of CO_2 by water. As shown in *eq. 1*, in green plants, the products are carbohydrates and oxygen.[30]

$$6H_2O + 6CO_2 + 48h\nu \rightarrow C_6H_{12}O_6 + 6O_2 \tag{1}$$
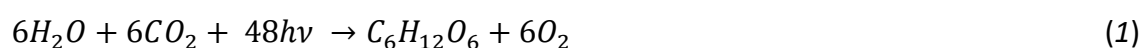
The objective of artificial photosynthesis aligns with that of natural photosynthesis: the transformation of solar energy into chemical reactions, resulting in the formation of high-energy compounds, the so called "solar fuels", where the energy is stored within

the chemical bonds. Solar fuels production includes process like water splitting for the generation of hydrogen (*eq. 2*) or the production of reduced carbon-based compounds, like CH_4, CH_3OH, $CHOH$, CO, as will be examined in depth in *section III* of this thesis.

$$2H_2O + 4h\nu \rightarrow 2H_2 + O_2 \tag{2}$$

It is worth noting, that the compounds mentioned above are already fully compatible with existing technologies for energy utilization and storage and can be used by the end user when and where they are required.[30,32,33]

1.1.4 Water Splitting in the Dye-Sensitised Photoelectrochemical Cell (DSPEC)

In the 1970s, Honda and Fujishima[34] first reported water splitting by ultraviolet bandgap excitation of anatase TiO_2 in a photoelectrochemical cell with a Pt cathode and a small pH gradient. The apparatus captured UV sunlight, and when this light interacted with the transparent semiconductor, the photogenerated electrons were directed into the conduction band of TiO_2. The migration of electrons to the counter electrode triggered the reduction of water to H_2, while the positive holes in the valence band oxidized water to O_2 (*figure 6*).
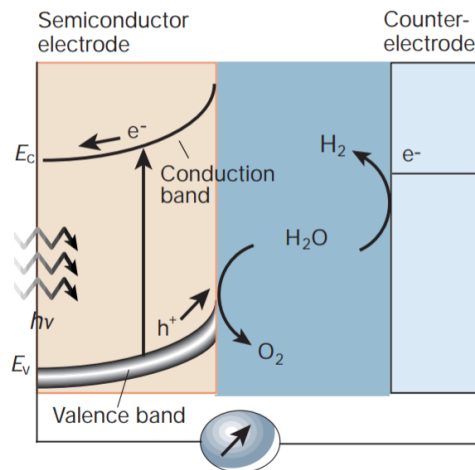
Figure 6: *scheme of an n-type anode like the one used by Fujishima and Honda*

Since the experiment of Fujishima and Honda, the scientific community has devoted a great effort to study water splitting and create always more efficient devices. Taking inspiration from the architectural concepts of the previously discussed Dye-Sensitized Solar Cells (*par. 1.1.2 of this section*), researchers developed Dye-Sensitized

Photoelectrochemical Cells (DSPECs). DSPECs rely on molecular sensitizers integrated with metal oxide semiconductors, in conjunction with water oxidation catalysts (WOCs) or hydrogen-evolving catalysts (HECs). These innovative designs hold great promise as methods for solar-driven water splitting (*figure 7*).[33]
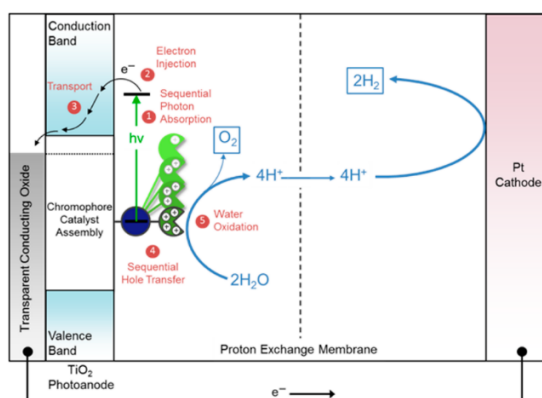
Figure 7: *schematic diagram for a DSPEC for water oxidation*[30]

As in the DSSC, the photogenerated electrons in the conduction band migrate through the bulk of the semiconductor and external circuit to the counter electrode, but in the DSPEC they are used to reduce water molecules to hydrogen. On the other hand, the positive holes in the valence band are used by the water oxidation catalysts (WOCs) to oxidize water molecules to oxygen, since the slow kinetics of the H_2O oxidation reaction calls for catalysis. Sunlight completes the overall water splitting process, which is remarkable. This is particularly impressive considering that, thermodynamically, the water decomposition reaction has a notable positive free energy change (ΔG) and a marginal positive entropy change (ΔS). As a result, hydrogen production is unfavourable at equilibrium, unless conducted at temperatures exceeding 4500 K. In DSPECs, H_2 and O_2 are generated at physically separated cathodic and anodic compartments, respectively, which allows an easy collection of H_2 gas. Since the seminal report of Fujishima and Honda, significant progress has been made on developing new semiconductors materials and improving the solar water splitting performances, but the choice of the semiconductor remains a crucial point. The semiconductor must exhibit an optimal band gap to ensure proper light absorption, current production, and maximum achievable voltages. Additionally, the position of the band gap is critical: the conduction

band should be more negative than the redox potential of the H$^+$/H$_2$ couple, while the valence band should have a higher energy level than O$_2$/H$_2$O redox potential (*figure 8*).
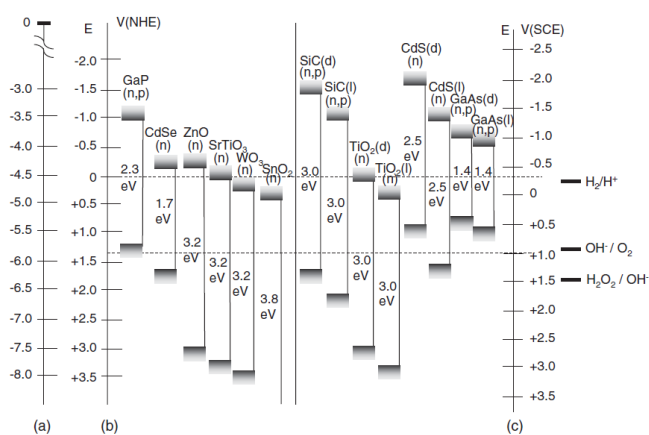
***Figure 8**: energy band gaps of various semiconductors with respect to a) vacuum b) NHE c) SCE*
©C. G. Zoski, Handbook of Electrochemistry. Amsterdam: Elsevier, 2007

A recurring challenge in the research of semiconductor photocatalysts or photoelectrodes is that it is intrinsically difficult to develop an oxide semiconductor that possesses both a suitably band gap and appropriate energy levels for catalytic reactions. Fine-tuning the band levels of these inorganic materials is inherently complex, thus the utilization of organic sensitizers attached to the metal-oxide semiconductor (MOS) surface arose as an ideal strategy to attain proper characteristics. By stark contrast to inorganic semiconductor, it is much easier to fine tune the HOMO and LUMO levels of organo-metal complexes and/or organic dyes through specific modifications of their molecular structures, thus readily adjusting their spectral response.[33] As essential parts in dye-sensitized photoanodes, the photosensitizer and WOC should fulfil some general requirements to make DSPEC devices functional: a) the photosensitizer should absorb sunlight as much as possible, even the near-infrared (NIR) part; b) the photosensitizer should possess anchoring groups for robust linkages to the semiconductor surface under aqueous condition; c) the LUMO level of the photosensitizer should be more negative than the conduction band edge of the n-type semiconductor to facilitate efficient electron injection after photoexcitation; the HOMO level of the photosensitizer, on the other hand, should be more positive than the catalytic onset potential of the WOC for oxygen evolution (see *figure 9*); d) the photosensitizer and WOC should be photo- and

electrochemically stable. The design principles of photosensitizers and various types of WOCs have been extensively overviewed in the past years.[25,35,36]
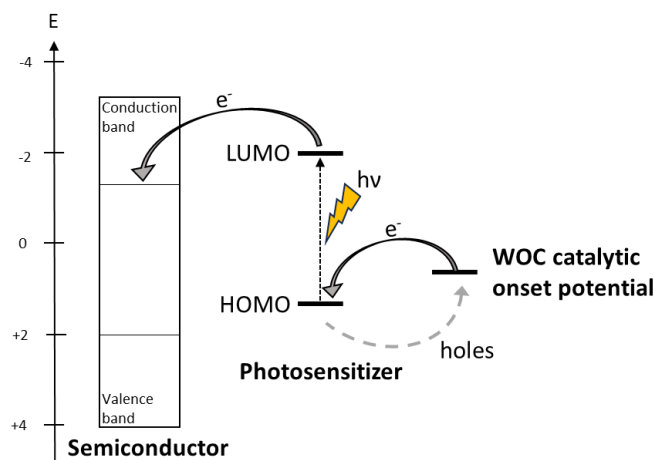
Figure 9: *schematic representation of light-driven excitation of photosensitizer's electrons. Electrons are then injected into the CB of the semiconductor, and holes are transferred to the WOC*

In 2009, Mallouk and co-workers[37] demonstrated the first example of a functional DSPEC for visible light-driven water splitting, in which the photoanode is a dye-sensitized nanocrystalline TiO_2 electrode. A ruthenium-tris(bipyridyl) complex serves as light absorber and as a stabilizer for the nanoparticulate hydrated iridium oxides ($IrO_2 \cdot nH_2O$) WOC. Upon irradiation with 450 *nm* light at an intensity of 7.8 *mW/cm²*, the cell produces a photocurrent density of 12.7 *µA/cm²*, corresponding to a quantum yield of ~0.9%. The low quantum yield is primarily ascribed to a significantly faster back electron transfer from the conduction band of TiO_2 to the oxidized dye molecules compared to the transfer from $IrO_2 \cdot nH_2O$ nanoparticles WOC to the oxidized dye. This limitation is commonly observed in DSPECs. However, in DSSC photovoltaic systems, oxidized sensitizers quickly undergo rejuvenation through electron donors in the electrolyte, typically within a microsecond, such as with a typical iodide electron donor. Conversely, the multi-electron processes essential in water splitting are energetically demanding and sluggish in terms of kinetics, particularly in the context of water oxidation reactions. In simpler terms, the rates of dye regeneration in DSPECs tend to be too slow to effectively counter the reverse electron transfers from the semiconductor oxides. Consequently, a profound molecular-level comprehension of the charge transfer dynamics at the semiconductor/dye/catalyst interface must be gained to enhance this approach further. A pivotal aspect for augmenting quantum efficiencies would involve the development of innovative sensitizer configurations that maintain long-lived charge-separated states.

1.2| DESIGN OF THE DYES

In the domain of DSPECs sensitizers, in particular in the dye-sensitized photoanode, porphyrins can play a crucial role, thanks to the possibility of precisely tuning their photophysical and electrochemical proprieties upon chemical functionalization.[38,39] In fact, a rational tailoring of the porphyrin core and judicious design of the substituents can improve the light harvesting ability of the dye and promote the charge injection process into the semiconductor. Further, by modulating HOMO and LUMO energy levels, the tailoring of the electronic characteristics and absorption spectrum of porphyrins becomes feasible. This enables the creation of porphyrin molecules with precisely matched HOMO-LUMO energy levels for effective integration with WOCs. The reduction in the HOMO-LUMO energy gap is associated with an enhanced *push-pull* character of the dye and with its light-harvesting abilities. In 2013 the SunLab research group reported[40] the advantages of using a 4D–π–1A structure (also referred to as "β-substituted") respect to the traditionally used *meso* substituted 1D–π–1A porphyrins. In fact, although the HOMO–LUMO energy gap of the *meso*-substituted *push–pull* dyes is lower, so that charge transfer along the *push–pull* system therein is easier, the β-mono- or disubstituted *push–pull* dyes show comparable or better efficiencies when acting as sensitizers in DSSCs, due to their broad and intense light absorption along the visible region. Moreover, for the 4D–π–1A structure, the group developed a straightforward and effective synthetic procedure that makes the described β-monosubstituted Zn[II] porphyrinates extremely promising sensitizers for use in DSSCs. They also demonstrated that employing a cyanoacrylic group to anchor the dye to the semiconductor, due to its electron-withdrawing properties, is advantageous as it leads to a substantial reduction in the LUMO energy, accompanied by a simultaneous decrease in the HOMO-LUMO energy gap. Another key point in designing sensitizers with enhanced light-harvesting is to utilize additional chromophores that can be directly linked to the porphyrin molecular structure. In fact, although porphyrins have a broad electronic absorption spectrum covering much of the solar spectrum, they suffer from weak absorptivity between the Soret and Q bands and in the NIR region. To address this, Lu et al.[41] found that benzothiadiazole (BTD) based acceptors have a beneficial effect, providing greater LUMO stabilization and longer-wavelength absorption. Consequently, many new-generation

porphyrin dyes now include this moiety as an ancillary acceptor between the porphyrin core and the anchoring group.[42–44] In the pursuit of water oxidation-focused chromophores, fluorinated porphyrins are well-suited due to their energy levels. The perfluorinated design, in fact, effectively generates an electron-poor porphyrin core, achieving a positive ground-state oxidation potential that enables access to energy-intensive redox reactions for solar energy conversion and storage, while also providing stability in oxidative and aqueous conditions through the presence of fluorine substituents.[45–47] However, the electron-poor core negatively affects the charge separation character of the dyes, as revealed by the study on the spatial distribution of the excited states, leading to a nonquantitative charge injection.[12] Taking into account this current state of knowledge, briefly summarized above, in 2019, SunLab investigated the two Zn[II] perfluorinated porphyrins reported in *figure 10*.[48]

A (β-TFP)   **B**
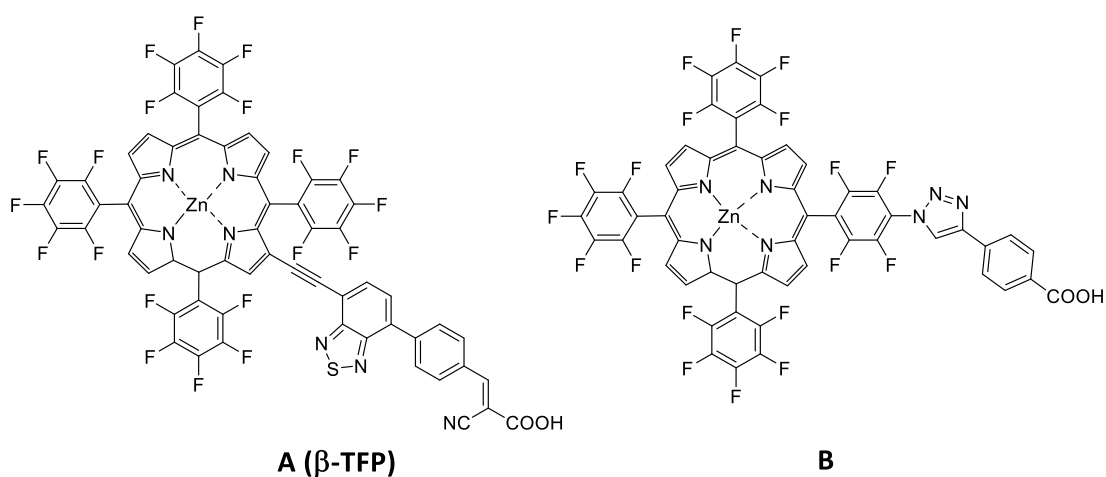
Figure 10: *Zn[II] porphyrins presented in Applied Sciences **2019**, 9 (13)*[48]

Both **A** (**β-TFP** from now on) and **B** are designed with structural features aimed at enhancing charge separation within the resulting dye-sensitized photoanode. They share a perfluorinated core conjugated with an electron-withdrawing linkers, and for **β-TFP**, a cyanoacrylic group for semiconductor surface anchoring. Functionalization occurs at either the β-*position* (**β-TFP**) or the *meso*-position (**B**), allowing for the assessment of their impact on sensitization efficiency and charge injection directionality from the excited state. Furthermore, porphyrin **β-TFP** incorporates a BTD moiety as an additional acceptor unit. Both dyes were successfully tested in HBr splitting.

HBr splitting stands out as a promising and cost-effective method for solar energy storage. In contrast to water splitting, which yields hydrogen and oxygen—where oxygen holds negligible economic value—HBr splitting yields Br_2. This bromine can serve various purposes, such as in chemical intermediate production or as fuel for fuel cells and redox flow batteries, effectively recuperating the stored energy within its bonds. [48–50] It is worth to consider, that traditional hydrogen-oxygen regenerative fuel cells necessitate heavy, high-pressure storage tanks for oxygen and are susceptible to membrane electrode assembly degradation due to the formation of peroxide radicals, spurred by high oxygen concentrations at the cathode. This challenge can be addressed by utilizing Br_2 as an oxidizing agent. Moreover, HBr splitting boasts the highest theoretical solar-to-hydrogen efficiency among available methods[48–51] Consequently, although both dyes effectively split HBr, enabling the conversion of red photons up to 700 *nm*, **β-TFP** outperformed **B** due to better injection efficiency and broader light absorption, aided by the presence of the BDT moiety.[48] Considering these results, we have conceived the three new perfluorinated Zn^{II} porphyrins presented in *figure 11*:

β-**F16**

meso-**F16**

meso-**F19**
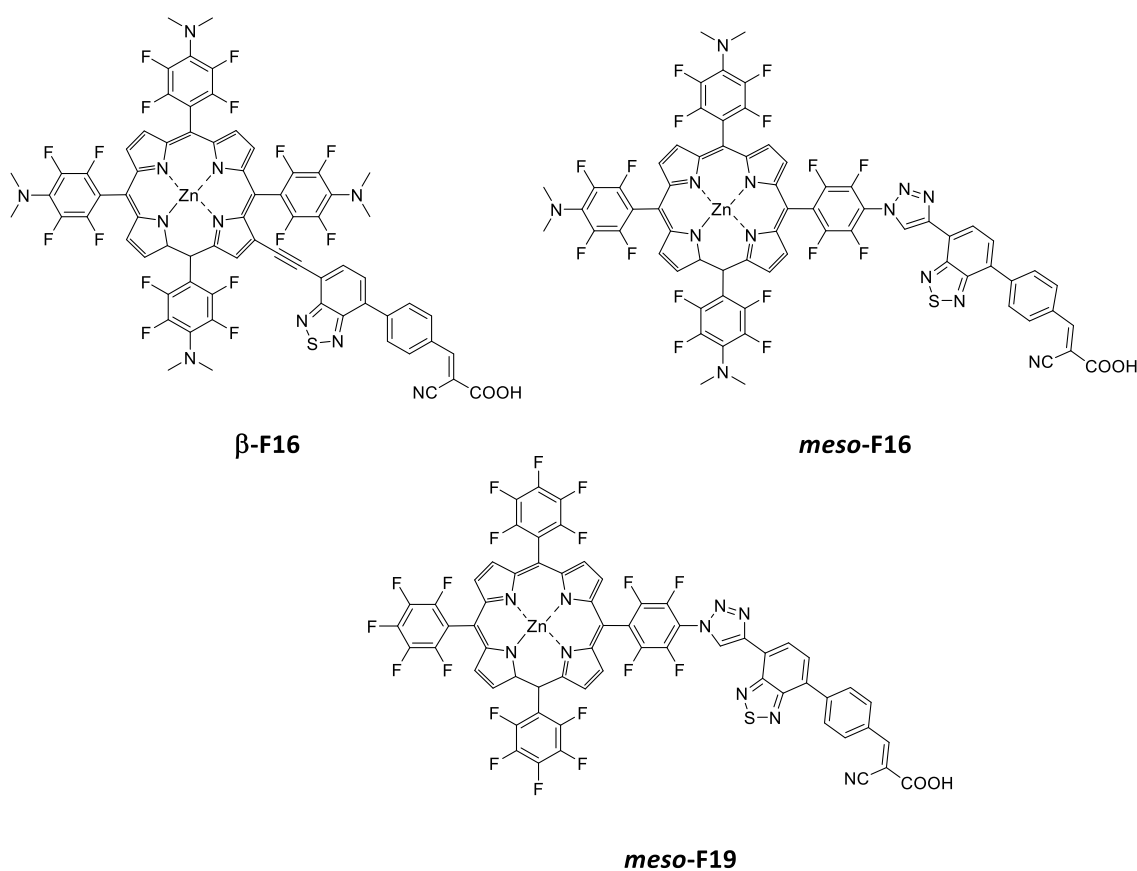
Figure 11: *Zn^{II} porphyrins studied in this section of the thesis*

The design approach which leads us to the three dyes involved enhancing charge transfer by adding donor groups to the porphyrin ring, trying to counteract the strong electron withdrawing effect of the fluorine atoms. This approach aims to improve the porphyrin's electron injection's ability, facilitating subsequent coupled oxidation reactions. These reactions can occur in the presence of an oxidation catalyst (e.g., water oxidation to O_2) or even independently, as seen in the production of Br_2 from HBr. It was then reported that the introduction of strong electro-donating substituents like diaryl-amine, in the push-pull framework affects positively not only the electron injection process but also the light harvesting ability of the sensitizer thanks to a more extend conjugation.[52,53] Considering this, the addition of donor groups such as dimethylamino groups (**β-F16** and **meso-F16**), is expected to lower the energy of the LUMO orbital of the molecule by narrowing the HOMO-LUMO gap, related to the charge separation, and producing a broadening of the absorption bands by extending the light-harvesting ability of the dye. The simultaneous presence of a strong electron-withdrawing moiety like the BTD and the cyanoacrylic anchoring pendant in all the compounds should further enhance the push-pull effect. Considering porphyrin **β-TFP** as a reference point, we could conduct a more thorough assessment of the impact of β-*functionalization* (**β-TFP** and **β-F19**) compared to *meso*-functionalization (**meso-F19** and **meso-F16**). Additionally, we could examine the influence of incorporating ancillary electro-donating dimethylamino groups into porphyrins with similar functionalization patterns (**β-TFP** vs. **β-F16**; **meso-F19** vs. **meso-F16**). Ultimately, we explored the use of the porphyrins depicted in *figure 11*, as photosensitizers in SnO_2-based photoanodes for the TEMPO-catalysed light-driven conversion of benzyl alcohol into aldehyde, in a collaborative effort with Professor Caramori from the University of Ferrara. TEMPO-catalysed light-driven oxidations could serve as an alternative oxidation reaction for the photoanode, replacing the oxygen evolving reaction which could compromise the long-term stability of the system. It is noteworthy that in natural systems, these reaction centres are periodically renewed by the living organisms, but in an artificial device this will be uneconomical. Furthermore, these types of reactions present a thermodynamically more efficient option compared to water oxidation, which necessitates the involvement of four electrons. These photo-driven reactions offer a sustainable approach to producing valuable carbonyl compounds, thanks to the environmentally friendly nature of DSPECs devices, which

enable oxidation without the need for toxic oxidants, making the entire process more economical, safer, and virtually limitless.

1.3| RESULTS AND DISCUSSION

1.3.1 Synthesis

The first two synthesis discussed in this thesis are the ones related to the porphyrin with 3D–π–1A architecture, **meso-F19** and his analogous **meso-F16**. As shown in *figure 11* they both consist of a tetra-pentafluorophenyl Zn^{II} porphyrin core with the BTD-acceptor unit bridged to one of the *meso* fluorophenyl ring by a triazole linker. Additionally, **meso-F16** is endowed with donor dimethylamino groups at para position of the three residual fluorophenyl rings. *scheme 1* summarizes the synthetic pathway of the two dyes:
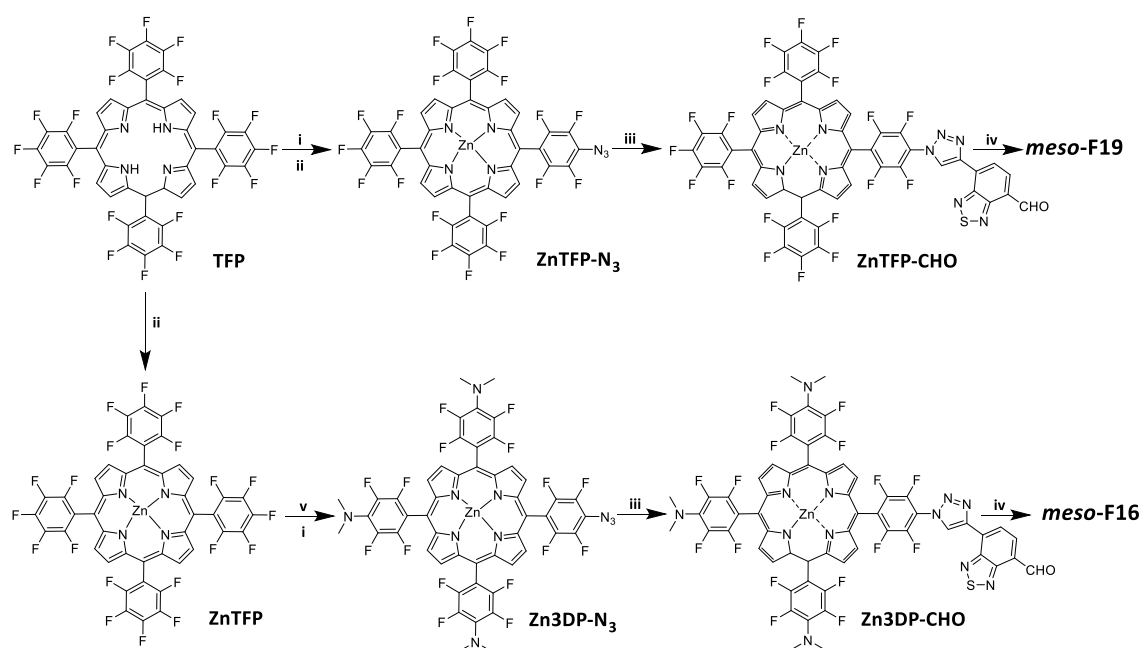
Scheme 1: synthesis of meso-F19 and meso F16
*i) NaN₃, DMF, 60°C, o.n.; ii) Zn(OAc)₂, CH₃OH, reflux, 3h; iii) BTD-3, Cuᴵᴵ/SAA, 50°C, 48h;
iv) CAA, toluene, TEA/piperidine, 90°C, o.n.; v) Me₂NH·HCl/KOH, DMF, 110°C, o.n.*

For both compounds, the starting reagent is the free base porphyrin TFP which is commercially available from Porphychem®. Alternatively, it can be synthetized in a simple and effective way by the one-pot condensation between pyrrole and pentafluorobenzaldehyde, catalyzed by the Lewis acid $BF_3(OEt_2)$, and followed by oxidation of the porphyrinogen upon addition of DDQ (2,3-Dichloro-5,6-dicyano-1,4-benzoquinone).[12] In the first part of *scheme 1*, in order to obtain **meso-F19,** TFP reacts with sodium azide in DMF, at mild temperature, overnight, to perform the selective nucleophilic substitution of one out of four of the *para* fluorine atoms of the

pentafluorophenyl rings. The free-base intermediate TFP-N_3 was collected in a 47% yield. The subsequent complexation of the core with zinc ions quantitatively provided ZnTFP-N_3 which was used as substrate for the following Cu(I)-catalysed azide-alkyne cycloaddition (CuAAC), also known as "click reaction",[54] with the acceptor unit BTD-3. The electron-withdrawing linker BTD-3 was previously synthetized following the procedure in *scheme 2*:
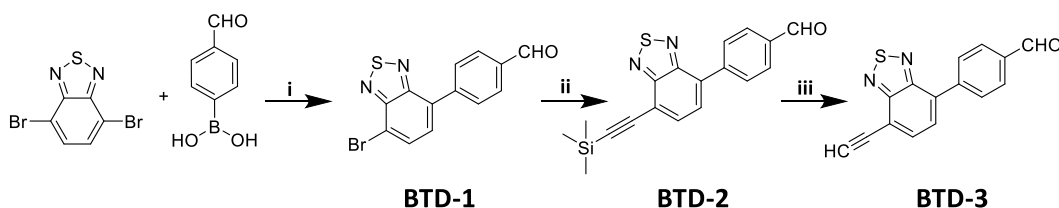
Scheme 2: *synthesis of BTD-3*

i) 1. Pd(PPh$_3$)$_4$, toluene, N$_2$, 30', 120°C; 2. Na$_2$CO$_3$ acq, EtOH, N$_2$, 3h, 116°C; ii) trimethylsilylacetilene, Pd(PPh$_3$)$_4$, CuI, THF, Et$_3$N, N$_2$, reflux overnight; iii) K$_2$CO$_3$, CH$_3$OH, CHCl$_3$, r.t. 2h

The first step involved a Pd-catalyzed Suzuki coupling between 4-(formylphenyl)boronic acid and 4,7-dibromobenzo[1,2,5]thiadiazole. Despite employing equimolar reagents (1:1), BTD-1 was produced with moderate yield (31%), because a comparable amount (25%) of the disubstituted side product was obtained. During the second step, a Sonogashira coupling between BTD-1 and trimethylsilylacetylene introduced a protected acetylene moiety, yielding BTD-2 with a 90% yield. Finally, deprotection of the acetylene group under mild conditions, using a saturated KOH aqueous solution, resulted in the formation of BTD-3, with 77% yield. The click reaction between BTD-3 and ZnTFP-N_3 to obtain the intermediate ZnTFP-*CHO*, was performed by using an in-situ Cu^I formation method, starting from Cu^{II} sulphate salt and sodium ascorbate (SAA) as reductant. CuAAC works generally with a broad range of reagents and can also be conducted in a large variety of solvents: non-coordinating solvents such as toluene and chlorinates, weakly coordinating solvents as THF and CH$_3$CN, polar solvents such as CH$_3$CN and DMSO, aqueous solvents including mixtures of water with organic solvents. The key role of the solvent or solvent-mixture is to solubilize both the substrate and copper catalyst to insure rapid reactions. In optimizing this reaction, we considered two different literature procedures. The first[55] involved CuI as catalyst and DIPEA as base at room temperature, in a mixture of THF and CH$_3$CN. This strategy didn't work at room temperature (*table 1*, entry 1) and gave unsatisfactory results at 50°C (entry 2). We also try to invert the order

of reactions in *scheme 1* trying to perform first the *click*-reaction iii) on the free base TFP-N_3 eventually followed by the metalation ii), but no product was collected both at room temperature and at 70°C (entries 3 and 4). We finally realized that the CuI in our lab was mostly oxidized to Cu[II], which posed potential issues because CuI is directly involved in the reaction mechanism, since it coordinates both the triple bond and the azide group, and it's crucial to maintain it in its reduced form. This supposition was confirmed when the addition of 2 equivalents of reduction agent ascorbic acid to the reaction almost doubled the yield (entry 5). This deduction leads us to a second protocol[56] that consists of using as pre-catalyst copper sulphate pentahydrate in combination with the reducing agent sodium ascorbate (SAA). $CuSO_4.5H_2O$ and SAA were separately dissolved in water, before mixing with ZnTFP-N_3 and BTD-3. We tried to let it react overnight at 50°C (entry 6) or at room temperature (entry 7) and found out that heating provides a slightly better yield (47% vs 35%). We hence decided to perform the reaction at 50°C, using copper-sulphate and SAA.

Table 1: *optimization of the CuAAC "click-reaction"*

Entry	Substrate	Pre-catalyst	Solvent	Temp. (°C)	Yield
1	ZnTFP-N_3	DIPEA/CuI (1eq/cat.)	THF/CH$_3$CN (1/1)	r.t.	-
2	ZnTFP-N_3	DIPEA/CuI (1eq/cat.)	THF/CH$_3$CN (1/1)	50	13%
3	TFP-N_3	DIPEA/CuI (1eq/cat.)	THF/CH$_3$CN (1/1)	r.t.	-
4	TFP-N_3	DIPEA/CuI (1eq/cat.)	THF/CH$_3$CN (1/1)	70	-
5	ZnTFP-N_3	DIPEA/CuI/ascorbic acid (1/1/2)	THF/CH$_3$CN (1/1)	r.t.	22%
6	ZnTFP-N_3	$CuSO_4 \cdot 5H_2O$/SAA (1.2/1.2)	H$_2$O/THF	50	47%
7	ZnTFP-N_3	$CuSO_4 \cdot 5H_2O$/SAA (1.2/1.2)	H$_2$O/THF	r.t.	35%

The final Knoevenagel condensation step between the aldehyde terminal group and cyanoacetic acid (CAA) provided the dye with the carboxylic functionality necessary to properly sensitize the metal oxide semiconductor. To maximize the conversion yield such a reaction was conducted in non-polar solvent (toluene) and in presence of triethylamine, as reported elsewhere[57,58], so the desired *meso*-**F19** was almost quantitatively obtained. In the second part of *scheme 1* the synthetic approach to obtain *meso*-**F16** is presented. After the metalation of the core, the creation of the 3D–π–1A architecture starts with the introduction of three dimethylamino groups at the periphery of the ZnTFP complex. The amination of the *para* positions of TFP was reported to efficiently occur by nucleophilic substitution mechanism at high temperature using DMF both as solvent and dimethylamine source.[59] Nucleophilic substitution usually does not occur for aromatic rings, with the exception of the case in which the core is strongly electron poor, like in the case of TFP. However, such hard conditions cannot be adopted to the asymmetrical functionalization of the porphyrin core, thus the method was modified to control the amination process by lowering the temperatures and using a quantifiable source of the nucleophile.[60,61] In particular, we tried using as nucleophile the ammonium salt $(CH_3)_2NH \times HCl$, both in presence or absence of KOH, at different temperature and in different solvents. Also, in this case we tried to perform the reaction both on the free base TFP and on the metalated ZnTFP. The attempts to find the best conditions for this reaction are summarized In *table 2*, considering that, as shown in *scheme 3* a mixture of different amination products is often collected. In *table* 2 the yields of tetra-substituted (4DP/Zn4DP) and tri-substituted (3DP/Zn3DP) products of interest are reported.

M = 2H (**TFP**)
M = Zn (**ZnTFP**)

M = 2H (**4DP**)
M = Zn (**Zn4DP**)

M = 2H (**3DP**)
M = Zn (**Zn3DP**)
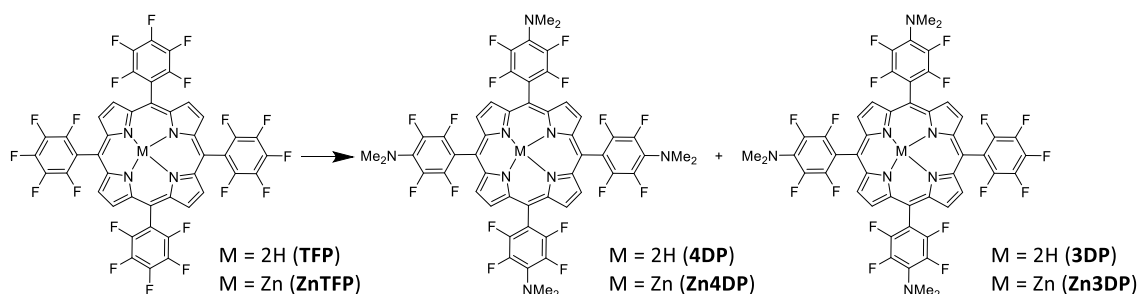
NB: also di- and mono- amination products are sometimes observed

Scheme 3: *products of amination*

Table 2: *optimization of the asymmetric amination*

Entry[a]	Substrate	(CH₃)₂NH·HCl (eq.)	KOH (eq.)	Solvent	Temp. (°C)	Yield of 4DP/Zn4DP	Yield of 3DP/Zn3DP
1	TFP	30	0	DMF	160	100%	-
2	TFP	30	0	DMF	70	-	7%
3	TFP	3	0	DMF	160	-	7%
4	TFP	4	8	DMF	110	75%	-
5	TFP	3	6	DMF	110	100%	-
6	TFP	4	8	THF	70	-	-
7	TFP	0	3	DMF	110	-	-
8	TFP	3	3	DMF	110	70%	27%
9	ZnTFP	0	3	DMF	110	-	-
10	ZnTFP	3	3	DMF	110	-	25%
11	ZnTFP	4	4	DMF	110	51%	15%
12	ZnTFP	3.3	3.3	DMF	110	23%	40%

[a]*All reactions are performed overnight.*

In the initial attempt (entry 1), we used a large excess of ammonium salt in DMF at reflux temperature, resulting in the formation of only the tetra-substituted porphyrin 4DP, as reported in literature.[56] Lowering the reaction temperature to 70 °C (entry 2) led to the production of some tri-substituted molecule (3DP) in 7% yield, along with small amounts of mono and di-substituted porphyrins. This indicated that both an excess of amine and higher temperature are crucial for completing the reaction. Using stoichiometric amounts of ammonium salt in DMF at reflux temperature (entry 3) resulted in a low yield of tri-substituted molecule 3DP. To improve control over the reaction, we introduced a base (KOH) in entry 4 to free the chlorohydrate (CH₃)₂NH×HCl and make it more reactive. In this case, using DMF at 110 °C, 4 *equivalents* of ammonium salt, and 8 *equivalents* of KOH, we obtained a good yield (75%) of the tetra-substituted 4DP, along with some side products. Surprisingly, in entry 5 using the same temperature and solvent conditions, but with 6 *equivalents* of KOH and substoichiometric (CH₃)₂NH×HCl (3 *eq.*), we again

obtained the intermediate 4DP quantitatively. This suggested that an excess of KOH could somehow promote a nucleophilic attack of DMF on the porphyrin. Changing the solvent (entry 6), lowering the temperature, or omitting the amine chlorohydrate (entry 7) resulted only in degradation by-products and traces of mono and di-substituted porphyrin. This highlighted the necessity of ammonium salt and base along with DMF solvent and high temperature (110°C), for the successful amination of the *para* positions in pentafluorophenyl porphyrins. The best conditions we found, starting with the free base TFP, (entry 8) involved 3 *equivalents* of both $(CH_3)_2NH\times HCl$ and of KOH in DMF at 110°C yielding 27% of the desired trisubstituted 3DP and 70% of tetrasubstituted 4DP. Under this alkaline condition, the free-base porphyrin seems to be very reactive and mostly underwent to complete amination of all *para* positions leading to formation of 4DP. Thus, we decided to explore the reactivity of the Zn^{II}-analogous ZnTFP under the same condition (entry 9). Conversely to what happened with the free-base porphyrin (entry 7), none of substituted porphyrins were isolated and no side products were formed with zinc-porphyrin in agreement with a lower reactivity. Due to the evident lower reactivity of the Zn^{II}-porphyrin ZnTFP, compared to the free-base TFP, the reaction was performed with larger amount of reactants to maximize the formation of tri-substituted zinc-porphyrin Zn3DP. 4 *equivalents* of ammonium salt and KOH (entry 11) produced a lowering of the desired product Zn3DP (15%) and a simultaneous and significant increase of tetra-substituted porphyrin Zn4DP (51%). Best results were obtained with 3.3 *equivalents* of both $(CH_3)_2NH\times HCl$ and KOH (entry 12) providing the intermediate Zn3DP with 40% of yield as favourite product. This investigation revealed that the metalled porphyrin is ideal as substrate for the nucleophilic attack in alkaline condition allowing better control over asymmetric amination on three positions and mostly preventing the tetra-substituted molecule and side products formation. The subsequent azido derivative Zn3DP-*N₃* was easily obtained, in almost quantitative yield, by nucleophilic substitution of the residual *para* fluorine of the unsubstituted *meso* aryl group with an excess of sodium azide. Such modification didn't affect the polarity of the porphyrin core; thus, we weren't able to isolate the product Zn3DP-*N₃* by chromatographic separation and the progress of the reaction was checked by ^{19}F-NMR looking at the disappearance of the peak related to the residual *para* fluorine. As for **meso-F19** the BTD-acceptor substituent BTD-3 was inserted by CuAAC reaction, using

optimized reaction conditions discussed before, and the terminal anchoring group by a Knoevenagel condensation to give the desired dye *meso*-**F16**. *Scheme* 4 illustrate the synthetic multistep pathway to obtain the 4D–π–1A type dye **β-F16** and the reference dye **β-TFP**.
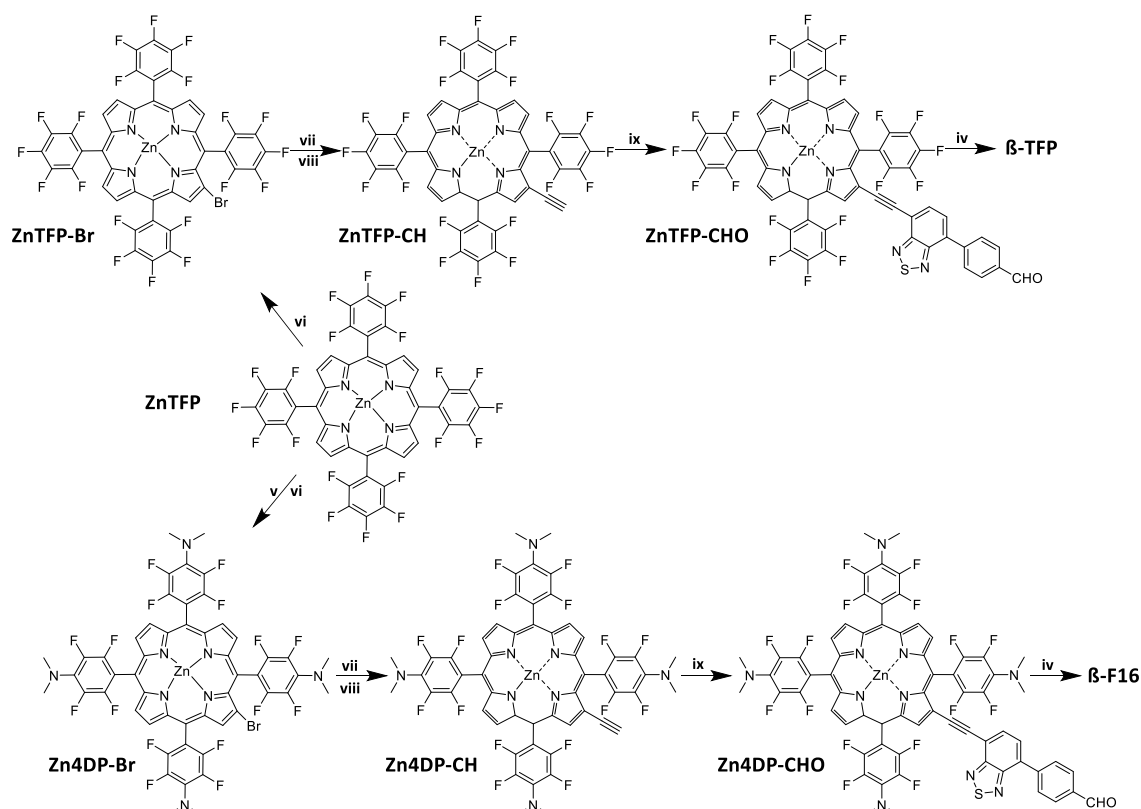
Scheme 4: synthesis of reference compound β-TFP and β-F16

v) Me₂NH·HCl/KOH, DMF, 110°C, o.n.; vi) NBS, CH₃OH, r.t., o.n.; vii) THS-CH, Pd(PPh₃)₄, TEA/DMF 60°C, MW; viii) TBAF/THF, r.t. 1h; ix) BTD-1; Pd(PPh₃)₄, TEA/THF; 70°C, o.n.; iv) CAA, toluene, TEA/piperidine, 90°C, o.n.;

In this case, the common starting point of the two pathways is ZnTFP, which can be obtained by metalation of the commercially available TFP as described above. The synthesis of **β-F16** involves an additional amination step by multiple nucleophilic substitution that successfully occurred in DMF at 110°C with an excess of amine source. From this point the two synthetic routes proceed in parallel and retrace the procedure previously reported,[48] although some steps required additional refinement. Both ZnTFP and Zn4DP were functionalized at the β-*pyrrolic* position with a bromine atom with NBS in methanol at room temperature affording respectively the intermediate ZnTFP-*Br* (yield: 75%) and Zn4DP-*Br* (70%). This step was optimized on ZnTFP as shown in *table 3* and the same protocol was subsequently applied to Zn4DP.

Table 3: *optimization of bromination step*

Entry	NBS (eq)	Solvent	Temperature (°C)	Time (h)	Yield (calc. From ^{1}H-NMR)
1	1.7	CHCl$_3$	70	16	?
2	1.7	CCl$_4$	76	16	?
3	1.7 (+ 2.7 Py)	CH$_2$Cl$_2$	50	16	?
4	1.5	MeOH	80	3	30%
5	1	MeOH	25	16	75%
6	1	MeOH	0 à 25	16	63%
7	0.8	MeOH	25	16	56%

The primary challenge with this reaction is the limited control on achieving only the mono-brominated product. Indeed, after the first bromide insertion, further additions are favored, resulting in a mixture of mono- and dibrominated products, along with unreacted starting material, even with just an equivalent of NBS.[62] Entry 1 of *table 3* was based on a literature procedure already known in the laboratory,[62] but it led just to a mixture of unreacted porphyrin and polyfunctionalized porphyrins. Trying different halogenated solvents (entry 2 and 3) again gave us just polybrominated products, from which the isolation of the mono-bromo porphyrin through gravimetric chromatography was unattainable, due to the comparable polarity of the various brominated compounds. Given the failures, we tried to change the nature of the solvent and to conduct the reaction in MeOH. We started refluxing a solution of ZnTFP in MeOH with 1.5 *equivalents* of NBS for 3 *hours* (entry 4). In this case, we obtained a mixture of monobromo-porphyrin and dibromo-porphyrin. Even in this case, it was impossible to isolate the mono-bromo porphyrin by gravimetric chromatography, but having just two brominated derivatives, we were able to estimate a reaction yield by ^{1}H NMR, evaluating the ratio of the intensity of the peaks ascribed to the monobromo-porphyrin and dibromo-porphyrin. In these conditions we obtained 30% of yield (*Figure 12a*).
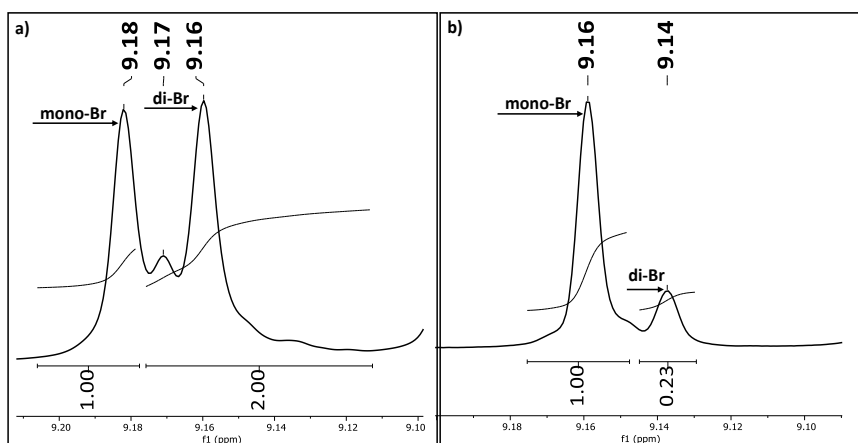
Figure 12: a) ^{1}H-NMR of entry 4; b) ^{1}H-NMR of entry 5

In order to reduce the reactivity and minimize the formation of di-bromo porphyrin, we carried out the reaction at room temperature with 1 equivalent of NBS, overnight (entry 5); at 0°C always with 1 equivalent of NBS, overnight (entry 6) and with sub-stochiometric quantity of NBS (entry 7). We found that best conditions are the ones indicated in entry 5, where we obtained 75% of the desire product (percentage calculated from NMR estimate, *Figure 12b*). Since the target molecule was hard to isolate by chromatography techniques, it was collected as a mixture with the unreacted substrate and polybrominated side products and used for the next step. In order to maximize the electronic delocalization, which plays a key role in improving the charge separation character of the donor-acceptor system, the BTD acceptor unit was bridged to the porphyrin core by a π-conjugated ethynyl linker. The ethynyl terminal moiety was then inserted at 80°C in 5 *minutes* by a microwave-assisted Sonogashira coupling reaction with trihexylsilyl acetylene (THS-*CH*). Thanks to the long alkyl chains, the silane protecting group endowed the molecule with the proper features to guarantee an easier purification by column chromatography from poly-functionalized and non-functionalized products. The Sonogashira's reaction conditions are again the result of an optimization process since this is a very sensitive step in the synthetic process. Indeed, prior research showed that achieving significant conversion at the pyrrolic position requires high temperatures, while in this case the initial perfluorinated porphyrin core is more susceptible to these conditions compared to non-fluorinated porphyrinic substrates previously studied.[40] High temperatures can lead to unwanted byproducts, reducing reaction yields and complicating purification. Previous optimized reaction were

conducted at 55°C using a mixture of TEA and THF as solvent, $Pd(PPh_3)_4$ as catalyst, $HC{\equiv}C\text{-}Si(Hex)_3$ as coupling agent in presence of CuI (*table 4*, entry 1), resulting in moderate yields at the cost of long reaction times (7 *days*). In order to shorten reaction times and increase yields, we carried out a systematic study of microwave-assisted coupling conditions. A summary of the optimization attempts is provided in *table 4.*

Table 4: *optimization of Sonogashira's coupling*

Entry	T (°C)	Heating	Time	Catalyst	Yield
1	55	Thermal	7 *days*	$Pd(PPh_3)_4$	36%
2	120	MW	15 min	$Pd(PPh_3)_2Cl_2$	<5%
3	120	MW	5 min	$Pd(PPh_3)_2Cl_2$	37%
4	120	MW	1 min	$Pd(PPh_3)_2Cl_2$	40%
5	80	MW	15 min	$Pd(PPh_3)_2Cl_2$	17%
6	80	MW	5 min	$Pd(PPh_3)_2Cl_2$	53%
7	80	MW	1 min	$Pd(PPh_3)_2Cl_2$	22%
8	80	MW	5 min	$Pd(PPh_3)_2Cl_2$	62%

Entry 2-8 were prepared by adding the following to a proper microwave vial: 1 *eq*. of ZnTFP-*Br*, 2 *eq*. of THS-C≡CH, 0.2 *eq*. of the proper palladium catalyst, freshly distilled TEA and anhydrous DMF (*ratio* 1.5/1). The mixture was then purged with a stream of nitrogen for 15 *minutes* to ensure the removal of oxygen. After adding a small amount of CuI (0.1 *eq*.), the vial was sealed and placed in a monomodal MW reactor (Biotage®). Initially, the temperature remained constant (entries 2-4), resulting in increasing yields along with reduced reaction times. Entry 2 is particularly noteworthy as it shows a low yield (<5%) after just a 15-minute reaction, despite the complete consumption of all starting reagents. This suggests a predominant role of side reactions. To mitigate these latter, the reaction was carried out at lower temperatures (entries 5-7). The best results were achieved in 5 minutes (entry 6), while a 1-minute reaction (entry 7) led to some unreacted starting material. Consequently, the optimal balance between temperature and reaction time was found to be 5 minutes at 80 degrees (entry 6). Even better yields were obtained by using Palladium Tetrakis instead of Bis(triphenylphosphine)palladium(II) dichloride (entry 8) which gave the desired product

with 62% yield in the case of ZnTFP-*Si*, while a similar protocol gave Zn4DP-Si with 50% yield. The isolated intermediates were then deprotected by the cleavage of silane protecting group with TBAF (tetrabutylammonium fluoride) and the resulting ZnTFP-*CH* and Zn4DP-*CH* were allowed to react with the brominated acceptor derivative (BTD-3) under thermal Sonogashira coupling to successfully give the aldehyde intermediate ZnTFP-*CHO* and Zn4DP-*CHO*. This second Sonogashira's coupling was performed under thermal condition at 70 °C by using a mixture of equal volumes of TEA and THF as solvent. It is worth mentioning that during our investigation we noticed that the performance of both MW-assisted and thermal Sonogashira coupling procedures are not affected by the presence or the absence of CuI in the reaction mixtures. The subsequent Knoevenagel condensation was performed as previously described in toluene providing the desired dye **β-TFP** and **β-F16** efficiently (80-90% yield).

1.3.2 UV-Vis Spectroscopic Properties in Solution

The effect of the substituents on the photophysical properties of **meso-F19**, **meso-F16** and **β-F16** in comparison with the ones of the reference **β-TFP** was evaluated by UV−Vis spectroscopy in diluted THF solution. The ε-normalized absorption spectra of the dyes are shown in *figure 13* and the corresponding data are summarized in *table 5.*
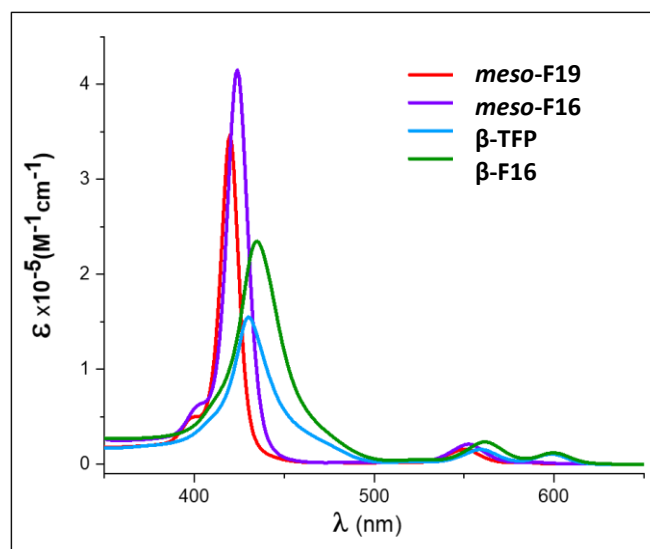
***Figure 13**: absorption spectra recorded in THF solution*

Entry	λ_b/nm (*logε*)	λ_q/nm (*logε*)	E^{0-0}/ev
meso-F19	420 (*5.54*)	550 (*4.22*) 585	2.11
meso-F16	424 (*5.62*)	552 (*4.34*) 590	2.08
β-F16	435 (*5.37*)	563 (*4.37*) 600 (*4.09*)	2.05
β-TFP	432 (5.27)	560 (4.27) 600 (4.12)	2.07

The presence of perfluorinated withdrawing rings produces a blueshift of the typical absorption bands of porphyrin-based dyes, however, the insertion of amine donor groups and the BTD-acceptor unit can strongly influence the electronic properties and thus the spectroscopic features of the final dyes. A proper arrangement of donor and acceptor groups in the molecular structure can affect the overall *push-pull* character of the dye, which is reflected in both absorption and emission properties. At a first look, we can notice that the absorption spectra of **meso-F19** and **meso-F16** and the ones of **β-TFP** and **β-F16** are almost superimposable as expected from their similar molecular architecture. The absorption spectra of the two *meso*-substituted compounds are featured by an intense and narrow Soret band (B band) around 420 *nm* with a less intense shoulder at higher energy and one weak Q absorption band at lower energy. A closer look reveals a further Q band with a very low intensity at about 590 *nm*. A broadening of the Soret band along with a slight redshift (2-8 nm) of all absorption and emission bands are perceivable in **meso-F16**, due to the presence of the dimethylamino moieties (*table 3*). Their electron-donating ability in the 3D–π–1A pattern likely improves the donor-acceptor system, thus favouring the electronic transitions at lower energies, as highlighted by the reduced optical *band-gap* obtained for **meso-F16** (2.08 *eV*) compared to **meso-F19** (2.11 *eV*). The presence of a BTD-acceptor unit, instead, doesn't significantly affect the absorption pattern of these *meso*-substituted dyes contrary to what happens when such a unit is inserted at the β-position, where is possible to observe a broadening of the B bands as for **β-TFP** and **β-F16**. The lack of this latter thus suggests an interruption of the electronic communication between the porphyrin core and the

BTD unit *via* the triazole *meso*-linker as evidenced by DFT analysis and the electronic distribution of molecular orbitals (MOs) (*see paragraph 1.3.4*). The presence of both the amino groups and the BTD-unit arranged in a 4D–⬚–1A architecture produce appreciable effects on the spectroscopic properties of **β-F16**. In fact, it is possible to notice in *figure 13* a red-shift and a broadening of both B and Q bands in **β-F16** compared with the reference compound **β-TFP**. This is in accordance with a more effective *push-pull* character between the donating porphyrin core and the accepting anchoring linker in the β-substituted architecture as confirmed by the narrower optical *band-gap* (2.05 *eV* and 2.07 *eV*) measured in the series. As said before, the theoretical calculations corroborate a more efficient charge-transfer character in **β-F16** as already observed in **β-TFP** [48] by showing the distribution of Mos electron density moving from the HOMO levels, localized on the amine donors, to the LUMO on BTD acceptor. The red-shifted and broadened B band (435 *nm*), together with the two Q bands up to 600 *nm*, endow such a dye with improved light harvesting ability in the visible absorption range compared with the *meso* series.

1.3.3 DFT Calculations

DFT calculations, performed by professor Caramori's group, at the university of Ferrara, revealed how the BTD group forms a dihedral angle of ≈55° in the case of the 3D–π–1A-based systems suggesting partial interruption of π conjugation, potentially leading to reduced CT character of the *meso*-substituted dyes. Conversely, for the β analogue, the ethynyl linker was found, as expected, more effective in promoting the electronic delocalization exhibiting a dihedral angle of 7° with respect to the porphyrin core and of 26° with respect to the BTD moiety. The computed HOMO energy aligns with the experimental ones, with ***meso*-F19** and **β-F16** showing respectively the deepest and shallowest HOMO levels among the series (*table 6*). This agrees with the presence of electron withdrawing groups in ***meso*-F19**, which deplete by inductive effects the electron density of the porphyrin core, whereas in **β-F16** the presence of amino donor groups in the 4 positions of the perfluoro phenyl rings partly mitigates the depletion of the porphyrin core. Indeed, a substantial orbital contribution of the amino groups can be observed in the isodensity surfaces of the HOMO (-1) and (HOMO-2) of **β-F16** in *figure 14*:
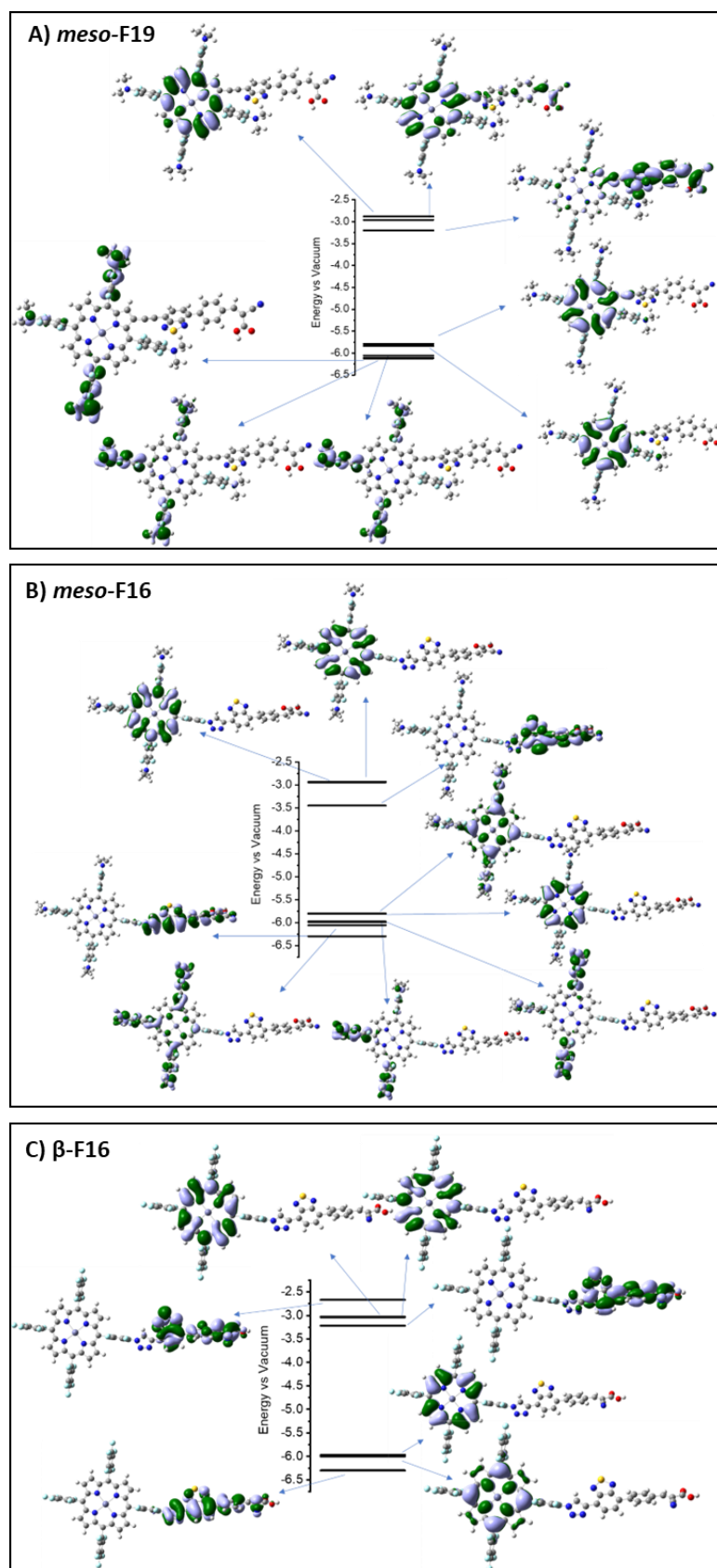
Figure 14 A-C: *energy levels of the KS orbitals for the three new-synthetized dyes, along with their corresponding isodensity surfaces*

Based on EDDMs at this theoretical level and assuming injection from the lowest thermalized singlet state, we predict the 4D–π–1A architecture to excel, followed by *meso*-**F16** and then *meso*-**F19**.

1.3.4 Electrochemical Investigation in Solution

The electronic properties of *meso*-**F19**, *meso*-**F16** and **β-F16** were first examined by cyclic voltammetry (CV) in DMF solution with TBAPF$_6$ 0.1 M, as supporting electrode, providing complete CV patterns (*figure 15a*) recorded at 0.2 *V/s* on a glassy carbon (GC) electrode and referred to ferrocenium/ferrocene redox couple for intersolvental comparison of electrode potentials. In order to provide a better determination of the peak potentials, the DPV analysis (*figure 15b*) was also performed under the same condition of the CVs; the key features are summarized and then compared in *table 6* with the ones obtained for **β-TFP** in the previous work.[48] Additionally, to gain insights about the effectiveness of the molecular design, we also performed a comparison with the unsubstituted zinc porphyrin ZnTFP.
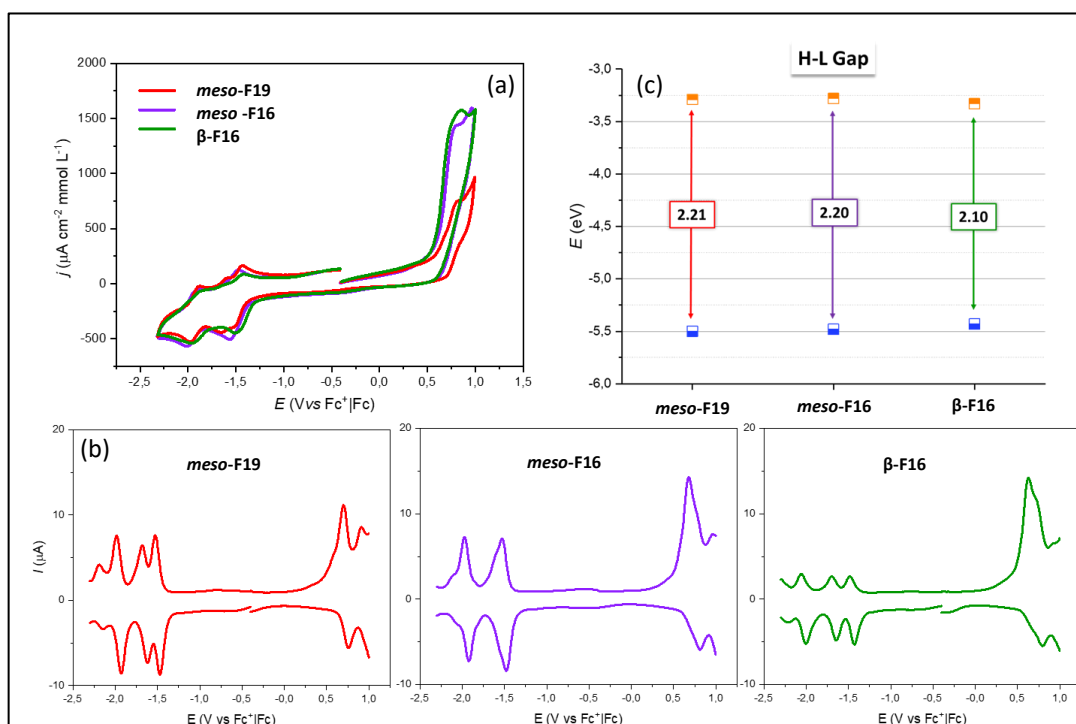
Figure 15: CVs, DPVs and electrochemical HOMO-LUMO gaps of the three new-synthetized dyes

Table 6: synopsis of electrochemical properties

Entry	$E_{P,IA}/V$ (Fc$^+$|Fc)	$E^{0'}_{IA}/V$ (Fc$^+$|Fc)	$E_{P,IC}/V$ (Fc$^+$|Fc)	$E^{0'}_{IC}/V$ (Fc$^+$|Fc)	E_{HOMO} (Ev)	E_{LUMO} (Ev)	H-L GAP (Ev)
ZnTFP	0.66	0.68	-1.52	-1.54	-5.48	-3.26	2.22
meso-F19	0.68	0.70	-1.49	-1.51	-5.50	-3.29	2.21
meso-F16	0.66	0.68	-1.50	-1.52	-5.48	-3.28	2.20
β-F16	0.61	0.63	-1.45	-1.47	-5.43	-3.33	2.10
β-TFP	0.80	0.86	-1.43	-1.46	-5.63	-3.48	2.15

In the investigated potential window, all dyes show two or more reversible reduction and one poorly resolved and quasi-reversible oxidation peaks. The broad anodic waves at around 0.80V increase in intensity when the dyes are decorated with amino donor-groups, however in all cases a multielectron process seems to be involved during the oxidation of the porphyrins. The DPV patterns, in accordance with those obtained with CV, show multiple reversible cathodic peaks and one intense anodic wave for all dyes. Further, the better resolution of the peaks allowed us to measure the electrochemical HOMO and LUMO energy levels, derived from $E^{0'}_{Ia}$ and $E^{0'}_{Ic}$ respectively, and the relative HOMO-LUMO gaps. By comparing the first cathodic waves ($E_{p,Ic}$) more negative potentials can be observed for the *meso*-series **meso-F19** (-1.49 *V*) and **meso-F16** (-1.50 *V*) than for **β-F16** (-1.45 *V*) and **β-TFP** (-1.43 *V*) in agreement with an easier reduction of the porphyrin with 4D–π–1A architecture. The anodic waves are in the range 0.61-0.68 *V* moving from **β-F16** to **meso-F16** and **meso-F19** and much bigger is the anodic wave of **β-TFP** (0.80 *V*). **meso-F19** and even more **β-TFP** result as the hardest dye to oxidize in accordance with the electron-poorest porphyrin core. As expected, the presence of amino donor groups makes easier the oxidation of **β-F16** and **meso-F16** producing, the destabilization of the corresponding HOMO levels. The H-L energy gaps (*figure 15c)*, derived from DPV measurements, nicely reproduce the trend obtained by spectroscopic analysis with the narrowest gaps observed for the β-substituted porphyrin **β-F16** (2.10 *eV*) and **β-TFP** (2.15 *eV*). The comparison with ZnTFP allowed to confirm that the introduction of the BTD acceptor unit on the *meso* position of ZnTFP, as for **meso-F19**, affects largely the cathodic potentials of the dye by facilitating its reduction and thus lowering the LUMO energy level. However, a slight anodic shift can be also observed for

the first oxidation wave, as expected from the electron-poorer porphyrin core. The combination of the mentioned effects results in a very small reduction of the H-L gap (2.21 *eV*) compared to that of ZnTFP (2.22 *eV*). Focusing on the 3D–π–1A type dye **meso-F16**, the further insertion of amino donor groups produces a slightly narrower H-L gap (2.20 *eV*) mostly originated by the destabilization of the HOMO as a consequence of the cathodic shift in the first oxidation potential. It is worth noting that when both the amino groups and the BTD unit are arranged in a 4D–π–1A donor-acceptor system through the π-conjugated linker at the pyrrolic position, as for **β-F16**, the H-L gap significantly lowers to 2.10 *eV*. The simultaneous destabilization of the HOMO level and the stabilization of the LUMO, derived from easier oxidation and reduction processes, endow the dye with the narrowest electrochemical bandgap in accordance with a more efficient *push-pull* system and an improved charge-separation character.

1.3.5 Injection Efficiency and Devices Test with TEMPO

To assess injection quantum yield, our chromophores were evaluated on sensitized TiO_2 or SnO_2/TiO_2 with 0.1 *M* sodium ascorbate at pH 5. Photocurrent onset occurred at -0.6 *V vs SCE*, plateauing to 0.2 *V*. Net photocurrent varied in the order: **meso-F19** < **meso-F16** < **β-F16**, ranging from 960 $\mu A/cm^2$ to 1.7 mA/cm^2. IPCE (Incident Photon to Current Conversion Efficiency) under 0.1 *V* reverse polarization confirmed that the excited state of the dye is indeed responsible for the photocurrent generation. Quantum yields were comparable, among the different dyes with maxima of 14-18% in the Soret region and 12-14% in Q bands portion. A similar trend was found when the same chromophores were loaded onto SnO_2/TiO_2. However, the photocurrent response was now generally higher owing to the lower conduction band position of SnO_2, resulting in 1.5, 1.7 and 2.1 mA/cm^2 for **meso-F19, meso-F16**, and **β-F16** respectively. IPCE mirrored TiO_2, with increased yields (17-20% in Soret, 15% in Q bands). The higher photocurrent for 4D–p–1A system is attributed to a bathochromic shift from the lower H-L gap. Lithium iodide on SnO_2/TiO_2, the sole electrode used, yields higher conversions than pure TiO_2. In the upper part of *figure 16,* photocurrent density-voltage curves show **meso-F19**, **meso-F16**, and **β-F16** at 0.5 mA/cm^2, 1.2 mA/cm^2, and 2.5 mA/cm^2, respectively.
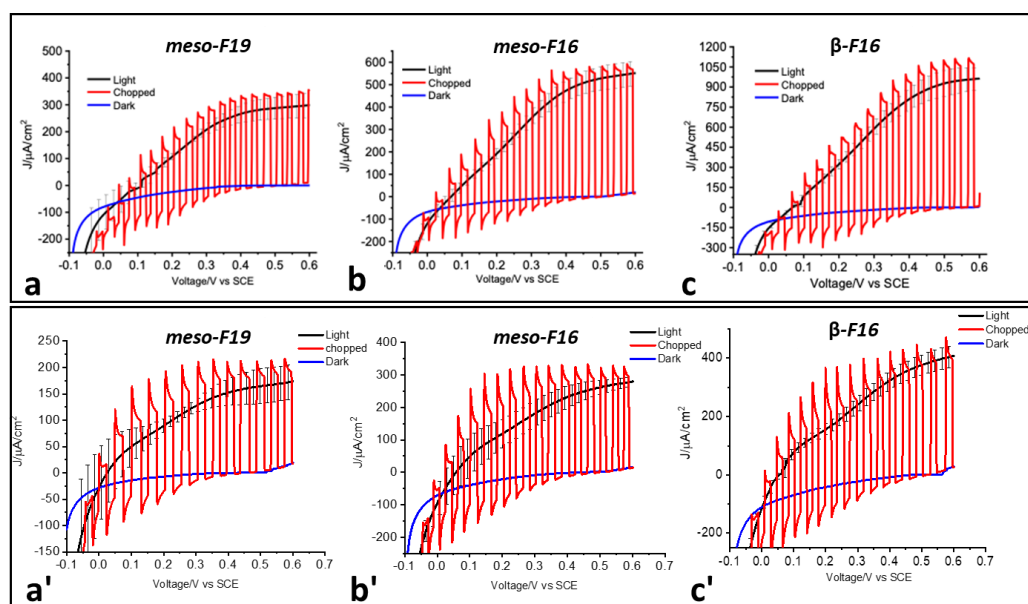
Figure 16: *Photocurrent density – voltage (JV) curves for the three porphyrins absorbed onto SnO₂/TiO₂ in contact with 10 mM TEMPO/0.1 M LiClO₄/ACN. The electrodes were illuminated from the back side (a, b, c) and from the front side (a', b',c'). All the JVs were recorded in the presence of a 400 nm cut-off.*

The experimental evidence aligns Electron Density Difference Maps (EDDMs), where **β-F16** demonstrates superior excited state directionality and higher injection quantum yield. In the presence of a 10 *mM* TEMPO/ACN electrolyte, the photocurrent of porphyrins on SnO₂/TiO₂ doubled when illuminated from the FTO side compared to front irradiation (lower part of *figure 16*), highlighting the significant impact of TEMPO on competing for photon absorption. The onset of the photocurrent is around 0.1 *V*, reaching a plateau up to 0.6 *V*. The current order is again ***meso*-F19** < ***meso*-F16** < **β-F16** (300 $\mu A/cm^2$ to 1000 $\mu A/cm^2$). Increasing TEMPO concentration to 50 *mM* and 100 *mM* significantly decreased the current (150 $\mu A/cm^2$ to 450 $\mu A/cm^2$), attributed to high light losses through the electrolyte. For benzyl alcohol (BzOH) oxidation, a 10 *mM* TEMPO concentration was chosen for optimal electrolyte transparency, illuminated from the FTO side. In acetonitrile, BzOH oxidation requires a base for proton extraction. We selected TBPy due to its relatively low basicity. Electrochemical studies showed reversible TEMPO oxidation, and increasing base concentration led to an s-shaped voltammogram. **β-F16** based electrode optimization involved analysing photocurrent response as a function of BzOH concentration. The photocurrent increased linearly with BzOH concentration (100 $\mu A/cm^2$ without BzOH), suggesting faster TEMPO regeneration. For exhaustive photoelectrolysis with **β-F16**, the optimal electrolyte was 10 *mM* TEMPO/70 *mM*

BzOH/0.1 *M* TBPy/0.1 *M* LiClO4/ACN, striking a balance between solution transparency, SnO2 Fermi level positioning, and scavenger concentration. *Figure 16a* displays the JV curves for **β-F16** with the optimized electrolyte in a standard three-electrode/one-compartment cell.
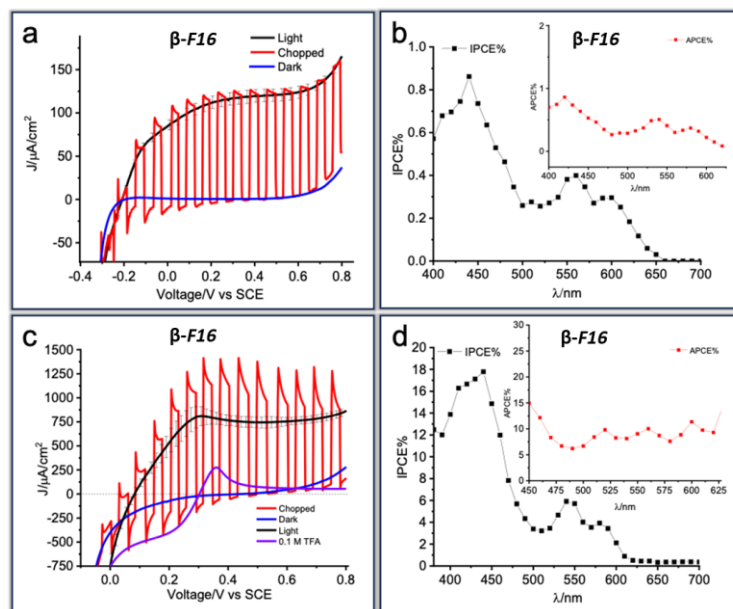
Figure 17: *(a) Photocurrent density – voltage (JV) curves and (b) IPCE% (APCE% as insert) for β-F16 in contact with 10 mM TEMPO/70 mM BzOH/0.1 M LiClO$_4$/0.1 M TBPy/ACN onto SnO$_2$/TiO$_2$. (c) JV curves and (b) IPCE% (APCE% as inset) for the same electrode in contact with 10 mM TEMPO/70 mM BzOH/0.5 M LiTFSI/ACN. The JV curves reported in (a) and in (c) were recorded in the presence of a 400 nm cut-off.*

Under 1 SUN irradiation (λ > 400 nm), the limiting current reached approximately 125 μA/cm^2 in the 0.2-0.7 V range, followed by direct TEMPO oxidation. The chopped photocurrent density-voltage profile showed minimal recombination events, with a 10 times lower current compared to the absence of TBPy (*Figure 16c*), attributed to an increase in the semiconductor Fermi level due to the base. The photoaction spectrum at 0.4 V reverse polarization indicated a maximum APCE of 1% in the Soret region, aligning with the dye's spectral profile. However, the injection quantum yield dropped to 1% in the presence of the base, as revealed by transient absorption spectroscopy. In bulk photoelectrolysis with a Proton Exchange Membrane (PEM), the Faradaic Efficiency (FE%) for benzaldehyde collection reached 85±7%, confirming selective BzOH oxidation. LiTFSI was explored as a milder base, but its slower catalysis compared to TBPy suggested potential improvements on longer timescales. Prolonged photoelectrolysis identified nearly unitary faradaic yield for benzaldehyde, indicating TFSI's effectiveness in

promoting selective oxidation. When the photoanode was in contact with 0.5 M LiTFSI/10 mM TEMPO/70 mM BzOH, a photocurrent of 750 $\mu A/cm^2$ (black line) was recorded (*figure 17c*), which was 6-fold higher than the case in the presence of TBPy (*figure* 17a). Attempts to depolarize the cathode with TFA for enhanced hydrogen evolution resulted in dye desorption, indicating the need for further experiments to find an appropriate proton donor preserving dye stability.

1.4| CONCLUSIONS

In conclusion, in this section, a new set of perfluorinated Zn^{II} porphyrins was rationally designed and synthetized with the aim of enhancing the *push-pull* character of the dyes, and to improve the electron injection from the sensitizer to the metal oxide semiconductor. The designed compounds were made with the purpose of comparing two different *push-pull* structures (3D–π–1A *vs* 4D–π–1A) and to state if the presence of ancillary amino-donor groups could be positive in enhancing the charge injection of the dyes. After the optimization of the synthetic pathways, the UV characterization confirmed the expected red shift of the Soret band for **meso-F16** and **β-F16** due to the addition of electro-donating dimethyl ammino which is responsible of an increase *push-pull* character. Moreover, the 4D–π–1A configuration of **β-F16** displayed enhanced *push-pull* character in comparison to the 3D–π–1A structure of **meso-F16**, where the triazole moiety's presence partially disrupts conjugation, because of his rotation with respect to the molecular plane. The electrochemical analysis suggested that all the porphyrins are equipped with the suitable redox potentials for application in DSPEC as promising sensitizers. The dyes were subsequently sent to the University of Ferrara, where Professor Caramori's team first conducted DFT calculations. These calculations were in accordance with our electrochemical and UV data, reinforcing our findings. Additionally, they assembled DSPEC cells, subjecting them to a thorough examination from a photoelectrochemical standpoint. During the evaluation of the catalytic performances, Professor Caramori's group observed photocurrents of approximately 125 $\mu A/cm^2$ during the optimized TBPy/LiClO$_4$/ACN electrolyte-induced oxidation of BzOH, consistent with existing literature data.[63] They also noted a remarkable increase in photocurrent to around 800 $\mu A/cm^2$ when altering the base and using LiTFSI instead of TBPy. To our knowledge, this represents one of the highest values ever documented for this photoelectrochemical reaction. The work here described is the subject of a paper submitted to *ACS Appl. Mater. Inter.* and now under revision.

SECTION II

PORPHYRINS FOR VOCs SENSING

2.1| VOCs and GAS SENSING

2.1.1 Volatile Organic Compounds (VOCs)

Volatile Organic Compounds (VOCs) constitute a vast group of molecules characterized by their ability to readily evaporate at typical room temperatures. This propensity for rapid vaporization is closely associated with a low boiling point, indicative of the quantity of these molecules in the air. This property is commonly referred to as volatility.[64] The European Union defines a VOC as "any organic compound having an initial boiling point less than or equal to 250°C (482 °F) measured at a standard atmospheric pressure of 101.3 kPa".[65] The classification of VOCs is based on the different functional groups, e.g., halogenated hydrocarbons, alcohols, aldehydes, aromatics, alkanes, ketones, olefins, ethers, esters, paraffins, and sulphur containing compounds. Carbon monoxide, methane and carbon dioxide are excluded from the definition of VOCs. The composition and properties of volatile organic compounds (VOCs) are shaped by their source of release. These sources can be categorized as outdoor sources, exemplified by chemical industries, and indoor sources, represented by household products. The EPA (Environmental Protection Agency of U.S.) has determined that VOC concentrations from indoor sources can be 2 to 10 times higher than those found in outdoor air. [66] The major contributors to VOC emissions encompass the utilization and production of fossil fuels, the usage of solvents in coatings, paints, and inks, the presence of compressed aerosol products like butane and propane, and the combustion of biomass, particularly in rainforest regions.[64] Volatile Organic Compounds originating from diverse natural and human-made sources in the ambient air pose significant threats to both the environment and human health. These compounds are major contributors to problems like smog, ozone layer depletion, and overall air pollution due to their ready dispersal, toxicity, and volatility. Halogenated VOCs exhibit pronounced bioaccumulation potential, acute toxicity, and resistance to degradation. Aldehydes are highly reactive in the atmosphere, while alcohols, primarily ethanol, contribute to the formation of aldehydes through secondary reactions, which in humans can lead to symptoms such as throat irritation, shortness of breath, eye irritation, and chest tightness[66–69] Moreover, many VOCs are highly toxic with potential carcinogenic, mutagenic, and teratogenic effects even at low concentrations.[70] For all these reasons, the monitoring of these compounds

has become mandatory. On the other side, few VOCs are biomarkers of specific illnesses, as they are strictly correlated to several metabolic processes when they are present in the human's breath. For example, acetone, that is contained in breath exhalations, can be considered a biomarker for type I diabetes as its concentration in breath varies from 300 to 900 *ppb* in healthy people to more than 1800 *ppb* for diabetics.[71] In this case, analysis of breath samples for testing VOCs can be helpful in monitoring therapeutic intervention. Breath tests (BTs) are widely employed in different fields of medicine, due to their non-invasive nature, making them particularly well-suited for critically ill patients and young children. Furthermore, they have been proven to be useful for diagnosing a broad range of diseases, including diabetes, gastrointestinal and liver diseases, lung disorders, different types of cancer, and infections.[72] Normally, breath tests (BTs) involve on-site sample collection followed by subsequent laboratory analysis. To reduce both time and costs of this procedure, portable sensors can be highly advantageous.

2.1.2 Gas Sensing and Chemiresistors

A promising solution for the detection and quantification of VOCs, for example for continuous emissions of industrial plants and vehicles but also for non-invasive medical analysis and control,[73,74] consists in the implementation of chemiresistive gas sensors, were n-type semiconductor metal oxide (MOS), like SnO_2, WO_3, ZnO, TiO_2, or graphene oxide (GO), are used as basic elements for detecting gas.[70,75] They offer advantages such as compactness, cost-effectiveness, ease of production, and the ability to detect a wide range of gaseous substances. Despite these merits, these sensors present certain limitations *e.g.*, the necessity of high operating temperatures (200-400℃), limited lifespan, and low selectivity. Consequently, it becomes challenging to selectively analyse multiple substances within complex matrices using these sensors, making them an alternative to traditional, more advanced but also more expensive analytical techniques, like mass spectrometry and gas chromatography.

Chemiresistors have been studied since 1950, when it was demonstrated that some semiconductor materials modify their resistance depending on the atmosphere they are in contact with.[76] The response of a sensor to the analyte is generally a first order time response.[77] The functioning of a sensor starts with exposure of the reference gas (typically simulated air: 80% N_2 − 20% O_2) to the sensor to establish a baseline.

Subsequently, the sensor is exposed to the analyte, leading to a change in its output signal until it stabilizes. Once the analyte is removed from the sensor using the reference gas, the sensor returns to its baseline. The subsequent stage involves adjusting the sensor's response relative to this baseline, effectively mitigating noise, drift, and signals that are inherently either too large or too small. The most popular procedure reported in literature for metal oxide gas sensors is the fractional method[78] in which the gas response ($R_{analyte}$) is subtracted from baseline (R_{air}) and then divided by the response as follows (*equation 3*):

$$\frac{R_{air} - R_{analyte}}{R_{analyte}} = \frac{R_{air}}{R_{analyte}} - 1 \qquad\qquad (3)$$

The elaboration of the signal allows to evaluate two parameters: i) the *response time* (t_{res}) defined as the time needed to reach 90% of the final response and ii) the *time of recovery* (t_{rec}) that is the time taken by the signal to return to the baseline (*figure 18*).
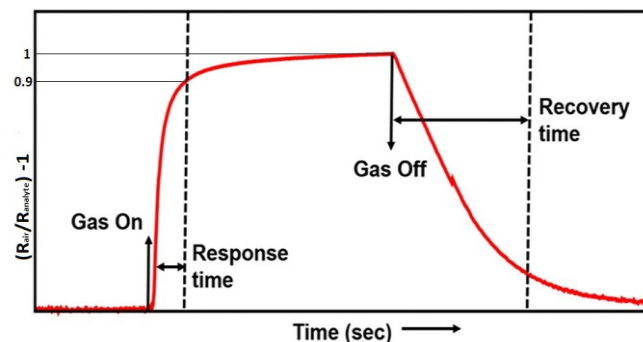
Figure 18: dynamic response curve of a gas sensor - adapted from Langmuir 2020, 36, 6326–6344

Other important parameters are the *sensitivity*, that can be defined as the change in the measured signal per analyte concentration and the *selectivity*, which determines whether a sensor can respond selectively to a group of analytes or even specifically to a single one.[79] A chemiresistive sensor typically consists of interdigitated comb-like electrode structures (IDE) that are coated with coarse granules of sensing powders using an appropriate method. *Figure 19* provides a schematic representation of IDE, which is widely utilized in the realm of chemical sensors because of its affordability, ease of production, and exceptional sensitivity. [78]
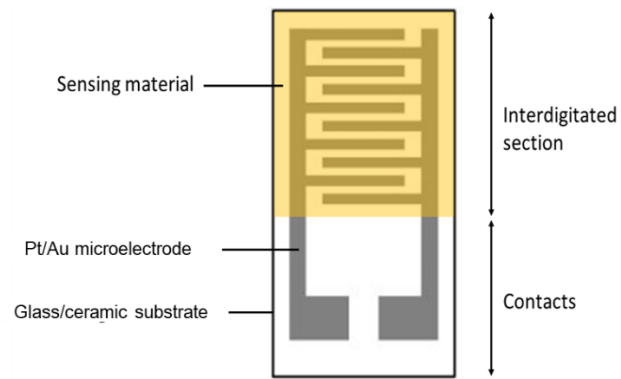
Figure 19: schematic drawing of an IDE[70]

The thickness of the sensing layer usually ranges from micrometres to nanometres and therefore they are called thin films. The deposition of the material on the substrate is accomplished by several methods, that can be grouped in three categories:

- Physical Vapour Deposition (PVD): Vacuum processes that allow the sequence condensed phase-vapor-thin film-condensed phase.

- Chemical Vapor Deposition (CVD): Vacuum processes at usually higher temperature than PVD that allow volatile precursors to react/decompose to the desired product upon exposure of the substrate.

- Solution Based Chemistry (SBC): low temperature, atmospheric pressure methods that create films from a liquid phase.

2.2| DESIGN OF THE PORPHYRIN-SnO$_2$ HYBRIDS

To enhance the sensitivity and the selectivity of chemiresistive sensors towards target compounds and their ability to work at low temperature (ideally room temperature) metal oxides can be coupled with other matrices that can act as sensitizers.[75,80,81] In particular, the main challenges of sensing worsening could be the metal oxide (MOS) high sensitivity to water vapour molecules, interfering species present in the environment (*cross-sensitivity*) together with high temperature dependency and high operating temperatures in the case of bare metal oxides.[82–84] Therefore, in order to address some of these challenges, MOS can be combined with other materials. For example, the combination of SnO$_2$ with Graphene Oxide (GO) has been observed to enhance the sensing capabilities compared to pristine SnO$_2$.[75] However, a significant limitation of graphene is its absence of functional groups, which would facilitate gas adsorption. Graphene itself lacks a band gap and remains unreactive, which diminishes its competitive potential in the semiconductor and sensor domains.[85] GO's drawbacks may be overcome using porphyrins as sensitizers. Indeed, porphyrins have emerged as highly promising materials in the field of chemiresistive gas sensors based on MOS, thanks to their thermal and chemical stabilities, the quite good solubility, and the high structural flexibility, that allow a tailor-made synthesis and a fine tuning of the electronic properties in view of a specific application. They exhibit unique electronic and optical properties that make them well-suited for sensing applications.[86,87] For example, when incorporated into chemiresistors, porphyrins undergo changes in conductivity in the presence of specific VOCs, leading to measurable electrical responses. Photoactive porphyrins exhibit remarkable versatility as ligand platforms, capable of both forming an extensive array of metal complexes and interacting with gaseous molecules through diverse mechanisms.[87] However, leveraging on their chemical versatility, porphyrins can be used to both enhance their hybridization with other compounds (as MOS) and tailor the sensing material's surface, so that the sensitivity, selectivity, and the operating conditions may be improved. Therefore, this section of the thesis introduces the synthesis, characterization, and subsequent combination in different ratio with SnO$_2$ of four porphyrin-based compounds, illustrated in *figure 20*.
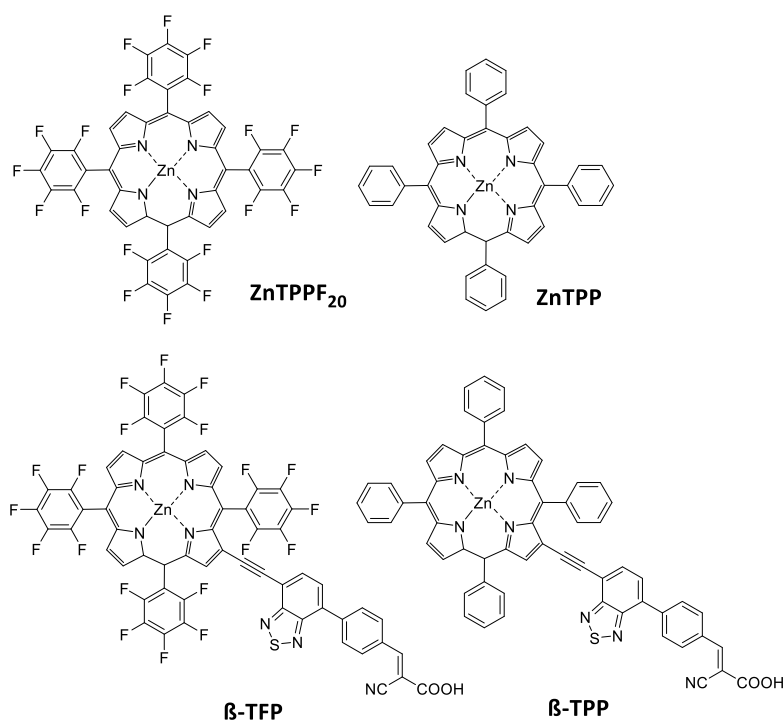
Figure 20: Zn^{II} porphyrins studied for low temperature chemiresistive detection of acetone

Porphyrins in *figure 20* were chosen due to their unique electronic properties. Specifically, Zn(II) 5,10,15,20-tetraphenylporphyrin (**ZnTPP**) exhibits an electron-rich nature owing to the plain aryl groups in the *meso* position, while its perfluorinated counterpart, Zn(II) 5,10,15,20-tetrakis(pentafluorophenyl)porphyrin (**ZnTFP**), possesses an electron-deficient core due to the presence of multiple fluorine atoms. This selection allows for an investigation of the potential impact of the porphyrin's electron properties on the sensing characteristics of the final hybrid materials. Lastly, **β-TFP** and **β-TPP** were included in the assessment to explore the potential influence of a pendant group in the β-*pyrrolic* position. Endowing the macrocycle core in β-*position* with electron-withdrawing groups indeed stabilizes the frontier orbitals and raises the associated potential.[45] Additionally, we considered that the presence of fluorine atoms in **ZnTFP** and **β-TFP** results in an enhanced hydrophobicity, thus leading to a possible reduction of humidity interference**.** The four compounds have been used in the generation of a series of SnO$_2$-porphyrin hybrids in chemiresistive sensors for the detection of acetone at mild temperatures, for a comprehensive comparative study, in collaboration with the research group of prof. Cappelletti at the Univeristy of Milan. The primary objective of this partnership was to develop a compact and wearable device capable of detecting acetone levels to monitor the concentration of this VOC in the breath of diabetic

individuals. To ensure its wearability and portability, the sensor must function effectively at room temperature and remain operational under UV sunlight irradiation. Ultimately, *ab initio* calculations through density functional theory (DFT) were performed to possibly shed light on the chemiresistive mechanism of the synthesized nanocomposites.

2.3| RESULTS AND DISCUSSION

2.3.1 Synthesis

The two Zn[II] porphyrin **ZnTPP** and **ZnTFP**, were obtained performing a metalation reaction with zinc acetate of the commercially available cores, as outlined in *section I*. It should be noted that TPP exhibits a distinct solubility behaviour when compared to TFP. Specifically, it dissolves only in chlorinated solvents and not in alcohols. Consequently, TPP metalation is carried out in a MeOH and CH₃Cl mixture to ensure the solubility of both the free-base porphyrin and the Zn[II] salt. This method ensures that the desired **ZnTPP** is obtained in nearly quantitative yield. The synthesis of **β-TPP** from **ZnTPP**, follows a modified version of the synthetic pathway employed for compound **β-TFP**, which was thoroughly discussed in *section I*, and is outlined in *scheme 5.*
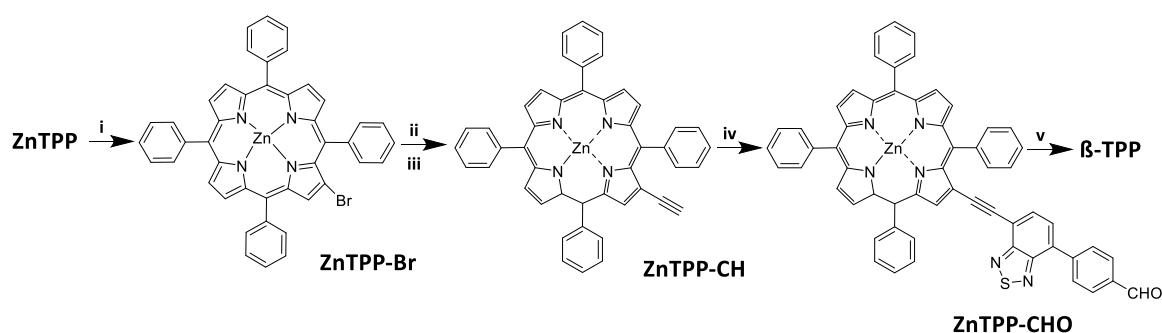
***Scheme 5**: synthesis of* β-*TPP*
i) NBS, CCl₄, reflux, o.n.; vii) THS-CH, Pd(PPh₃)₄, TEA/DMF 120°C, MW; viii) TBAF/THF, r.t. 1h; ix) BTD-1; Pd(PPh₃)₄, TEA/THF; 70°C, o.n.; iv) CAA, CHCl₃/CH₃CN, piperidine, 90°C, o.n

As anticipated, the primary distinction between the porphyrinic cores of **β-TFP** and **β-TPP** lies in their solubility. The presence of perfluorinated phenyl rings in TFP renders the macrocycle slightly more soluble, particularly in alcohols like methanol and ethanol, whereas the TPP core, in contrast, remains insoluble. This disparity not only affects the selection of the reaction solvent, but also affects the purification of various intermediates. In the synthetic pathway of **β-TFP**, nearly every step requires purification through column chromatography, whereas in the case of **β-TPP**, many intermediates can be purified simply by rinsing with methanol. The bromination of **ZnTPP** in β-*pyrrolic* position occurs again by reaction with NBS, this time using CCl₄ as solvent.[62] The crude (70%), insoluble in methanol, was washed with this latter to remove residual NBS and used for a Sonogashira's coupling with trihexylsilylacetylene, in a 3/1 =

triethylamine/N,N-dimethylformammide mixture as solvent and catalytic amounts of [Pd(PPh$_3$)$_4$] and CuI, using a microwave assisted approach (30 *minutes*, 120°*C*).[40,88] In this case, the electron-rich core of ZnTPP-*Br* is less sensitive than the perfluorinated one to high temperatures and nucleophilic reagents, and the product can be easily collected with around 50% yield. After the removal of the protective group with 2 *equivalents* of tetrabutylammonium fluoride, ZnTPP-*CH* was obtained in good yields. BTD-3 (*scheme 2, section I*) was inserted through a second Sonogashira's coupling, heating at 80°*C* for 24*h*. Like in the case of **β-TFP**, this second coupling does not require MW assistance due to the lower steric hindrance of the substrates. The final Knoevenagel condensation between ZnTPP-*CHO* and cyanoacetic acid (CAA), using piperidine as base in 2/1 chloroform/acetonitrile mixture gave **β-TPP** in 50% yield.

2.3.2 Molecular characterization

Spectrophotometric analyses were carried out in order to outline the light-harvesting abilities of all the investigated dyes. The ε-normalized spectra, recorded in tetrahydrofuran (THF) solution, are shown in *figure 21* and the related data are summarized in *table 7*.
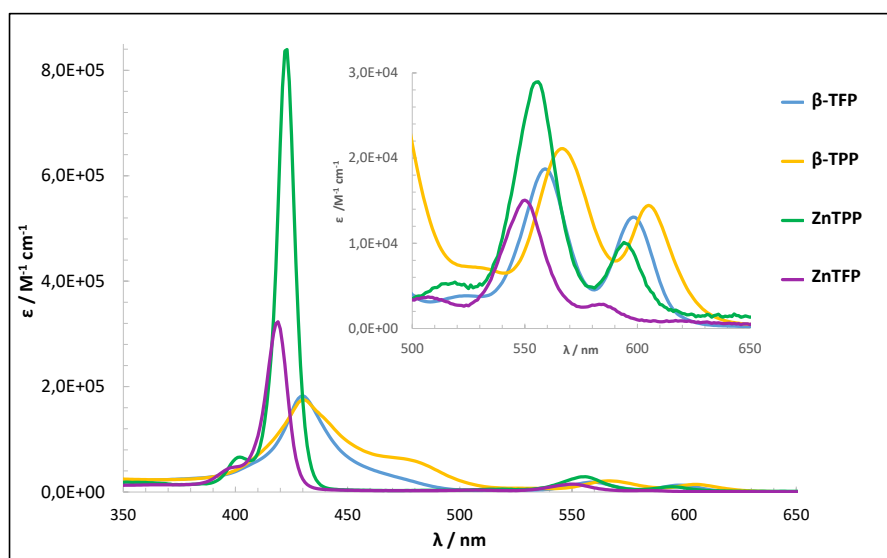

Figure 21: *UV-Vis absorption spectra of the four porphyrins recorded in THF solution*

Table 7: synopsis of the UV-Vis absorption data recorded in THF solution

Entry	λ_b/nm (*logε*)	λ_q/nm (*logε*)
β-TFP	430 (5.27)	560 (4.27)
		600 (4.12)
β-TPP	430 (*5.25*)	566 (*4.33*)
		605 (4.17)
ZnTPP	422 (*5.39*)	555 (5.85)
		594 (3.90)
ZnTFP	419 (5.22)	550 (4.15)
		583 (3.38)

Similar absorption patterns can be observed for **ZnTPP** and **ZnTFP** characterized by the typical presence of a sharp and intense Soret or B band (423 *nm* and 419 *nm* respectively) and the two Q band (557 nm/594 nm and 552 *nm*/586 *nm* respectively). The B band with higher oscillator strength and higher energy state is strongly allowed and can be designated as the $S_0 \rightarrow S_2$ transition (from the ground state to the second excited state). The higher the intensity of the B band, the higher the ability of light-harvesting. Incorporating a benzothiadiazole (BTD) unit into the acceptor pendant at the β-*pyrrolic* position results in the broadening and reduction of the B band, associated with a broader range of wavelength absorption. This effect is evident in dyes **β-TFP** and **β-TPP**, that both exhibit absorption peaks at 431 *nm*. The presence of the cyanoacrylic terminal group accounts for the additional absorption peak at 470 *nm*. As expected, the introduction of the pendant in the β-position creates a more favourable conjugation and charge transfer between the porphyrin-core and the BTD-based anchoring-acceptor moiety, leading to a greater *push-pull* electronic effect. Indeed, a significant red shift of all the bands of **β-TFP** and **β-TPP** compared to those of**ZnTFP** and **ZnTPP,** respectively, is clearly perceivable. Moreover, the fluorination in **ZnTFP** and **β-TFP** is responsible of a blue-shift in comparison with **ZnTPP** and **β-TPP**, due to a greater electron acceptor character and a lower *push-pull* electronic effect. Focusing on the Q bands (generated from the $S_0 \rightarrow S_1$ transition), it is possible to observe how they are weakly allowed. However, the redshift of the Q bands in β-functionalized porphyrins **β-TFP** and **β-TPP** (560 *nm*/600 *nm* and 569 *nm*/607 *nm* respectively) suggests a more favourable conjugation compared with the non-functionalized **ZnTFP** and **ZnTPP** (557 nm/594 nm and 552 *nm*/586 *nm*

respectively). With regard to the potential application of the studied Zn^{II} compounds in sensor fabrication, where the porphyrin is used in powdered form, we conducted an examination of their solid-state absorption properties using UV-Vis Diffuse Reflectance Spectroscopy (DRS). The spectra are shown in *figure 22* and the experimental data are reported in *table 8.*
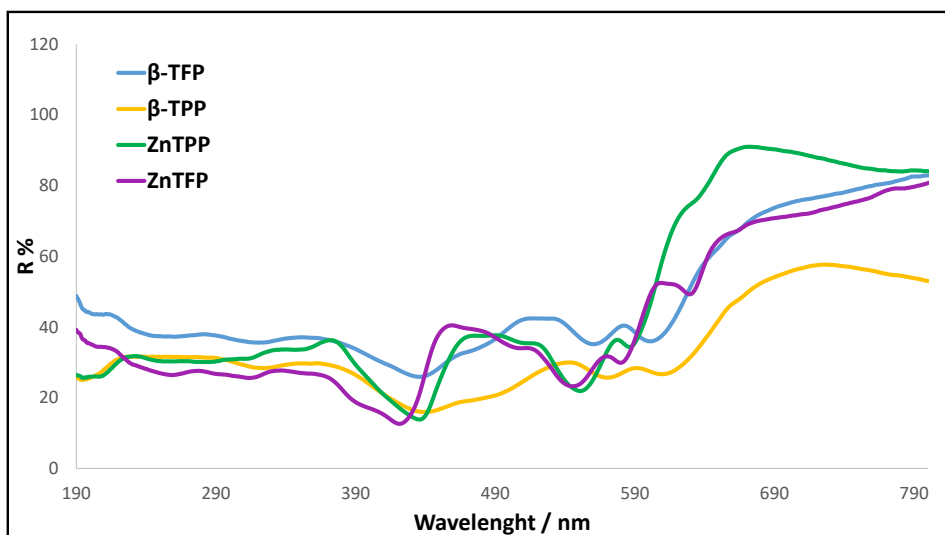
Figure 22: *Diffuse Reflectance spectra of the four porphyrins in powder form*

Table 8: *synopsis of DRS data*

Entry	λ_b/nm	λ_q/nm
β-TFP	439	559
		603
β-TPP	438	574
		613
ZnTPP	427	548
		587
ZnTFP	422	547
		580

The DRS behaviour of the investigated Zn^{II} porphyrins resembled that in THF solution, although the Soret bands appeared slightly red-shifted (Dl = 3-9 *nm*) in the solid state. Non-functionalized **ZnTPP** and **ZnTFP** share the same pattern characterized by a Soret band (427 and 422 *nm*, respectively) and two Q bands (at 548/587 *nm* and 547/580 *nm* respectively). The presence of the fluorinated rings in **ZnTFP** and **β-TFP** led to a hypsochromic shift (Dl = 5-7 *nm*) of all the bands in the spectrum. The introduction of a

BTD unit in **β-TFP** and **β-TPP** promoted a broadening and a reduction in intensity of the B band with respect to the corresponding non-substituted porphyrin. The shoulder at higher wavelengths due to the cyanoacrilic moiety is still perceivable. Finally, both the B and the Q bands of **β-TFP** and **β-TPP** are red-shifted in comparison to those of the not-substituted compounds.

Lastly, thermogravimetric analysis (TGA) was performed to examine the thermal stability of the two porphyrinc cores **ZnTPP** and **ZnTFP** (*figure 23*).
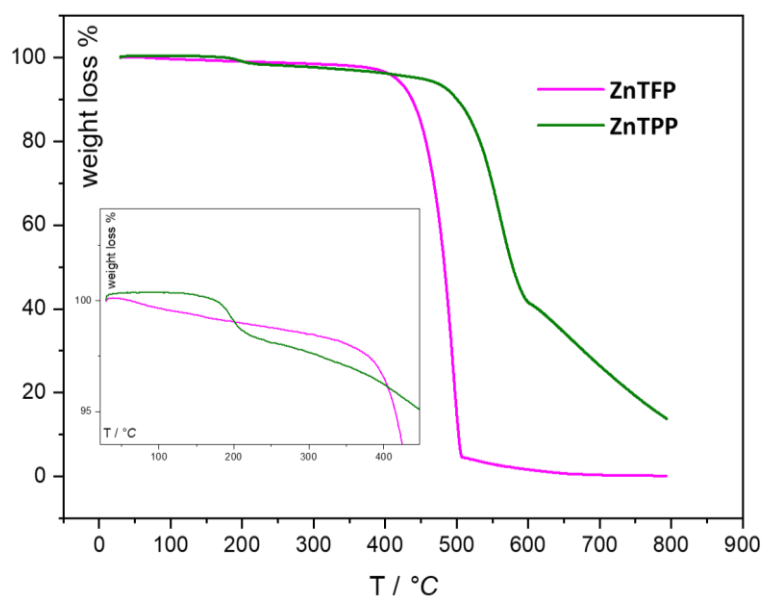
Figure 23: *thermogravimetric analysis of porphyrin cores in air atmosphere, heating rate 10°C/min*

The TGA profile revealed a weight loss of 90% in the range 380-480°C that could be attributed to the complete decomposition of the macrocyclic structure with the formation of ZnO species.[89] In comparison with **ZnTPP**, the curve of **ZnTFP** appeared smoother in the temperature range 25-380°C, and also lacks the step due to the loss of tetraphenyl groups (40% weight loss at 600°C), probably due to the presence of the fluorine atoms, which led to an improved thermal stability.

2.3.3 SnO$_2$-ZnTPP and SnO$_2$-ZnTFP Nanocomposites Sensing Performances

Firstly, we focused our attention on the study of the different electronic impact of **ZnTPP** and **ZnTFP** on sensitization of SnO$_2$-based semiconductor. This stage of the research was aimed at evaluating the impact of incorporating porphyrins in a chemiresistive sensor. To investigate the sensing properties for acetone molecules at moderate operating

temperatures (< 120 $°C$), we fabricated a series of nanocomposites (see *section 5.3* for SnO_2 synthesis and nanocomposite preparation) with different Zn-porphyrin/SnO_2 ratios, specifically 1:4, 1:32, and 1:64, using both **ZnTPP** and **ZnTFP**. The purpose was to determine the most effective combination in terms of sensor performance. To investigate the influence of light on the sensing, the samples were illuminated during the sensing experiments using a LED light source (455 *nm*, power of 2 *W*). Nanocomposites were deposited by a hot-spray method on glass interdigitated platinum electrodes (Pt-IDEs) and sensing tests were carried out using a custom-built stainless-steel cell.[75,90] In particular, the electrode resistance was measured while flowing a simulated air (80% N_2 – 20% O_2) gas mixture (with total flow rate of 0.5 *L min^{-1}*) in the presence of different concentrations of acetone gaseous molecules. The flow of the target analyte was varied by dilution from a starting 500 *ppm* concentration (in N_2 gas mixture) keeping constant the total flow rate. Sensing results both with and without LED light are summarized in *table 9*, where $i_{baseline}$ is the material's current recorded in the absence of acetone molecules, and (R_{air} / $R_{acetone}$ – 1) represents the response intensity relative to the signal at 20 *ppm*.

Table 9: *materials' current values in the absence of acetone molecules ($i_{baseline}$) and response intensity reported as $R_{air}/R_{acetone}$ – 1 relative to the signal at 20 ppm, both with and without LED light.*

	Entry	LED OFF		LED ON	
		$i_{baseline}$ (µA)	$R_{air}/R_{acetone}$ – 1, (intensity at 20 ppm)	$i_{baseline}$ (µA)	$R_{air}/R_{acetone}$ – 1 (intensity at 20 ppm)
1	**SnO$_2$**	3	0.60	9	0.55
2	**ZnTPP/SnO$_2$ 1:64**	38	0.29	50	0.33
3	**ZnTPP/SnO$_2$ 1:32**	64	0.10	53	0.30
4	**ZnTPP/SnO$_2$ 1:4**	1700	n.d.	1700	n.d.
5	**ZnTFP/SnO$_2$ 1:64**	5	0.70	8	0.72
6	**ZnTFP/SnO$_2$ 1:32**	20	1.80	10	0.80
7	**ZnTFP/SnO$_2$ 1:4**	610	n.d.	620	n.d.

Initially concentrating on dark conditions (LED off), it is notable that for both **ZnTPP** and **ZnTFP**, at porphyrin/SnO_2 weight ratio of 1:4 (entry 4 and 7, 2nd column) no discernible response upon purging the target volatile organic compound (VOC) is seen, consistent with prior observations that the porphyrins alone exhibited negligible sensing behaviour. Upon thorough examination of the acquired data, it becomes apparent that the two **ZnTPP**-based nanocomposites with ratios of 1:64 and 1:32 (entry 2 and 3, 2nd column), worsen the sensing performance of pristine SnO_2 (entry 1, 2nd column), particularly as the porphyrin content in the nanocomposite increases. In contrast, the presence of **ZnTFP** exerts a significantly different influence on the performance of metal oxide semiconductor (MOS). Notably, the 1:64 (entry 5) and 1:32 (entry 6) ratios exhibit heightened sensing responses compared to bare SnO_2, with the 1:32 ratio showing very high results. This particular sample demonstrates a remarkable three-fold increase in signal at a specified 20 *ppm* concentration (rising from 0.6 in pristine SnO_2 to 1.8). In general, higher sensing signals were consistently recorded for all investigated acetone concentrations down to 200 *ppb* (see *figure 24*).
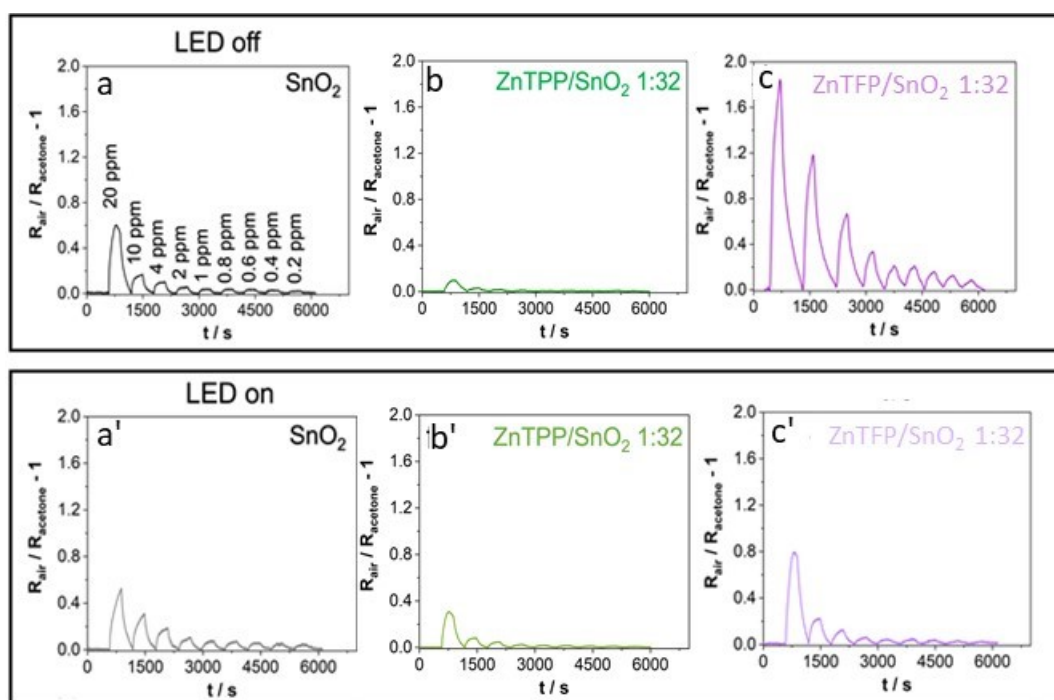

Figure 24: sensors' responses of pristine SnO2 and 1:32 porphyrin/SnO2 composite toward acetone both with and without LED light, under simulated air at 120°C

To clarify the notable differences among nanocomposites of different porphyrins and varying porphyrin/SnO_2 ratios, we conducted a comprehensive analysis of electrode

currents in a simulated air environment (referred to as baseline current hereafter). This examination was performed after system stabilization and before introducing acetone molecules into the sensing chamber. An overview of the collected data is presented in *table 9*, 2nd column. In general, the presence of both porphyrins results in an increase in baseline current compared to SnO$_2$ alone. Notably, this increase is more pronounced in the case of **ZnTPP**, and as more porphyrin is added to the composites, the current steadily rises. A similar trend is observed for **ZnTFP**-based samples, though the absolute values are lower than those of **ZnTPP**, as expected due to the higher mass of **ZnTFP** and its reduced electron transfer tendency, as supported by theoretical calculations (*see next paragraph*). When the LED illuminated the electrodes throughout the sensing measurement, a distinct behaviour was observed. As expected, pristine SnO$_2$ exhibited a slight increase in its baseline current, as the fixed wavelength of approximately 455 *nm* does not match the SnO$_2$ band gap (around 3.6 *eV*) and does not facilitate electron promotion from the valence band to the conduction band, resulting in limited enhancement of the system's conductivity. However, also in the other cases, no exceptional signal improvement was evident. For the **ZnTPP**-based nanocomposites, there were no notable observations, and the trends in both baseline currents (*table 9*, 4th column) and signal intensities (at 20 *ppm*; *table 9*, 5th column) mirrored those in dark conditions. Conversely, in the case of **ZnTFP**-based composites (*figure 24*c and *figure 24c'*), LED light appeared to predominantly degrade the behaviour of the 1:32 ratio. This suggests its potential promising applicability in handheld sensors, as it can provide an optimal signal even without the need for a light source. Furthermore, in addition to signal intensity, two other key parameters are essential in assessing a chemiresistor's performance: the *response time* (t_{res}) and *recovery time* (t_{rec}). In this study, all the compounds examined exhibited similar values, with average t_{res} of approximately 120-150 *seconds* and a t_{rec} of around 200-220 *seconds*. These values align well with existing literature data for chemiresistors operating at temperatures below 150 *°C*.[91]

2.3.4 Theoretical Investigation of Sensing Mechanism

In an attempt to understand the sensing mechanism and properties of the synthesized nanocomposites, in collaboration with doctor R. Soave and doctor M. Trioni of CNR, performed *ab initio* calculations using density functional theory (DFT). Initially, we

simulated SnO$_2$ in its bulk form and its stoichiometric (110) surface, which is known to be stable.[91,92] We then examined the structures of the **ZnTPP**/SnO$_2$ and **ZnTFP**/SnO$_2$ aggregates. Our computational setup proved reliable, at first, for bulk and (110) SnO$_2$ surface modelling, so we then considered the Zn-porphyrins adsorption. We calculated the adsorption energy, which turned out to be approximately 3.55 *eV* for **ZnTPP** and 4.12 *eV* for **ZnTFP**, compatible with physisorption. *Figure 25* shows the *ab initio* optimized structures of the two nanocomposites:
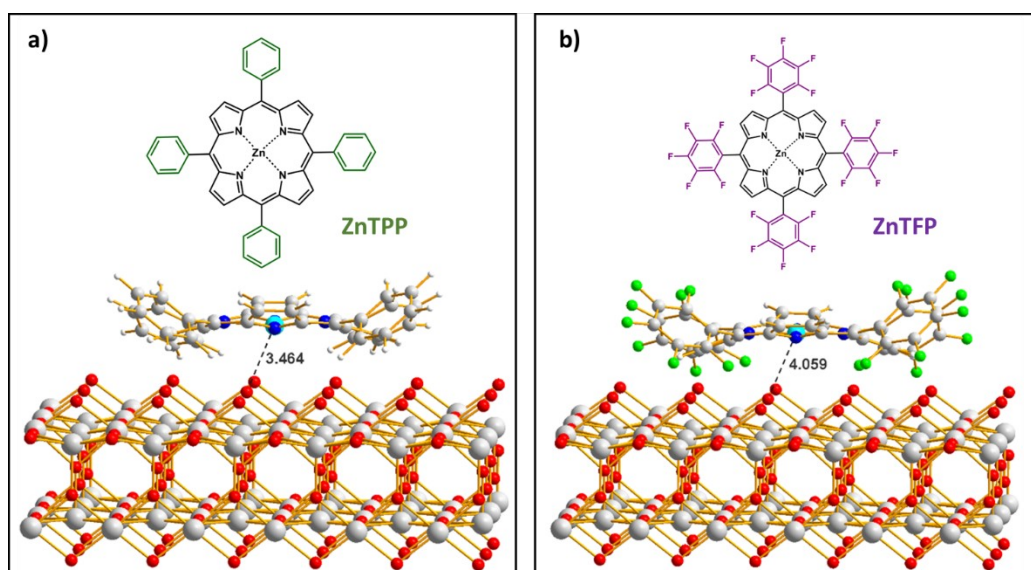
***Figure 25:** Ab initio optimized structures of the (a) ZnTPP/SnO$_2$ and (b) ZnTFP/SnO$_2$ nanocomposites with the relative chemical structure. The shortest Zn-O distances (in Å) are shown as dashed lines.*

Subsequently, we assessed charge transfer using Bader's theory, revealing that **ZnTPP** donates 1.23 electrons when physisorbed on the tin dioxide surface, while **ZnTFP** donates only 0.78 electrons, aligning with their electronic properties. Indeed, the crucial difference between the two systems lies in the slight change in energetic levels. In the case of non-fluorinated porphyrin, the Fermi level is slightly higher in energy, resulting in increased conduction band occupancy and charge transfer. To sum up, **ZnTPP** is more inclined to donate electrons to the SnO$_2$ surface than **ZnTFP**, likely due to the electron-withdrawing nature of fluorine atoms of the latter. Integrating the empirical observation with the theoretical calculations revealed that the combination of SnO$_2$ with **ZnTPP** diminishes acetone sensing properties due to its tendency to inject more electrons upon physisorption onto the SnO$_2$ surface, suggesting that an excessive electrons injection into the MOS conduction band may not always benefit gas sensing properties. On the

contrary a moderate injection of electrons, as in the case of **ZnTFP**-based nanocomposites, resulted in enhanced signals compared to pure SnO_2. Being the sensing response strongly dependant on the difference of resistivity measured in presence of analyte compared with air (baseline), if the porphyrin injects too many electrons into SnO_2, acetone won't be able to donate its electrons, by leading to a negligible change in the sensor's conductivity and resistivity. This could be the case for **ZnTPP**, that saturates the available states and prevents interaction with the target analyte. Regarding the different ratios, when the porphyrin concentration is too low (*i.e.*, 1:64), insufficient electron injection occurs to not benefit sensing and sensing is suppressed, while at high porphyrin concentration (*i.e.,* 1:4), excessive electron injection saturates all accessible states, worsening again the performance. Thus, achieving a balance between electron injection and accessible MOS states is crucial and can be attained by tailoring porphyrin chemistry and adjusting the porphyrin-to-MOS ratio.

2.3.5 SnO_2-β-TPP and SnO_2-β-TFP Hybrids: Influence of the β-Functionalization

In order to investigate the effect of surface sensitization, in a second stage of the study we focused our attention on preparing nanocomposites in which the porphyrins are chemisorbed onto SnO_2 rather than physisorbed. Our objective was to uncover whether the incorporation of a linker at β-*pyrrolic* position showing an anchoring functionality could offer additional advantages in the interaction between SnO_2 and porphyrin, potentially leading to enhanced acetone sensing capabilities. This was based on the possibility for a chemical bond to form between the SnO_2 surface and the terminal cyanoacrylic group of the β-*pyrrolic* pendant. It's important to note that the results we've obtained so far are preliminary and subject to further investigation Upon initial observation, it appears that β-TFP consistently delivers superior results across all tested conditions. Notably, *figures 26* illustrate that, in the SnO2/porphyrin ratio of 1:32, β-TFP/SnO2 outperforms ZnTFP/SnO2 in both illuminated and dark settings. This may be attributed to a more effective coupling with the metal oxide.
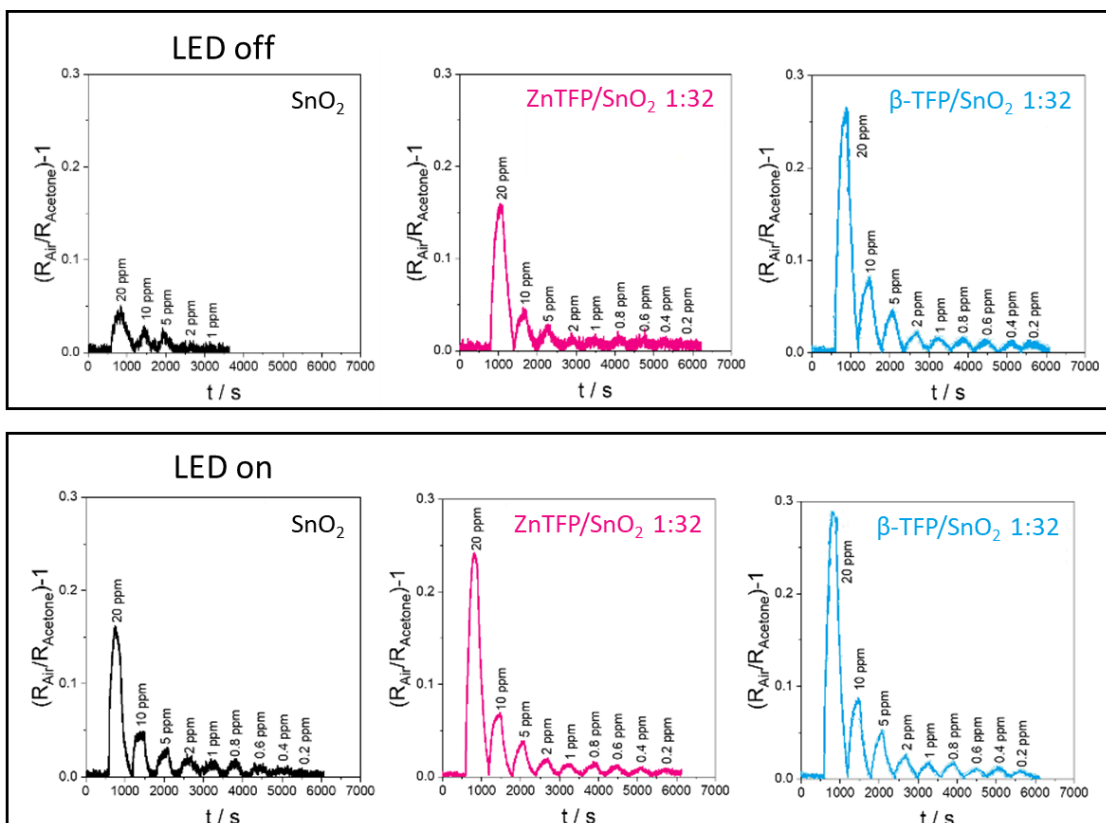
Figure 26: sensors' responses of pristine SnO2 and 1:32 porphyrin/SnO2 composite toward acetone both with and without LED light, under simulated air at 120°C

Conversely, β-TPP does not appear to yield any notable enhancements in the sensor response when compared to unsubstituted ZnTPP, whether in the presence or absence of LED light. As depicted in *figure 27*, it even seems to exhibit rather weak response values, potentially due to a significantly elevated baseline, as previously discussed for the unsubstituted ZnTPP.
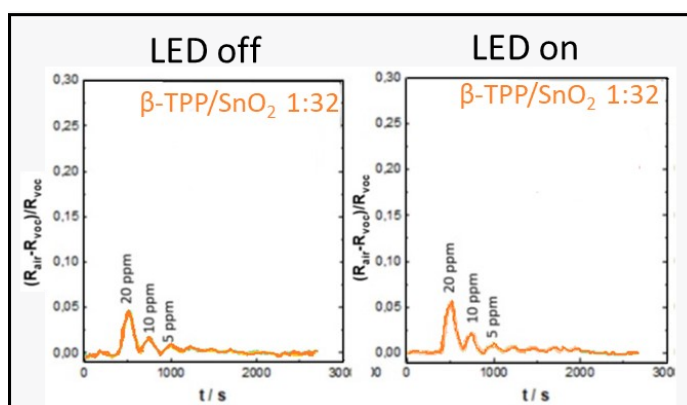
Figure 27: sensors' 1:32 porphyrin/SnO2 composite toward acetone both with and without LED light, under simulated air at 120°C

It is crucial to reiterate that the findings presented in this section are subject to ongoing assessment, and they necessitate validation through additional experiments and theoretical calculations. Thus far, it appears that the overall behaviour of the unsubstituted porphyrins remains consistent, with the perfluorinated analogue outperforming the non-fluorinated porphyrin, while the presence of the pendant group may prove advantageous, particularly in the case of **β-TFP**.

2.4| CONCLUSIONS

In this *section*, we delved into the synthesis and characterization of four distinct porphyrins namely **ZnTPP**, **ZnTFP**, **β-TPP** and **β-TFP**.

In the initial phase of the investigation, SnO_2 nanoparticles were combined with **ZnTPP** and **ZnTFP** at three distinct Zn-porphyrin/ SnO_2 weight ratios (1:4, 1:32, and 1:64). The 1:32 ratio proved optimal for ZnTFP, demonstrating superior performance compared to pristine SnO_2. In fact, by integrating experimental results with DFT calculations, we uncovered a distinctive electron-donating behaviour for the two macrocycles when interacting with SnO_2 semiconductor. Our findings revealed that in cases where the metal oxide semiconductor (MOS) is electron-rich, the oxidation of acetone molecules upon interaction with its surface could be significantly impeded. Consequently, the perfluorinated porphyrin **ZnTFP**, which donates a lower number of electrons compared to **ZnTPP**, could prevent the saturation of available electronic states in SnO_2. This, in turn, enhanced the nanocomposite's conductivity, ultimately improving its sensing capabilities. In summary, we evidenced importance of achieving a delicate balance between porphyrin electron injection and available MOS states for optimal sensor performance. This crucial equilibrium can be attained by customizing the chemistry of the porphyrins and adjusting their ratio with MOS. To further explore the subject, we extended the study in its final phase to include ancillary functional groups in the β-pyrrolic position, such as **β-TFP** and **β-TPP**. Although results in this regard are still pending, we hope that this investigation will enhance our understanding of the interaction between SnO_2 and porphyrins. These collective findings hold the potential to yield a sensor capable of operating at ambient temperature, despite the fact that, based on current results, we have significantly improved sensing performance. The discoveries outlined in this section have been condensed into a manuscript, which has been submitted to *ACS Appl. Mater. Inter*. and is currently undergoing revision.

SECTION III

PORPHYRINS AS CATALYSTS

FOR CO$_2$ REDUCTION

3.1| ELECTROCHEMICAL REDUCTION OF CO_2

3.1.1 CO_2 Emission and Carbon Neutrality

In the present day, one of the most pressing global concerns is the emission of greenhouse gases, with a particular focus on CO_2, as the primary cause of climate change resulting in extreme weather conditions worldwide. It's widely acknowledged that urgent emissions reduction is essential to avert the most severe consequences of climate change.[93] The European Union has taken a resolute stance on climate policy as outlined in the Green Deal, with the ambitious objective of becoming the first continent to offset its CO_2 emissions entirely by 2050, a goal commonly referred to as "Carbon Neutrality." This commitment gained legal force with the adoption of the Climate Law by the European Parliament and Council in 2021. Furthermore, the EU has updated its interim target for emission reduction by 2030, raising it from 40% to a minimum of 55%. As illustrated in *figure 28*, CO_2 emissions have been steadily increasing since the latter half of the 19th century.
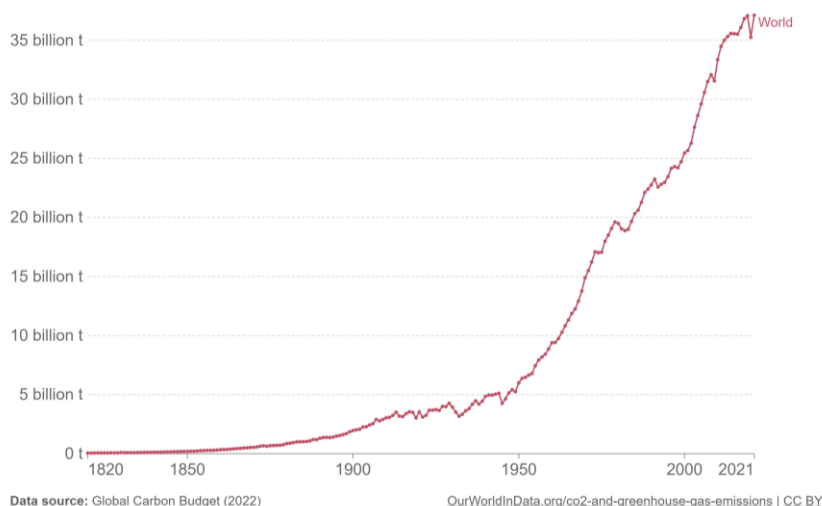

Figure 28: *annual CO_2 emissions from fossil fuels burning and emitted directly from industrial process*

Achieving net-zero emissions necessitates a global effort to balance all greenhouse gas (GHG) emissions with carbon sequestration. In nature, the so-called natural sinks *e.g.,* soil, forests and oceans can remove between 9.5 and 11 *gigatons* of CO_2 per year, but

annual global CO_2 emissions reached 37.8 *gigatons* in 2021.[94] In this frame, one of the approaches to mitigate CO_2 from the atmosphere should involve capturing it and converting it into higher-value products such as CH_4, $HCOOH$, CH_3OH, and CO. In this way it is possible, not only to generate revenue from CO_2 feedstocks while reducing emissions, but simultaneously to reduce dependence on oil and natural gas for chemical and fuel productions.[95]

3.1.2 Electrochemical Reduction of CO_2 to CO

The activation of CO_2 requires high energy, due to the great stability of the two identical C=O double bonds that form the molecule. Up to now, considerable research efforts have been devoted to converting CO_2 into other carbon compounds, and the electrochemical CO_2 reduction reaction (CO_2RR) is especially appealing, since it can be implemented under room temperature and atmospheric pressure but has also good compatibility and complementarity with renewable energy sources. As the price of renewable energy sources falls, the solution of carbon recycling on the basis of the electrochemical CO_2RR holds great promise.[95,96] In order to overcome the great thermodynamics and kinetics barriers, and the CO_2 significant chemical inertness, catalysts become indispensable. Depending on the electrocatalyst employed, a diverse range of products can be generated, including CO and HCOOH, as well as more complex C_{2+} products like ethylene and various alcohols. The production of single-carbon products is comparatively straightforward to regulate, and high-efficiency CO_2R to CO is presently advancing towards commercial implementation.[97–99] Indeed, CO, despite being known mainly for its high toxicity, has many industrial uses like meat colouring, nickel purification or as a reducing agent.[100] The primary research challenge lies in achieving selectivity, given that multiple reactions take place at very similar potentials, rendering it intricate to steer the reaction towards a specific product:[101,102]

$$CO_2 + 2H^+ + 2e^- \rightarrow CO + H_2O \qquad E^0 = -0.77\,V\,(pH\,7, vs\,SCE)$$
$$CO_2 + 8H^+ + 8e^- \rightarrow CH_4 + 2H_2O \qquad E^0 = -0.48\,V\,(pH\,7, vs\,SCE)$$
$$CO_2 + 6H^+ + 6e^- \rightarrow CH_3OH + H_2O \qquad E^0 = -0.62\,V\,(pH\,7, vs\,SCE)$$
$$CO_2 + 2H^+ + 2e^- \rightarrow HCOOH + H_2O \qquad E^0 = -0.85\,V\,(pH\,7, vs\,SCE)$$
$$2H^+ + 2e^- \rightarrow H_2 \qquad E^0 = -0.65\,V\,(pH\,7, vs\,SCE)$$

In this frame, iron porphyrins, when electrochemically reduced to the Fe(0) state, rise as exceptionally well-suited candidates among the available compounds for the purpose of selectively transforming CO_2 into CO.[103] *Figure 29a* highlights **FeTPP** as a benchmark in this particular field. Notably, this porphyrin possesses the simplest structure while demonstrating remarkable stability, as well as catalytic and photocatalytic properties.[104,105] These attributes render it highly suitable for a range of applications in chemical research and industrial production.[106] *Figure 29b* presents the catalytic reduction of CO_2 by **FeTPP.**
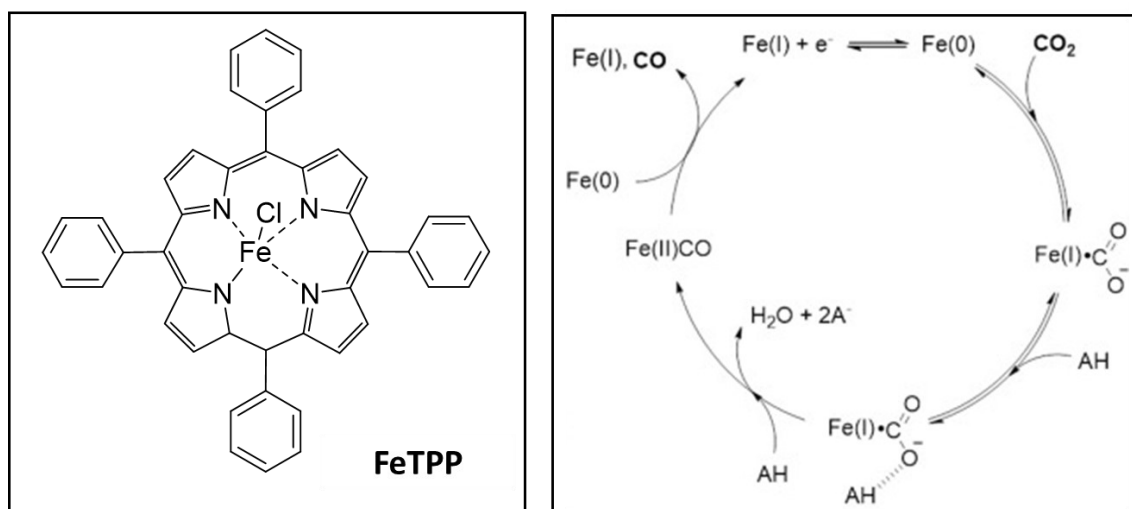
Figure 29: a) FeTPP and b) mechanism for the CO₂-to-CO conversion[107]

Within the catalytic cycle, Fe(III) undergoes electrochemical reduction to form Fe(0), which can readily bond with CO_2, resulting in the formation of the adduct [Fe(I)-$CO_2^{\cdot-}$]. This particular species is further stabilized through hydrogen bonding with a molecule of a weak acid, denoted as AH. The subsequent step entails the protonation of an oxygen atom by a second acid molecule, ultimately leading to the cleavage of a C-O bond and the creation of [Fe(II)-CO]. Lastly, the adduct is reconverted into Fe(I) through a one-electron homogeneous reduction process, releasing CO in the process. Indeed, weak Brönsted acids such as water, trifluoroethanol, phenol or acetic acid have been shown to considerably enhance catalysis, while stronger acids, like protonated triethylamine, promote hydrogen evolution.[107] *Figure 28* shows the general case of CO_2 reduction with **FeTPP**, but, as extensively elucidated in earlier sections of the thesis, porphyrins exhibit remarkable versatility, enabling meticulous tailoring of the macrocycle structure. In the

pursuit of developing an efficient and selective catalytic system, the fine-tuning of the simple **TPP** structure empowers the adjustment of attributes such as solubility in different solvents, refinement of redox potentials, and fostering interactions between the porphyrin and the substrates engaged in the reaction.

3.1.3 Non-Covalent Interaction in Catalysis Boosting

In recent years, numerous studies have pointed out the significance of peripherical substituents within the porphyrins' structure specifically in enhancing the interaction between CO_2 and the iron atom at the centre of the macrocycle to boost the catalytic activity.[108–112] Some examples of porphyrins showing proper functionality specifically designed to promote interaction with CO_2, gave better catalytic results in comparison with **FeTPP** and are reported in *figure 30a*:
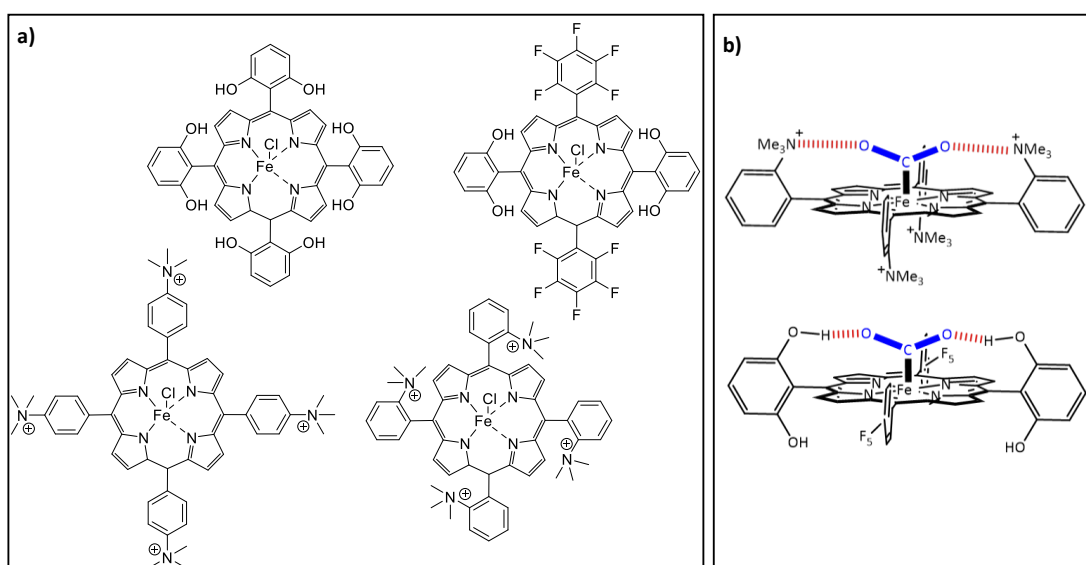
Figure 30: a) examples of iron porphyrins able to establish through-space interactions b) schematic representation of coulombic (above) and hydrogen (below) interaction between CO_2 and porphyrin

Notably, these compounds possess functional groups capable of establishing hydrogen bonds or coulombic interactions with the CO_2 molecule, particularly when inserted into ortho-ortho' positions of the *meso*-phenyl rings of the porphyrins. These types of interactions, often referred to as "*through-space* interactions," play a pivotal role in optimizing the orientation and facilitating improved interaction between CO_2 and the porphyrin catalyst (*figure 30b*). Among the non-covalent interactions that can be involved in *through-space* interaction halogen bonding has been steadily capturing the

attention of the scientific community. Halogen bonding is formally defined by the IUPAC as "a net attractive interaction between an electrophilic region associated with a halogen atom within a molecular entity and a nucleophilic region within another, or the same, molecular entity" and the volume of publications on this subject has witnessed a significant surge in recent years.[113] A schematic representation of the interaction is provided in *figure 31a*.
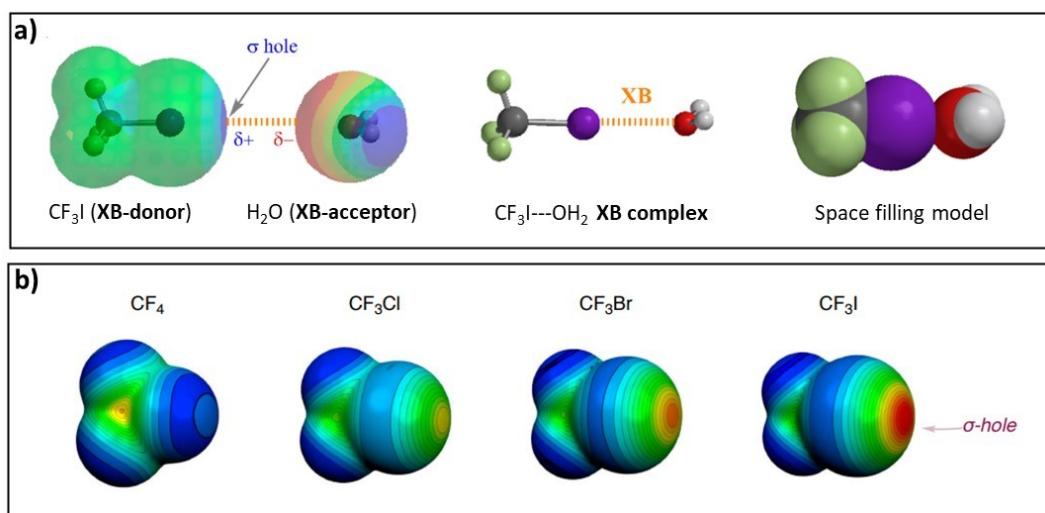
Figure 31: a) electrostatic model of halogen bond (XB) formation between CF_3I (XB-donor) and H_2O (XB-acceptor) used as example; b) isodensity surface of CF_4, CF_3Cl, CF_3Br and CF_3I

The strength of XB is correlate with magnitude of the *σ-hole* on the halogen atom, that increases with his polarizability (F < Cl < Br < I),[114] as shown in *figure 31b*. In nature XB has been identified in biological system as one of the responsible of the 3D conformation of proteins and other complex structures[115] and its exploitation is used in different fields, going from drug design[116] to molecular recognition[117] and catalysis[118].

3.2| DESIGN OF THE CATALYSTS

Given the increasing interest in halogen bonding within the scientific community and the urgent need for the development of selective and efficient catalysis for CO2RR, this section delves into the idea of utilizing porphyrins with halogen substituents. Indeed, these substituents may engage in interactions with CO_2 through halogen bonding. Developed in collaboration with the "*Laboratoire Electrochimie Moleculaire*" (LEM) at Université Paris Cité, the central concept explores whether halogen bonds can enhance catalysis, akin to the role played by hydrogen bond donor groups or groups capable of inducing coulombic interactions, as discussed above. In this field, Professor Robert from LEM is a prominent authority, conducting extensive research on *through-space* and *through-structure* effects.[119–121] Simultaneously, Dr. Fave has pioneered the exploration of halogen bonding across various domains.[117,122] Under their guidance, I had the opportunity to immerse myself in this subject, gaining profound insights into electrochemical techniques, which will be further elaborated upon in the subsequent sections. Considering the fundamental principles of halogen bonding (XB) discussed earlier, our initial concept focused on creating a novel series of iron porphyrins featuring iodine substituents. This strategic design aimed to leverage the most potent halogen bonding donor within the halogen series. The molecular structurers of the designed porphyrins are reported in *figure 32*.
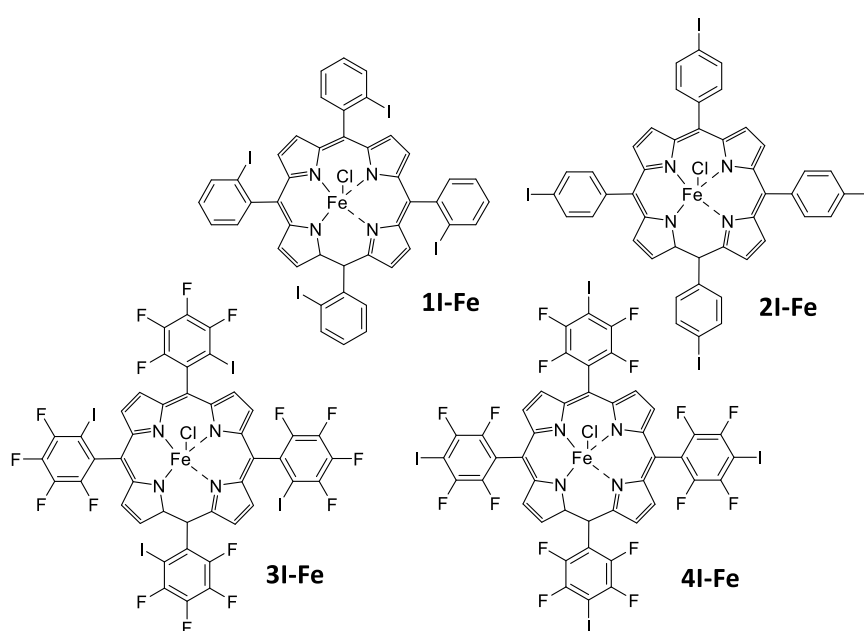
Figure 32: *iron porphyrins bearing iodine substituents as halogen bond donor*

All four porphyrins feature four iodine substituents strategically positioned either in the *ortho* or *para* positions of the *meso*-phenyl ring. Notably, porphyrins **3I-Fe** and **4I-Fe** are additionally characterized by a perfluorinated structure, intended to enhance the σ-hole on iodine through the electron-withdrawing properties of the fluorine atom. Upon their synthesis, we promptly subjected these porphyrins to cyclovoltammetry (CV) in DMF solution to provide a comprehensive assessment of their reduction potentials. As previously illustrated in *figure 29b*, the initial step in the catalytic process for CO_2 reduction involves the electrochemical reduction of the iron atom at the centre of the porphyrin. This reduction process occurs in three successive stages, gradually transitioning the iron atom from Fe(III) to Fe(0) oxidation state. The Fe(0) species is indeed the only one capable of interacting with CO_2 and initiating the catalytic cycle. The attainment of Fe(0) porphyrins entails the application of increasingly negative potentials to the solution. During this voltage scan, it is possible to observe in the cyclic voltammetry (CV) graphs that a peak appears for each of the successive reduction of iron from Fe(III) to Fe(0) state. Although, through experimentation with this set of porphyrins, an unexpected phenomenon emerged: prior to achieving the desired Fe(0) active species, it was observed that the porphyrins underwent cleavage of the carbon-iodine bond (*figure 33*).
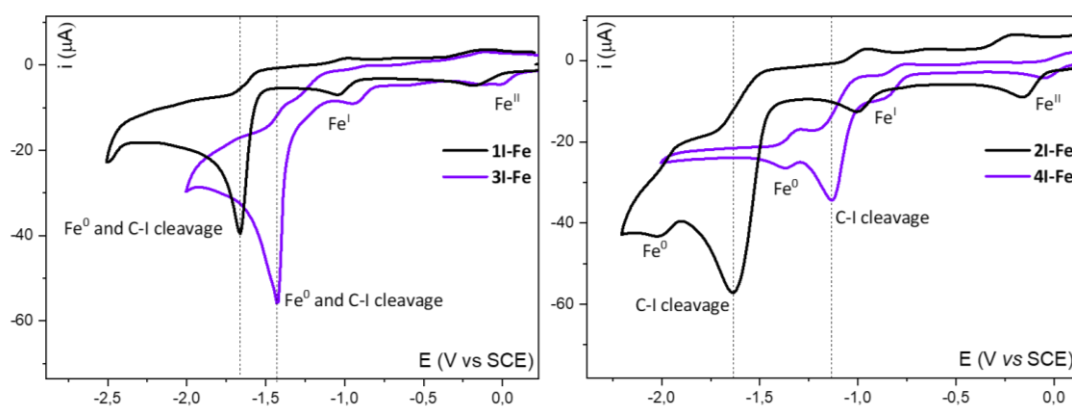
Figure 33: *cyclic voltammetry of porphyrins **1-4** in DMF solution*

This unexpected event implies that assessing the influence of halogen bonding on the catalytic activity of these compounds is unfeasible, as the halogen atom is removed from the porphyrins prior to their activation. In light of the previous unsuccessful attempts, we made the strategic decision to shift our focus towards a different set of porphyrins.

Thus, we decided to replace the iodine atoms with the more stable bromine as halogen bond donor groups. Although iodine promotes stronger XB-interaction, carbon-bromine bond is notably stronger, thus resulting in more stable porphyrins even at the negative potential required to generate the Fe(0) species. To enhance the σ-hole on bromide, these porphyrins also feature various electron-withdrawing substituents at the *ortho* or on the *para* positions of the phenyl ring (*figure 34)*.
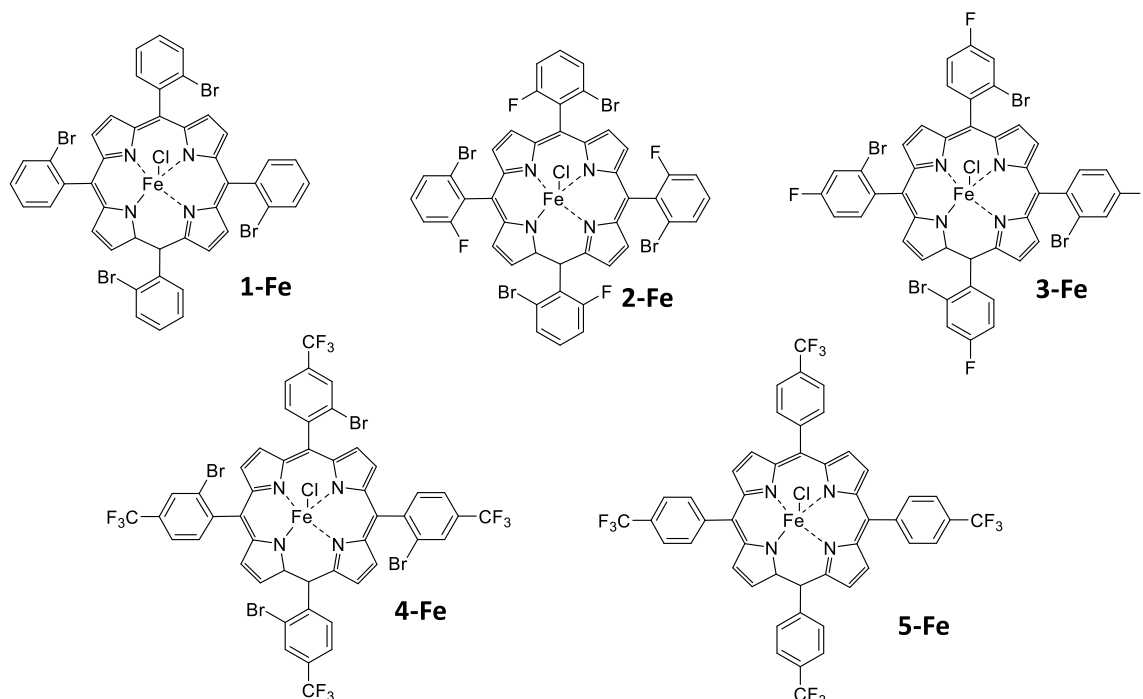
Figure 34: *iron porphyrins bearing bromide substituents as halogen bond donor*

Porphyrin **5-Fe**, lacking any bromide or other halogen bond donor, serves as a benchmark to compare the performance of **4-Fe**. In fact, owing to the presence of the potent electron-withdrawing CF$_3$ group, **4-Fe** is expected to exhibit the most significant σ-hole on bromide, thereby likely enabling the strongest halogen bonding. The initial assessment of these porphyrins using cyclic voltammetry techniques revealed their enhanced stability and their ability to reach the required negative potentials for Fe(0) species formation. However, it's crucial to emphasize that porphyrin **2-Fe** does not exhibit this behaviour, as it undergoes cleavage of the bromine before Fe(0) species generation. Consequently, porphyrin **2-Fe** was excluded from the study. Moving forward, the remaining four porphyrins, which demonstrate stability under the specified conditions, underwent a comprehensive evaluation of their electrochemical

performance and catalytic activity in subsequent sections. To gain a more profound insight into the experimental results, a theoretical investigation employing DFT was also carried out.

3.3| RESULTS AND DISCUSSION

3.3.1 Synthesis

The synthesis of iodinated porphyrins **1I-Fe – 4I-Fe** is reported in *scheme 6*.
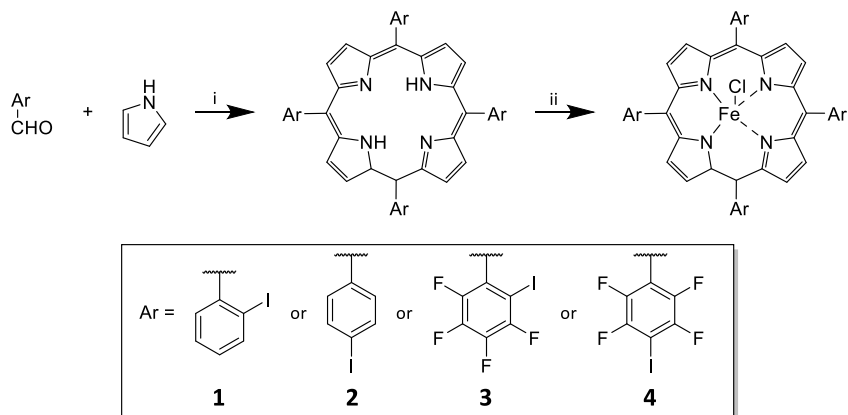
Scheme 6: *synthesis of porphyrins bearing iodine as XB donor*
i) 1. BF3(EtO)₂, DCM, 1h; 2. DDQ, 3h; 3. TEA, overnight. ii) FeCl₂, DMF, 120°C, MW, HCl

Although the final compounds **1I-Fe – 4I-Fe** will not be discussed in the subsequent sections, the synthesis is included here to acknowledge the substantial efforts it entailed. To produce compounds **1I-Fe** and **2I-Fe**, the initial reagents were freshly distilled pyrrole, as well as commercially available 2-Iodobenzaldehyde and 4-Iodobenzaldehyde, respectively. The cyclization process was carried out using the traditional acid catalized protocol,[17] and the free base porphyrins **1I-4I** were obtained in 15-30% yield. The subsequent metalation process was accomplished using a microwave-assisted procedure, significantly faster in comparison to the conventional thermal method.[123] To yield the desired Fe(III) catalysts, the products were treated with HCl, resulting in the precipitation of the Fe(III) porphyrin chloride complexes from the DMF solvent, in almost quantitative yield. The method for obtaining compounds **3I-Fe** and **4I-Fe** is quite similar, but the initial aldehydes are not readily available commercially. Therefore, they were synthesized through the steps outlined in *scheme 7* for 2,3,4,5-tetrafluoro-6-iodobenzaldehyde.
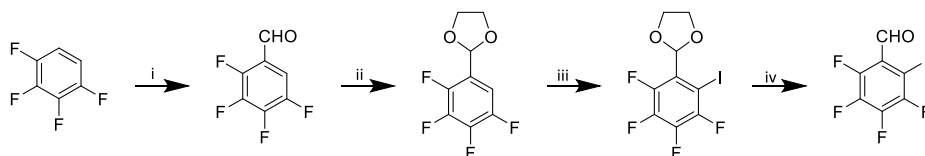
Scheme 7: synthesis of porphyrins bearing iodine as XB donor
i) nBuLi, ethyl formate, -78°C, THF, Ar; ii) glycerol, toluene, p-TsOH, TEA; iii) nBuLi, I₂, -78°C, THF, Ar;
iv) HCl, acetic acid

2,3,4,5-tetrafluoro-6-iodobenzaldehyde and 2,3,5,6-tetrafluoro-4-iodobenzaldehyde, obtained with an analogue procedure starting from 1,2,4,5-tetrafluoro benzene, where then used with freshly distilled pyrrole in the one-pot Lindsay method with $BF_3(EtO)_2$ as outlined in *scheme 6* The brominated porphyrins **1-Fe – 5-Fe** were obtained with the same procedure, followed by microwave assisted metalation. The starting aldehydes are all commercially available. *Scheme 8* outlines the synthetic route:
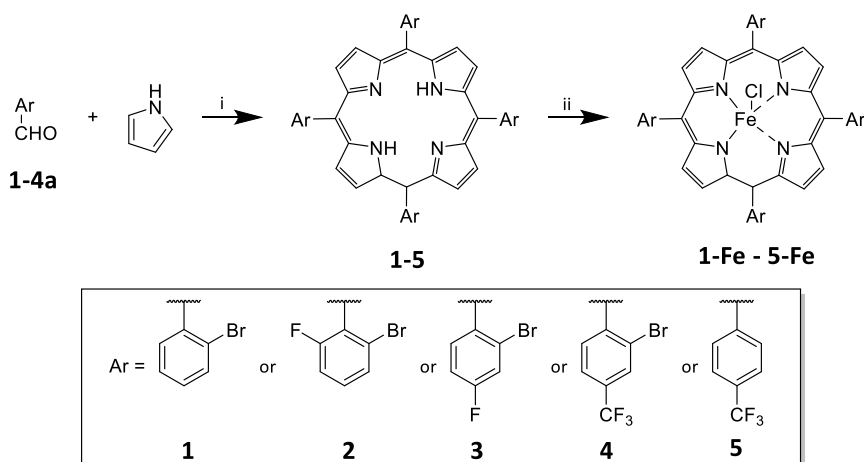
Scheme 8: synthesis of porphyrins bearing bromine as XB donor
i) 1. BF3(EtO)₂, DCM, 1h; 2. DDQ, 3h; 3. TEA, overnight. ii) FeCl₂, DMF, 120°C, MW, HCl

To synthesize the five porphyrins, we combined the respective aldehydes (1-4a) with an equal quantity of pyrrole under acidic environment. For all porphyrins except porphyrin **2-Fe**, we employed $BF_3(OEt)_2$ as the acid catalyst obtaining the desired compounds in satisfactory yields (12-40%). The case of porphyrin **2-Fe** requires special mention, because we encountered significant steric hindrance issues stemming from the presence of two *ortho* substituents on the benzyl-aldehyde, potentially obstructing the macrocycle formation. To overcome this obstacle, we turned to a different acid, In(OTf)₃, known for its effectiveness in cases of sterically hindered cyclization.[124] This modification

allowed us to successfully obtain macrocycle 2 with an acceptable yield of 4%. Porphyrin 5 is commercially available as free base and was bought at Porphychem®. Once obtained, the free-base porphyrin was metalated using $FeBr_2$ through the already described microwave-assisted procedure, which allowed to obtain the Fe(III) porphyrins **1-Fe – 5-Fe** in almost quantitative yields.

3.3.2 Cyclic Voltammetry in Solution Under Argon and CO_2 Atmosphere

We conducted the analysis of the electrochemical characteristics of porphyrins **1-Fe – 5-Fe** by cyclic voltammetry (CV), at first, in an argon atmosphere. This analysis was performed in a solution containing 0.1 *M* of $TBAPF_6$ in dry DMF. We employed a glassy carbon working electrode, a Pt-counter electrode, and a Saturated Calomel Electrode (SCE) as the reference electrode, maintaining a constant temperature of 293 *K*. It's worth noting that porphyrin **2-Fe** is excluded from this discussion since the cleavage of the four bromine substituents from the phenyl rings occurs before the generation of the active Fe(0) species, as anticipated above. *Figure 35* provide an overview of the electrochemical behaviour of porphyrins **1-Fe**, **3-Fe**, **4-Fe**, and **5-Fe**, in comparison to 5,10,15,20-Tetraphenyl-21H,23H-porphine iron(III) chloride (**FeTPP**), which serves as our reference compound). *Table 10* provides a summary of the reduction potentials.
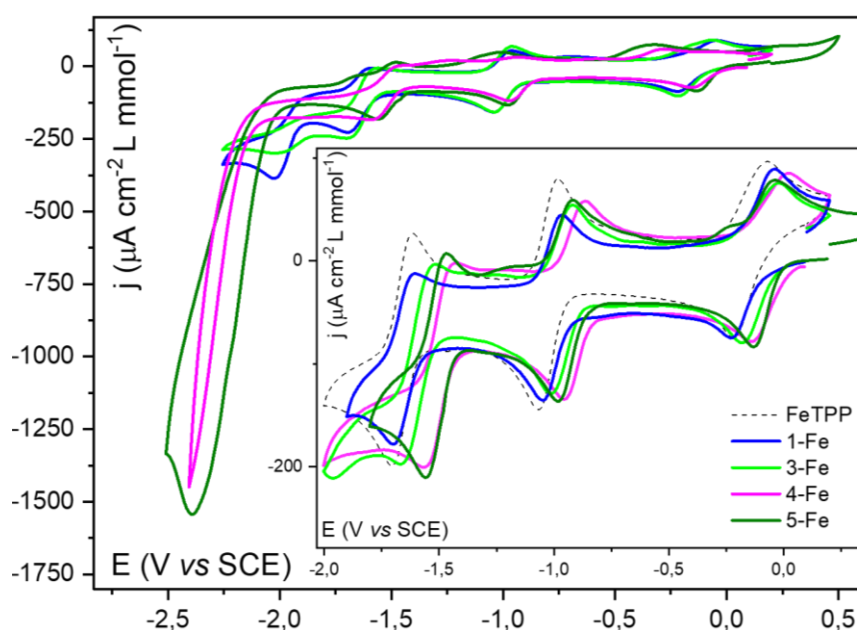
Figure 35: *CVs under argon in 0.1 M TBAPF₆/DMF for various Fe porphyrins with a focus on the region between 0.4 and -2 V vs SCE*

Table 10: *synopsis of redox potential E°' for the three reduction wave of Fe(III) to Fe(0), E^p_{red1} (cleavage of C-Br bond) and E^p_{re2} (irreversible reduction of CF_3)*

	E°'$_1$ Fe(III)/Fe(II) (V *VS* SCE)	E°'$_2$ Fe(II)/Fe(I) (V *vs* SCE)	E°'$_3$ Fe(I)/Fe(0) (V *vs* SCE)	E$^P_{RED1}$ (V *vs* SCE)	E$^P_{RED2}$ (V *vs* SCE)
FeTPP	- 0.15	- 1.02	-1.66	-	-
1-Fe	- 0.13	- 0.99	- 1.64	- 2.02	-
3-Fe	- 0.13	- 0.99	-1.63	- 2.02	-
4-Fe	- 0.07	- 0.91	-1.50	-	-2.40
5-Fe	-0.09	-0.94	-1.51	-	-2.39

Figure 35 reveals that, for all the examined porphyrins, three distinct cathodic waves appear within the potential range of 0.4 to -2 *V vs* the standard calomel electrode (SCE). These waves can be readily attributed to the three successive reduction steps that convert Fe(III) into Fe(0). As the potential is further lowered beyond -2.0 *V vs* SCE, porphyrins **1-Fe** and **3-Fe** exhibit an additional wave at approximately -2.1 *V vs* SCE, which can be attributed to the cleavage of the four bromine atoms located in the *ortho* position of the phenyl rings. In the case of porphyrins **4-Fe** and **5-Fe**, a significant wave is also observed around -2.4 *V vs* SCE. This wave has been associated with the reductive cleavage of CF_3.[125] Distinctively, the cleavage of the C-Br bond does not seem to occur for porphyrin **4-Fe**. *Table 10* also highlights the influence of electron-withdrawing substituents, as expected, on the shifting of all the reduction peaks towards more positive potentials. Remarkably, the more electron-withdrawing the substituent (in the order of H < F < CF_3), the more positively the reduction potentials are displaced. This effect is most pronounced in the case of **4-Fe**, bearing the CF_3 moiety, where the reduction potentials become the most positive within the series. After characterizing the iron porphyrins under an inert atmosphere, we proceeded to investigate their responses in the presence of CO_2. For this purpose, we saturated the cell's atmosphere by introducing CO_2 through bubbling. *Figure 36* displays the resulting CV curves recorded under these conditions.
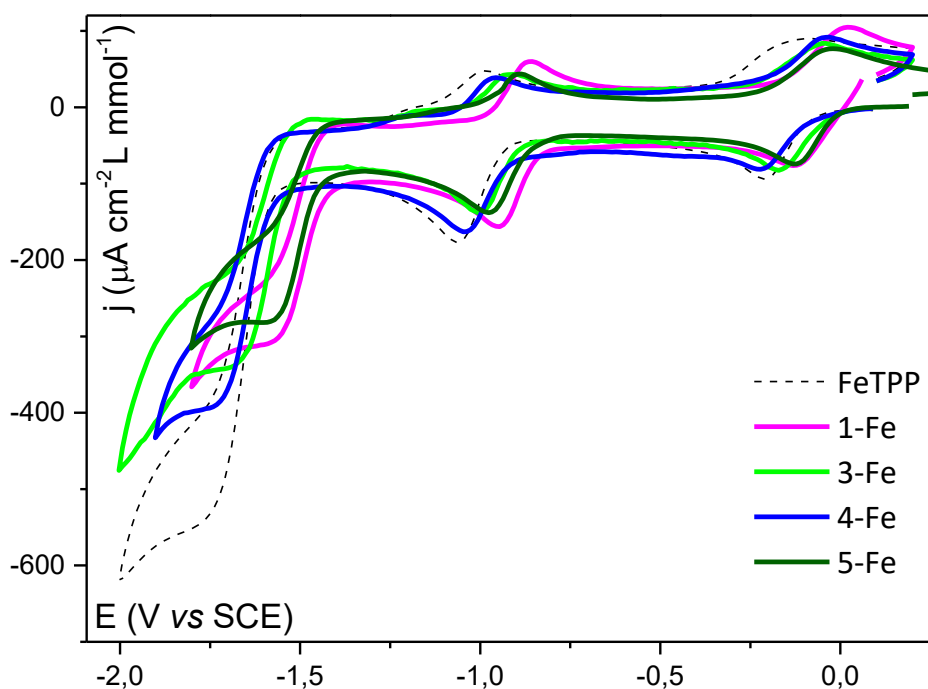
Figure 36: CVs under CO_2 in 0.1 M $TBAPF_6$/DMF for various Fe porphyrins

Upon examining the *figure*, it is evident that for the four porphyrins **1-Fe – 5-Fe** and for the reference **FeTPP** the two cathodic waves, corresponding to the Fe(III)/Fe(II) and Fe(II)/Fe(I) transitions, are still observable. Additionally, a substantial catalytic wave is observed during the Fe(I)/Fe(0) conversion. This phenomenon occurs because as soon as the Fe(0) species is generated, it engages with the CO_2 present in the cell, catalysing its reduction. This catalytic process results in a significant increase in current due to the movement of electrons from the electrode to the solution, leading to CO_2 reduction. The potential at which the catalytic wave is observed is closely linked to the presence and strength of electron-withdrawing groups. Notably, among the porphyrins studied, porphyrin **4-Fe** bearing a CF_3 moiety exhibits the most positive catalytic wave, followed by **3-Fe**, **1-Fe** (bearing F and H respectively), and, finally, FeTPP. It is intriguing to observe that Porphyrin **5-Fe** shows reduction potentials comparable to those of **4-Fe**, which can be explained by the presence of the same trifluoromethyl moiety in the *para* position of the phenyl substituent. However, the catalytic wave in the case of **5-Fe** is less intense. This observation may be a first suggestion of the positive influence of the halogen bonding donor plays a role in enhancing the catalytic process. It is noteworthy to observe that as the concentration of a weak acid like phenol (PhOH) is progressively raised in the solution, the catalytic wave exhibits a corresponding increase, (*figure 37*).
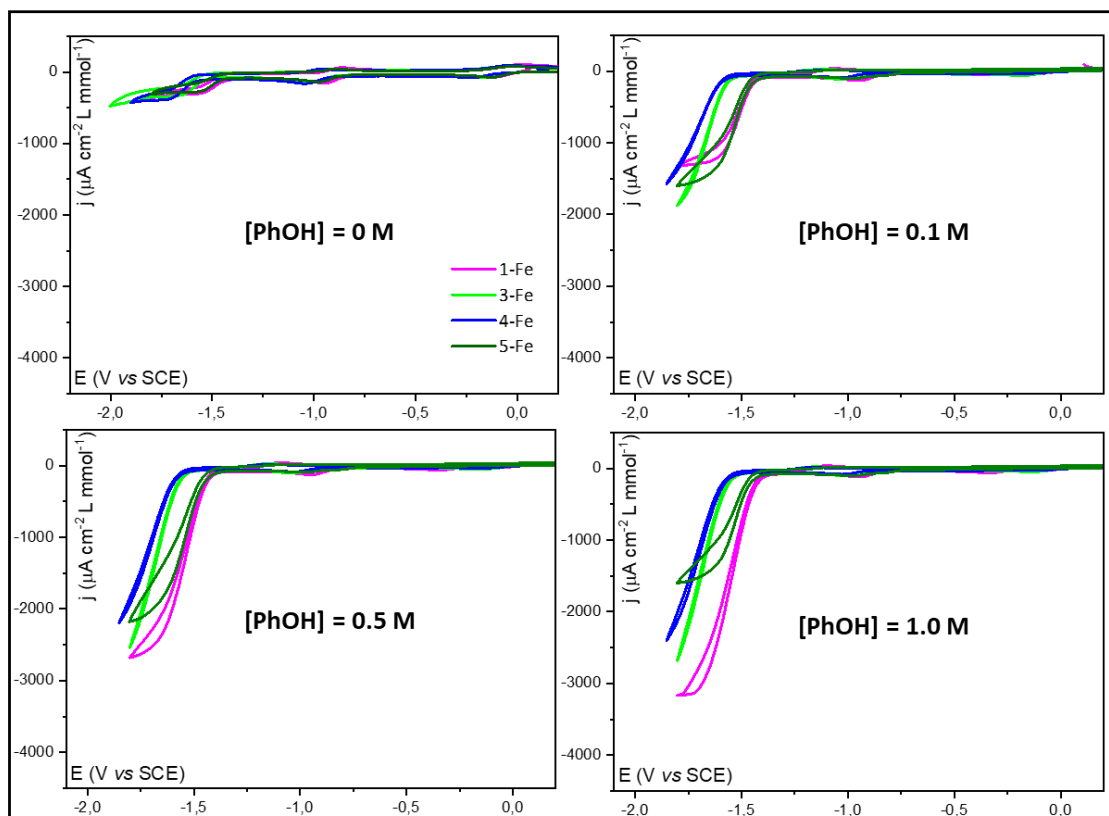
Figure 37: CVs under CO_2 in 0.1 M TBAPF$_6$/DMF for various Fe porphyrins, in presence of increased concentrations of phenol (PhOH)

This observed behaviour aligns with expectations, as the reduction of CO_2 to CO is an acid-catalyzed process. As the concentration of PhOH increases, the intensity of the catalytic wave likewise grows. This trend mirrors what has previously been noted for **FeTPP**.[126] In order to quantitatively assess the catalytic activity at various proton concentrations, we calculated the catalytic rate constant, denoted as "*k*", utilizing the "foot of the wave analysis" (FOWA) method. This method relies on extracting the parameters i^0_p (peak current) and E^0 (standard potential) from the cyclic voltammograms (CVs) and subsequently subjecting them to mathematical manipulation (see *section V* for details). The calculated *k,* that characterize the kinetic of the processes, of the considered porphyrins at different PhOH concentrations are reported in *table 11*.

Table 11: *catalytic rate constant k for different porphyrins, in presence of different amount of PhOH determined by FOWA*

CATALYST	k (M^{-1}s^{-1})			
	[PhOH] = 0 M	[PhOH] = 0.1 M	[PhOH] = 0.5 M	[PhOH] = 1.0 M
FeClTPP	20	$1.7\ 10^3$	$5.1\ 10^4$	$5.3\ 10^4$
1-Fe	7	$2.1\ 10^2$	$4.9\ 10^2$	$6.2\ 10^2$
3-Fe	13	$4.5\ 10^2$	$6.6\ 10^2$	$7.4\ 10^2$
4-Fe	15	$2.2\ 10^2$	$6.2\ 10^2$	$7.4\ 10^2$
5-Fe	9	$1.2\ 10^2$	$2.0\ 10^2$	$1.4\ 10^2$

3.3.3 Catalytic Tafel Plot and Evaluation of *Through-Structure* Effects

The Catalytic Tafel plot offers a systematic approach for exploring the *through-structure* electronic substituent effects of catalysts in catalytic reactions. This plot establishes a correlation between the turnover frequency (TOF, *equation 4*):

$$TOF = \frac{N_{product}}{N_{active\ cat}} \tag{4}$$

where $N_{product}$ is the number of moles of product generated per unit time, and N_{active_cat} is the maximal number of moles of active catalyst present in the reaction-diffusion layer only) and the potential (E) or overpotential (η). The overpotential (η) is calculated as shown in *equation 5:*

$$\eta = E^0_{CO2/CO,DMF} - E \tag{5}$$

Where E°$_{CO2/CO,DMF}$ is equal to -0.74 *V vs SHE-*. Prior research has indicated that effective catalysts tend to occupy the top-left region of the Catalytic Tafel plot.[127] *Figure 37* displays the Catalytic Tafel plot for our porphyrins and FeTPP.
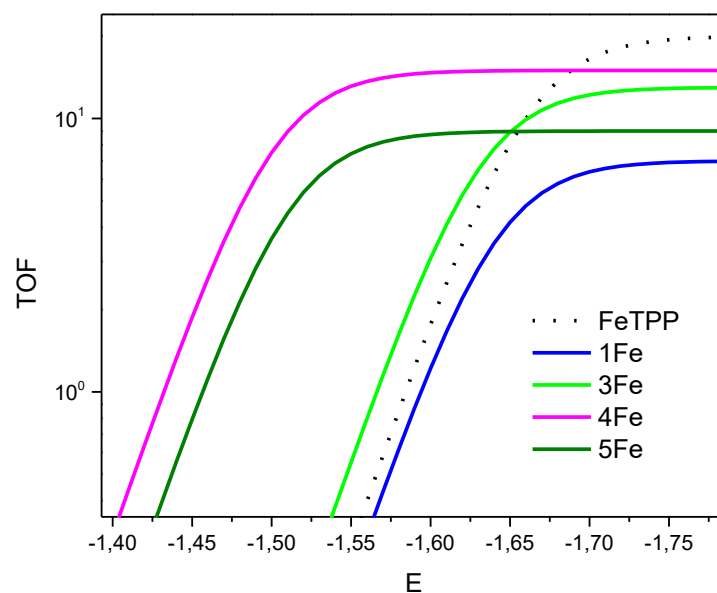
Figure 38: *Catalytic Tafel plots of the Fe-porphyrins for [PhOH] = 0 M.*

FeTPP (black line) clearly presents the higher TOF, but with unfavourable E.On the other hand, **4-Fe** and **5-Fe** (respctively the pink and dark gren lines) show lower E values. Moreover, among the two, **4-Fe** has also a higher TON, thus suggesting a possible role of halogen bonding on the catalytic activity. These results indicate a probable impact of Halogen Bond on CO_2-to-CO reduction through space. Importantly, the catalytic activity of the halogen-bond capable porphyrins increases with the strength of the σ-hole (see next section). From *figure* 38, it is also evident that significant electron-withdrawing character is needed to activate halogen-bonding at the formal Fe(0) state, due to possible attenuation by the overall negative charge of the metalated porphyrins (see also *figure 39b*). Indeed, **1-Fe** shows lower catalytic activity compared to **FeTPP** along all potentials, whereas both **2-Fe** and to a much higher extent **4-Fe** are capable of high turnover frequencies at potentials significantly positive of that of **FeTPP** (*figure 38*). On the other hand, **5-Fe**, bearing no XB donor, shows low E but also low TOF

3.3.4 DFT Calculations

The bromo-porphyrin derivatives' halogen bond donor capabilities may be assessed by determining the Electrostatic Surface Potential (ESP), with a particular focus on its intensity at the σ-*hole* location, as illustrated in *figure 39:*
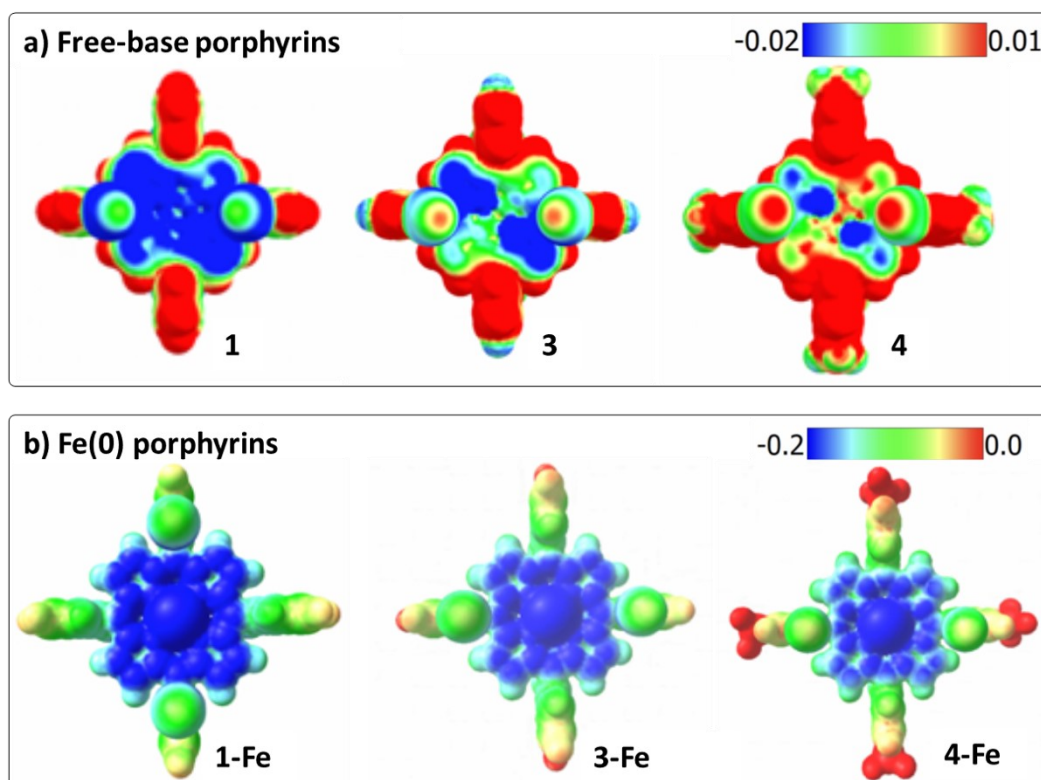
Figure 39: a) molecular electrostatic potential maps of the free-base and b) iron porphyrins at the formal Fe(0) oxidation state. Maps were plotted in Chemcraft with a scale of 1.5 (a) and 1.0 (b)

The calculations were performed by doctor N. Von Wolff, from *Laboratoire d'Electrochimie Moléculaire, Université Paris Cité*. Indeed, in the free-base porphyrins, the σ-*hole* increases from 1 to 3 and 4 in agreement with electron-withdrawing character of the substituents (H *vs* F *vs* CF$_3$), as proven by the increased intensity of colouring on bromine substituents (from green of 1 to intense red in 4). We were also interested to see if the σ-*hole* character persists upon metalation of the free-base and in particular upon reduction to the formal Fe(0) oxidation state (*figure 39b*). Although the overall σ-hole character seems attenuated by the global two-fold negative charge of the Fe(0)-porphyrins, a similar trend as for the free-base ligand is observed, i.e. with an increase of σ-hole character in the order of 1-Fe, 3-Fe and 4-Fe.

3.3.5 CPE (Controlled Potential Electrolysis)

The capability of porphyrins **1-Fe − 5-Fe** to generate CO in the presence of PhOH was evaluated through preparative-scale electrolysis experiments conducted under constant potential (CPE) conditions. Initially, only the oxidized species, CO$_2$, is present in the solution. Subsequently, the potential is adjusted to a constant value (-1.70 V *vs* SCE, in

our case), sufficiently negative to drive CO_2 reduction, and maintained at this level until only the reduced species remained in the solution. The selection of this potential was based on an analysis of the cyclic voltammograms (CVs), identifying a potential at the base of the catalytic wave. The total charge passed during the CPE experiment (denoted as Q) was determined by integrating the current, and is directly related to the number of electrons transferred per molecule (n) and the initial number of moles of the oxidized species (N) using Faraday's law (*equation 6*):

$$Q = nFN \tag{6}$$

Here, F represents Faraday's constant (96500 *C mol^{-1}*) and n is equal to 2. The Faradic efficiency (FE) is defined as the ratio of the experimentally detected amount of CO produced to the theoretically expected amount of CO, and it can be computed as follows:

$$FE = \frac{V_{CO}*n*F}{molar\ volume\ of\ CO*Charge} \tag{7}$$

The experimental determination of V_{CO}, representing the total quantity of CO generated during the CPE experiment, was accomplished by collecting gas samples from the headspace of the cell and subjecting them to analysis through gas chromatography. The experiments confirmed that the four porphyrins are selectively active for the catalytic reduction of CO_2 to CO at the Fe(I)/Fe(0) redox couple without forming H_2 or any other undesired side product (*table 12*):

Table 12: *calculated faradaic efficiencies for H_2 and CO after 1h electrolysis at $-$ 1.70 V vs SCE*

Catalyst	Fe H_2	Fe CO
1-Fe	0 %	92 %
3-Fe	0 %	87 %
4-Fe	0 %	83 %
5-Fe	0 %	99 %

The stability of the porphyrins during the experiment was tested recording a CV before and after the one-hour electrolysis. No major changes seem to occur, but a small degradation of the porphyrins may explain FE lower than 100%.

3.4| CONCLUSIONS

To conclude, in partnership with Université Paris Cité, we successfully developed the synthesis of four porphyrins featuring bromine atoms as halogen-bonding donor groups. Our primary goal was to explore whether halogen bonding could act as a *through-space* interaction to enhance the catalytic conversion of CO_2 to CO, mediated by iron porphyrins. To comprehensively understand the behaviour of these compounds in the CO2RR to CO, we conducted thorough electrochemical characizations using cyclic voltammetry under Ar and CO_2, as well as controlled potential electrolysis. These experiments allowed us to gather kinetic information on the reaction and determine Tafel plots, essential tools for evaluating catalytic properties. Theoretical DFT calculations served as a valuable tool, reinforcing our experimental findings. We successfully demonstrated that halogen bonding (XB) might indeed play a pivotal role in catalysis, particularly when the molecule hosts electron-withdrawing groups that enhance the s-*hole* on bromide. Notably, a significant electron-withdrawing character is crucial for activating halogen bonding at the formal Fe(0) state. Porphyrins **4-Fe** exhibited high turnover frequencies at potentials significantly positive compared to those of **FeTPP**. Furthermore, it is worth highlighting that all four porphyrins exhibited selective activity for the catalytic reduction of CO_2 to CO at the Fe(I)/Fe(0) redox couple without generating H_2 The discoveries outlined in this section have been condensed into a manuscript, which currently in preparation for the submission.

SECTION IV

PORPHYRINS FOR NLO

4.1| Nonlinear Optics (NLO)

4.1.1 General Concepts

The term Nonlinear Optics (NLO) describes optical phenomena that arise when a powerful, oscillating electromagnetic field (for instance, the one generated by an intense and coherent laser light) interacts with molecules or bulk materials, resulting in the emission of new electromagnetic fields. These new fields differ from the incident light in terms of frequency, phases, or other optical characteristics. When a laser beam interacts with a molecule, the perturbation (the total polarization) is expressed by *equation 8*:

$$\vec{P} = \mu_0 + \alpha\vec{E} + \beta\overrightarrow{E^2} + \gamma\overrightarrow{E^3} + \cdots \tag{8}$$

Being μ_0 the molecular ground state electric dipole moment, α the linear polarizability tensor, while β and γ are the quadratic and the cubic hyperpolarizability respectively. The terms $\beta\overrightarrow{E^2}$ and $\gamma\overrightarrow{E^3}$ correspond to the generation of light with double (2ω) or triple (3ω) frequency than the incident one through a nonlinear polarization process. Usually, higher order phenomena can be neglected.[10] It is important to underline that β vanishes in a centrosymmetric environment. Therefore, to have a second-order NLO effect, the acentricity requirement must be fulfilled. This is not true for γ.[128] Different techniques are available for the measurement of the second-order NLO response of molecular species, such as Rayleigh scattering (HRS)[129], Stark effect[130], solvatochromism[131,132] and EFISH (Electric Field Induced Second Harmonic generation).[133–136]

4.1.2 EFISH Technique

In the characterization of the second-order NLO response of chromophores with evident push-pull structures, as for example, asymmetric porphyrins, the EFISH technique is particularly used. This technique allows the determination of the quadratic hyperpolarizability β (which represents the figure of merit of the second order NLO response) through *equation 9*:

$$\gamma_{EFISH} = \frac{\mu_0\beta_\lambda(-2\omega;\ \omega,\omega)}{5kT} + \gamma(-2\omega;\ \omega,\omega,0) \tag{9}$$

γ_{EFISH} is the sum of a cubic electronic contribution $\gamma(-2\omega; \omega, \omega, 0)$ and of a quadratic dipolar contribution $\mu_0\beta_\lambda(-2\omega; \omega, \omega)/5kT$, being μ_0 is the ground-state molecular dipole moment and β_λ the projection along the dipole moment axis, of the vectorial component β_{vec} of the tensorial quadratic hyperpolarizability working with an incident wavelength λ. In order to avoid overestimation of the quadratic hyperpolarizabilty due to resonance enhancements, it is necessary to choose an incident wavelength whose second harmonic is far from any electronic absorption of the molecule. The third order contribution to γ_{EFISH} $\gamma(-2\omega; \omega, \omega, 0)$ is usually negligible compared with the dipolar orientation for the molecules usually investigated by the EFISH technique.[137,138]

In a typical EFISH experiment, the molecule of interest is dissolved in an appropriate solvent and put into an optical cell. Electrodes on opposite sides of the cell provide the means for applying a high voltage DC electric field, which orients the molecular dipoles and breaks the macroscopic centrosymmetry of the solution. Then the cell is shone with a laser light at ω frequency. Under these conditions, the second harmonic response of the solution at frequency 2ω resulting from interaction with the strong optical field of the laser light can be observed.[139]

4.1.3 Materials with NLO Proprieties

To obtain molecules displaying significant second order NLO effects, high values of β are required. In 1977 Oudar gave a theoretical interpretation of the electronic factors controlling β.[140] The quadratic hyperpolarizability of a molecule is originated by the mobility of polarizable electrons under the effect of the strong electric field $\vec{E}$ associated with an incident radiation. Therefore, it depends on electronic transitions which, being associated with a significant electronic mobility, are characterized by a high charge transfer (CT) character. Second order NLO properties are present across various classes of chemical compounds, spanning from inorganic crystals[141] to organic[142] and organometallic molecules.[128] Within organic molecules, there are two primary families of NLO chromophores: dipolar and octupolar species. Dipolar species, lacking centrosymmetry, exhibit an asymmetrical charge distribution, often achieved through the introduction of donor and/or acceptor group substituents. This creates a donor–π–conjugated bridge-acceptor (D–π–A) network, as seen in examples like *p*-nitroaniline *(figure 40)*.
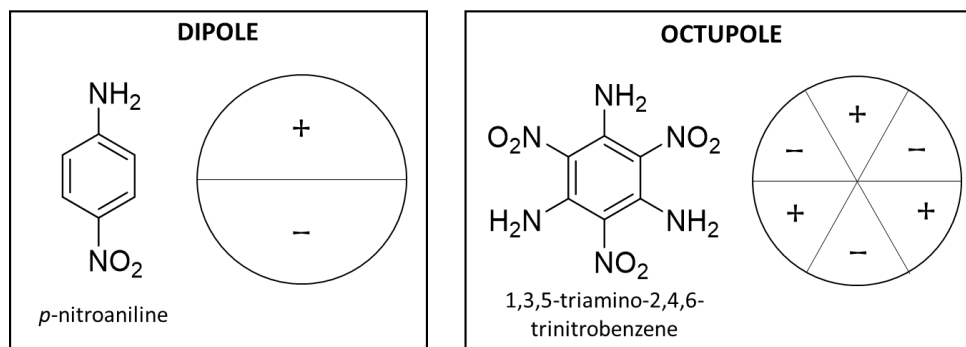
Figure 40: *Dipole and octupole in second order NLO-molecular based materials*

On the other hand, octupolar molecules may possess centrosymmetry but involve twofold (D_2) or threefold (D_3) rotational axes. These molecules are characterized by multidirectional charge transfer (CT) excitations, as exemplified by 1,3,5-triamino-2,4,6-trinitrobenzene *(figure 40)*. The theoretical description of nonlinearity in such systems necessitates a three-level approach, even in its simplest form. In the past decade, second order NLO active coordination and organometallic complexes have gained prominence in the realm of molecular NLO chromophores. This is attributed to the unique structural and electronic characteristics arising from the interaction of a metal centre with organic ligands. In contrast to organic molecules, coordination and organometallic complexes offer a broader range of electronic structures, influenced by factors such as the metal's electronic configuration, oxidation state, and coordination sphere. Particularly noteworthy is the role of the metal centre in dipolar NLO chromophores, where it can serve as the donor, acceptor, or even the bridge within a donor–acceptor network.

4.2| DESIGN OF HYBRID MATERIALS

In the frame of organic and organometallic molecules, porphyrins and their metal complexes have been widely studied from NLO point of view thanks to their thermal and chemical stability together with the possibility of a precise structure tailoring. Thus, a proper tuning of the optical and the electronic features of such chromophores may enhance their second order NLO response. To obtain intriguing conjugates, porphyrins can be linked to various carbonaceous organic components like fullerene, nanotubes, carbon spheres, and graphene. [143–146] A recent work[147] in collaboration with Professor Tagliatesta from the University of Rome "Tor Vergata" delved into the second-order nonlinear optical (NLO) response of Zn(II)porphyrins dyads and triads. These structures incorporated electron-donor ferrocene (Fc) and/or electron-acceptor fullerene (C60) connected by an ethynylphenyl spacer to the porphyrins, and their NLO properties were assessed using the EFISH technique. The investigation confirmed the porphyrins' versatility by acting as either electron acceptors or donors, depending on their connection to the electron-rich Fc or electron-deficient C60. Strikingly, all compounds examined exhibited a remarkably negative EFISH response. This evidence, in addition to the almost negligible dipole moment (μ) calculated via DFT, suggested a noteworthy third-order contribution to their second order NLO response. In completion of the previous work, we decided then to investigate novel hybrids involving Zn porphyrins and two-dimensional graphene nanoplates (GNP) with or without a Fc moiety, as illustrated in *figure 41*.
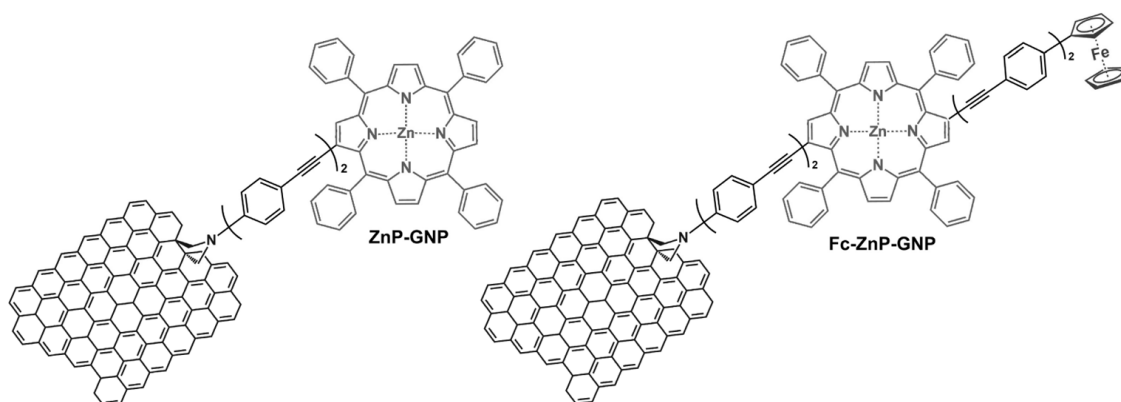
Figure 41: *Zn(II) porphyrins dyads and triads investigated in this Section*

GNP can be described as few layers of graphene. His functionalization with organic molecules permits to overcome its poor solubility due to the high π-π interlayer attraction energies. The π-delocalized electron system can serve as an electron acceptor when coupled with a metal porphyrin, establishing a *push-pull* system. In this instance the spacer of the dyad/triad consists of two ethylnylphenyl moieties instead of one. The increased length of the spacer is expected to yield a higher response compared to the system studied earlier, potentially resulting in the development of new promising materials with enhanced nonlinearity. After their synthesis and characterization from the Tor Vergata group, the two hybrids **ZnP-GNP** and **Fc-ZnP-GNP** were then investigated at the University of Milano's Chemistry Department using the EFISH technique in dichloromethane solution with a 1907 nm wavelength. The experimental data, compared with the theoretical DFT calculations DFT gave us a deep view of the second order NLO-proprieties of the two hybrids.

4.3| RESULTS AND DISCUSSION

4.3.1 Synthesis

The synthetic route that leads to the two hybrids compounds **ZnP-GNP** and **Fc-ZnP-GNP** is summarized in *scheme 9.*
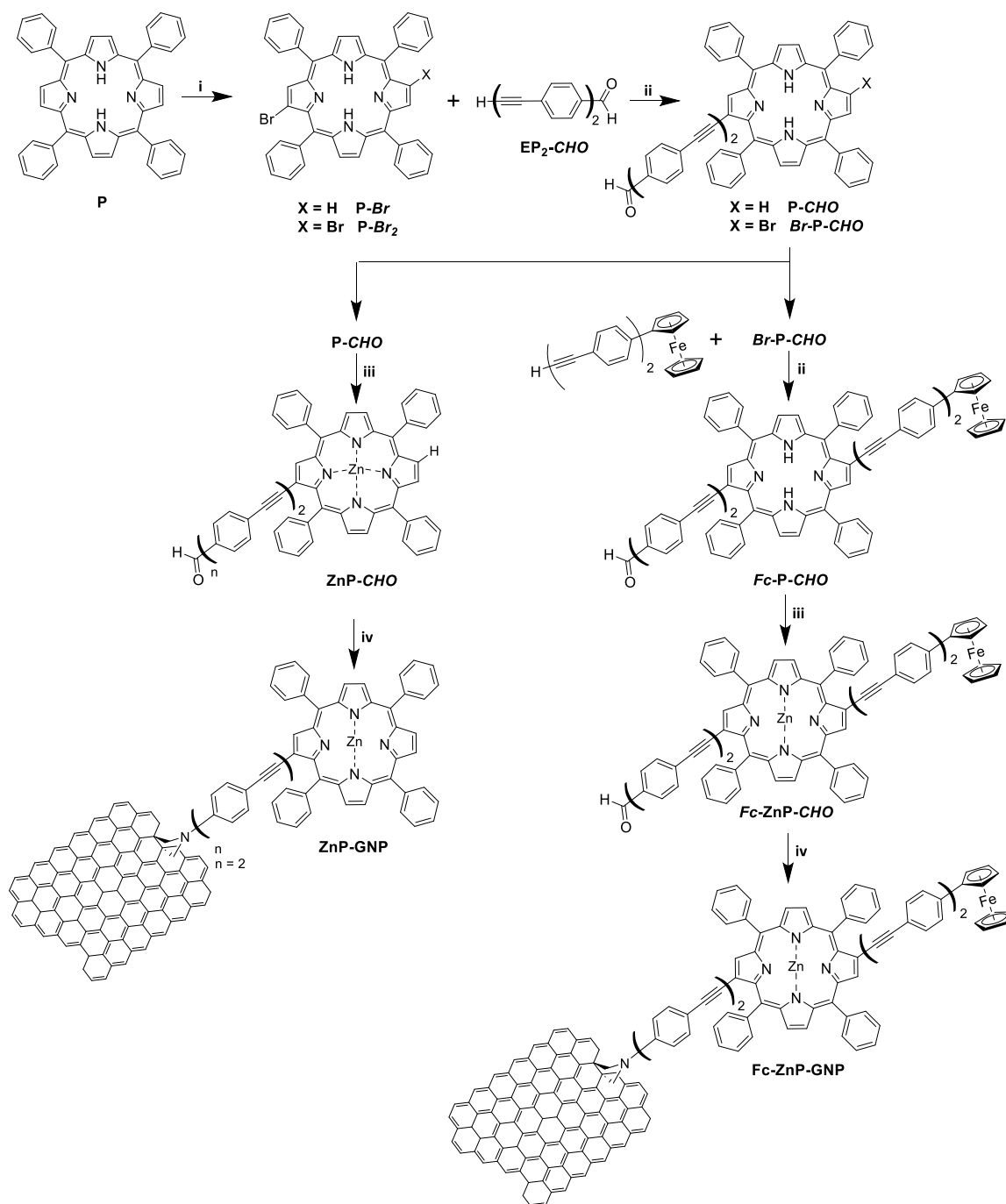
Scheme 9: *Synthetic route to the investigated compounds*
*i) NBS, hv (200 W), CH$_1$Cl$_2$; ii) Pd$_2$(dba)$_3$/AsPh$_3$, toluene/NEt$_3$ = 5/1, N$_2$, 40°C, 16h iii) Zn(OAc)$_2$·2H$_2$O, CHCl$_3$/CH$_3$OH, reflux, 1h; iv) **GNP**, N-methylglycine, toluene, N$_2$, Δ, 72h*

For both compounds the synthesis starts with the bromination of the commercially available free base TPP with NBS in different stochiometric ratio in order to obtain the monobromo P-*Br* or dibromo P-*Br$_2$* derivative. The regiospecific antipodal bromination in 2,12 β-*pyrrolic* position is carried out using a light induced reaction in dichloromethane.[62] The Sonogashira's coupling of P-*Br* and P-Br$_2$ with 1.5 *eq.* of 4-[(4'-ethynyl)phenyl]-ethynylbenzaldehyde (EP$_2$-*CHO*) afforded derivatives P-*CHO* and *Br*-P-*CHO* in 65 and 36% yield, respectively, after chromatographic purification. P-*CHO* was then metalated dissolving the free-base in chloroform and adding a 10% excess of a Zn(OAc)$_2$ methanol solution, to afford the corresponding complex ZnP-*CHO*. Finally, the electron acceptor unit GNP was connected to ZnP-*CHO* by the Prato–Maggini reaction,[148] leading to dyad **ZnP-GNP**. On the other hand, the preparation of triad **Fc-ZnP-GNP** involved, before complexation of the core with Zn(II) and the Prato–Maggini reaction, a second Sonogashira coupling between Br-P-CHO and two equivalents of EP$_2$-*Fc*, obtaining intermediate *Fc*-P-*CHO* in 53% yield. The synthesis of graphene nanoplatelets (GNP), inserted via Prato-Maggini reaction, was carried out using a method developed by some of us,[148] employing a standard 800 *W* household microwave (MW) oven. The process begins with an Asbury Expandable graphite sample (Asbury Carbons, Detroit, MI, USA), in which the graphene planes were intercalated with chemical substances such as sulphates and nitrates. Following MW irradiation, the resulting samples exhibit a worm-like morphology with a significantly large particle area. A brief ultrasound treatment in isopropyl alcohol is then applied to eliminate the overall worm-like structures from the GNPs. Post-treatment, the 2D particles exhibit a lateral dimension of 10 μm and thicknesses < 5 *nm*, corresponding to several layers of graphene.

4.3.2 SEM of GNP

The prepared GNP was characterized by SEM analysis, as shown in *figure 42:*
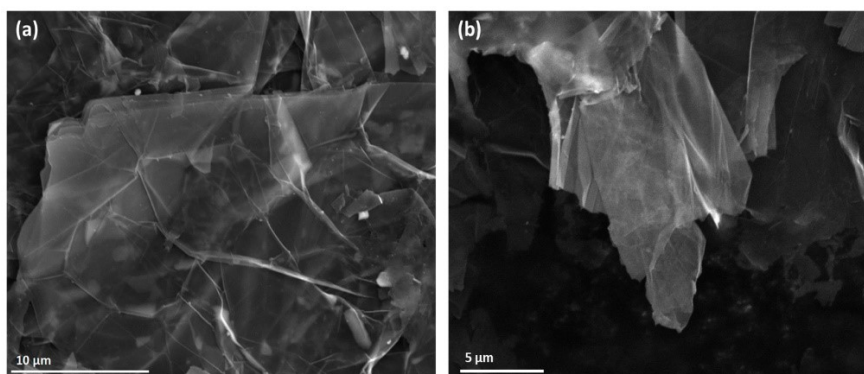
Figure 42*: SEM micrographs at different magnifications: (**a**) 10 μm and (**b**) 5 μm*

The pictures depict micrographs of GNP samples acquired post-irradiation with a conventional 800 *W* household microwave oven. SEM micrographs reveal the pristine GNP's smooth surface, validating the expansion of intercalated multilayer graphite and showcasing a well-dispersed material. The 2D particles exhibit a lateral dimension of approximately 10 *μm*, indicative of several layers of graphene (3–7 layers).[149]

4.3.3 UV-Vis Spectroscopy in Solution

Dyad **ZnP-GNP** and triad **Fc-ZnP-GNP** were examined using UV–Vis spectroscopy in a CH_2Cl_2 solution (the same solvent employed in the EFISH experiments) to exclude any resonance effects on the second-order nonlinear optical (NLO) properties. *Figure 43* presents the spectra in their original form, alongside the spectrum of the precursor compound *Fc*-ZnP-*CHO* (*scheme 9*). A summary of the UV–Vis data for the studied and reference compounds is detailed in *table 12*.
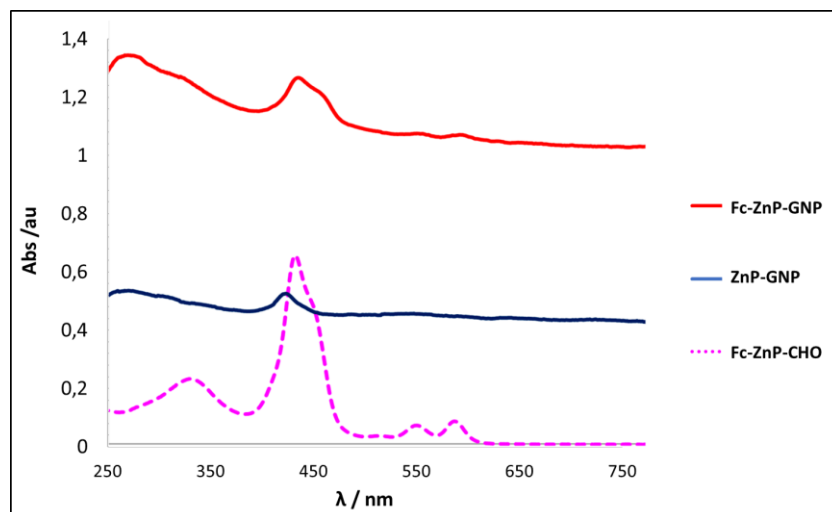
Figure 43: *UV-Vis spectra in CH$_2$Cl$_2$ of the investigated compound and of precursor Fc-ZnP-CHO*

Table 12: *synopsis of UV-Vis spectra in CH$_2$Cl$_2$ of the investigated compound and of precursor Fc-ZnP-CHO*
*ZnP data are from Materials (2021), 14(16), 4404 [146]

ENTRY	Λ_B/NM	Λ_{QA}/NM	Λ_{QB}/NM
ZNP-GNP	433	nd	nd
FC-ZNP-GNP	445	567	611
FC-ZNP-CHO	442	567	605
ZNP*	420	548	589

Looking at *figure 43*, the UV–Vis spectra of **ZnP-GNP** and **Fc-ZnP-GNP** exhibit a predominant optical density in the near-IR region, primarily attributed to the plasmonic resonance of GNP.[148] This dominance hinders the clear observation of the typical pattern associated with porphyrin metal complexes. Conversely, the spectrum of the precursor compound *Fc*-ZnP-*CHO*, which lacks the GNP unit, displays classical spectroscopic features anticipated for a metal porphyrin, following Gouterman's "four orbital" model,[4] with a sharp and intense ($\varepsilon \approx 105$ M^{-1} cm^{-1}) Soret or B band at 400–450 *nm*, corresponding to an S$_0 \rightarrow$ S$_2$ transition, and two less intense ($\varepsilon \approx 104$ M^{-1} cm^{-}) Q bands at 550–650 *nm*, attributed to S$_0 \rightarrow$ S$_1$ transitions. In the case of **ZnP-GNP**, only the Soret band is evident, while the Q bands are obscured in the background, making it challenging to reliably determine their wavelengths. In contrast, for **Fc-ZnP-GNP**, both the B band and the two Q bands are discernible, and the B band presents a shoulder at higher

wavelengths. This feature is attributed to the Fc unit, and it agrees with the presence of the same shoulder in the spectrum of *Fc-ZnP-CHO*. The formation of covalent bonds between ZnP and GNP at the 2 β-*pyrrolic* position, facilitated by two ethynylphenyl spacers, induces a 13 nm bathochromic shift in the Soret band (from 420 *nm* to 433 *nm*). This shift underscores the electron-withdrawing nature of the carbonaceous unit. Introducing an Fc moiety in the 12 β-*pyrrolic* antipodal position, as seen in **Fc-ZnP-GNP**, results in an additional 12 nm red-shift compared to **ZnP-GNP** (from 433 *nm* to 445 *nm*). To summarizes, the interaction with GNP not only perturbs the electronic state of ZnP, but also intensifies when an electron donor moiety is present in the antipodal position of the core. This suggests heightened π-delocalization within the system and a more pronounced *push–pull* character. Notably, the functionalization of the electron-rich β-*pyrrolic* position with donor substituents has been previously reported as an effective way of enhancing the second-order NLO properties of porphyrins.[150] The influence of GNP on the electronic properties of the studied hybrids is further evidenced by the 3 and 6 nm redshift experienced by the B and Q_a bands when moving from Fc-ZnP-CHO to **Fc-ZnP-GNP.**

4.3.4 EFISH and DFT Investigation of the Second Order NLO Properties

We explored the second order NLO properties of **ZnP-GNP** and **Fc-ZnP-GNP** through both experimental EFISH techniques and theoretical calculations using DFT. To underscore the influence of GNP, our investigation also included *Fc-ZnP-CHO*. *Table 13* summarized the experimental and theoretical findings.

Table 13: synopsis of experimental EFISH and theoretical DFT results on the investigated compound in comparison to the reference ones. *Data from Materials (2021), 14(16), 4404 [146]

Entry	μ (d)	Y_{efish} (x10^{-36} esu)	$\mu\beta_{1907}$ (x10^{-48} esu) (β_{190} x10^{-30} esu)	$\beta_{\|\|}$ (x10^{-30} esu)	$\mu\beta_{\|\|}$/5kt (x10^{-36} esu)	$Y_{\|\|}$ (x10^{-36} esu)	dipolar *vs cubic contr.* %
ZnP-GNP	1.23	-3160	-650 $(-528)^2$	20	120	-1890	6.3
Fc-ZnP-GNP	1.17	-8800	-1880 $(-1607)^2$	9	75	-4388	1.7
Fc- ZnP-CHO	5.31	-4130	-850 $(-160)^2$	94	2920	-5484	53
6(Zn)-C60*	4.77	-3470	-720 $(-151)^2$	30	696	-1543	45
10b(Zn)-C60*	4.14	-6410	-1330 $(-321)^2$	42	845	-3225	26

The experimental values of γ_{EFISH} and $\mu\beta_{1907}$ for the GNP-containing hybrids are comparable to those observed in a previous study where C60 was used as electron-acceptor, specifically 6(Zn)-C60 and 10b(Zn)-C60 in *table 13*.[146] A negative sign in the second-order NLO response measured by the EFISH technique may arise from intermolecular interactions or aggregation phenomena in solution.[151,152] However, for ZnP-GNP and Fc-ZnP-GNP, such influences can be confidently excluded due to the substantial steric hindrance characteristic of A$_4$ β-*pyrrolic* mono- or disubstituted Zn(II) porphyrins.[152] Moreover, the dihedral angles between the aryl rings in the four *meso* positions of the core and the mean plane of the macrocycle fall within the range of 70°–90°, resulting in an overall reduction of molecular flatness. In the case of the previously examined hybrids involving C60 instead of GNP, the negative sign of γ_{EFISH} was attributed to a non-negligible contribution from the electronic third-order cubic term $\gamma_0(-2\omega; \omega, \omega, 0)$ to the second-order nonlinear optical (NLO) response,[146] as indicated in *equation (9).* This observation aligns with other previous studies on β-*pyrrolic* mono- and di-substituted Zn(II) porphyrins,[149] where compounds with low polarity exhibited a diminished significance of the dipolar orientational contribution $\mu\beta_{1907}(-2\omega; \omega, \omega)/5\,\mathrm{kT}$ to γ_{EFISH}, overshadowed by $\gamma_0(-2\omega; \omega, \omega, 0)$. In contrast,

in classical push–pull NLO-phores, the latter term can be safely ignored.[153] Our recent findings on GNP-containing conjugates further reinforce and align with these previously established observations. Certainly, the experimental γ_{EFISH} and calculated $\gamma_{\parallel}$ values are closely comparable, at least in terms of magnitude, affirming the significance of third-order contributions to the second-order nonlinear optical (NLO) response. Additionally, the computed ground state dipole moments (μ) for **ZnP-GNP** and **Fc-ZnP-GNP** are notably low: 4 and 3.5 times lower, respectively, than the reference compounds 6(Zn)-C60 and 10b(Zn)-C60. They are also lower than those observed for other β-*pyrrolic* Zn(II) porphyrins previously studied.[149] From an NLO perspective, it can be inferred that GNP acts as a weaker electron acceptor compared to C60. Despite the red-shifts observed in the spectroscopic analysis, the dipolar *push–pull* character of GNP-containing systems diminishes in comparison to their C60-containing counterparts. Correspondingly, the calculated $\beta_{\parallel}$ values for GNP-containing compounds are 1.5 to 4.7 times lower than those of the corresponding C60-substituted complexes. However, caution is warranted when interpreting experimental β_{1907} values, as they are derived from *equation 9* under the assumption of neglecting $\gamma_0(-2\omega;\ \omega, \omega, 0)$, which, in reality, is crucial. The influence of GNP in diminishing the dipolar character of the examined compounds is supported by the substantial 5.31 D value of μ obtained for *Fc*-ZnP-*CHO*, which lacks the GNP unit. This value is also higher than those observed for C60-containing systems, consequently resulting in an elevated $\beta_{\parallel}$ value. However, even *Fc*-ZnP-*CHO* exhibits a negative γ_{EFISH} value. To offer a qualitative understanding of the relationship between the theoretical dipolar and cubic components of the second order NLO response in the investigated compounds, we computed the ratio between $\mu\beta_{\parallel}/5\ kT$ and $\gamma_{\parallel}$ (*table 13*, last column). For **ZnP-GNP** and **Fc-ZnP-GNP**, this ratio notably decreases to less than 10%, emphasizing the dominant role of $\gamma_0(-2\omega;\ \omega, \omega, 0)$ in γ_{EFISH}. In contrast, the corresponding C60-containing hybrids and *Fc*-ZnP-*CHO* exhibit higher ratios, aligning with their elevated μ and $\beta_{\parallel}$ values. In summary, our comprehensive EFISH and theoretical investigations indicate that the extended π-delocalized structure of GNP enhances the overall polarizability of GNP-containing hybrids without intensifying their *push–pull* character. Consequently, these

chromophores exhibit a noteworthy and substantial third-order contribution to the second order NLO response.

4.4| CONCLUSIONS

In this section, we employed a combined experimental EFISH and theoretical DFT approach to examine the second-order nonlinear optical (NLO) properties of two hybrids composed of Zn(II) *meso*-tetraphenyl porphyrin (ZnP), the electron acceptor graphene nanoplates (GNP), and the electron donor ferrocene (Fc). The UV–Vis absorption spectra indicated that incorporating a GNP unit in the 2 β-*pyrrolic* position of ZnP affects the electronic properties of the porphyrin core, akin to the perturbation induced by C60. Additionally, the presence of an Fc moiety in the antipodal position of the macrocycle proved crucial in enhancing the *push–pull* character of the system, distinct from the effect of inserting a second ethynylphenyl spacer. EFISH measurements for the newly formed GNP-conjugates revealed negative γ_{EFISH} and $\mu\beta_{1907}$ values comparable to those of C60-containing compounds. Notably, DFT computations indicated a very low ground state dipole moment (μ) for GNP-hybrids, even lower than those observed for corresponding C60-containing compounds, indicating that GNP has a less electron acceptor character than C60. The impact of GNP on lowering the μ value was further supported by the fair μ of *Fc*-ZnP-*CHO*, aligning with its higher ratio between the computed dipolar and cubic contributions (53% vs. less than 10%). Despite the negative second-order NLO response observed in all investigated compounds, including *Fc*-ZnP-*CHO*, it is evident that γ_{EFISH} is predominantly governed by the negative pure electronic term $\gamma_0(-2\omega; \omega, \omega, 0)$, which surpasses the dipolar orientational term $\mu\beta_{1907}(-2\omega; \omega, \omega)/5\,kT$. The extended π-delocalized structure of GNP proves highly effective in increasing the overall polarizability of the hybrids without proportionately intensifying their *push–pull* character. Consequently, these compounds primarily exhibit third order chromophoric behaviour. The discoveries outlined in this section have been condensed into a manuscript, entitled "Nonlinear Optical Properties of Zn(II) Porphyrin, Graphene Nanoplates, and Ferrocene Hybrid Materials" published on *Materials* in 2023.[154]

SECTION V

EXPERIMENTAL SECTION

5.1| GENERAL REMARKS

5.1.1 Materials and Methods

All reagents and solvents for the porphyrin's synthesis were purchased from PorphyChem, Merck and Fluorochem and they were used as received, except NEt_3 (freshly distilled over KOH), THF and Toluene (freshly distilled from Na/benzophenone under nitrogen atmosphere). $LiClO_4 \geq 99\%$ was bought from Acros organics. SnO_2 colloidal solution (15% in water), 0.180 mm thick Nafion-117 membrane, lithium Bis(trifluorometano)sulfonimide (LiTFSI), and ACS grade benzyl alcohol > 99% were purchased from Alfa Aesar. TiO_2 colloidal paste (Ti-nanoxide SP) from Solaronix.. TEC 8 Fluorine-doped Tin Oxide (FTO) conductive glass slides were obtained from Pilkington. Glassware was flame-dried under vacuum before use when necessary. Microwave assisted reactions were performed using the single-mode microwave synthesizer "Biotage's Personal Chemistry – Emrys Creator". Silica gel for gravimetric chromatography (Geduran Si 60, 63-200 μm) and for flash chromatography (Kieselgel 60, 0.040-0.063 mm) were purchased from Merck. Milli-Q water was prepared passing doubly distilled water through a Milli-Q apparatus.

5.1.2 Porphyrins Characterization

^{1}H-NMR and ^{19}F spectra were recorded on a Bruker Avance DRX-400 in $CDCl_3$, or in THF–d_8 (Cambridge Isotope Laboratories, Inc.). Mass spectra were obtained with a Bruker-Daltonics ICR-FTMS APEX II with an electrospray ionization source or on a VG Autospec M246 magnetic mass spectrometer with a LSIMS ionic source). Elemental analysis was carried out with a Perkin-Elmer CHN 2400 instrument. TGA analysis was performed on a TGA 7 Perkin Elmer instrument, connected to a TAC 7/DX interface and a gas selector to choose between air and nitrogen. The analysis was conducted in air, with a heating rate of 20$°C\ min^{-1}$, ranging from 30 to 800$°C$.

5.1.3 Spectroscopic Analysis

Electronic absorption spectra of porphyrin dyes in solution were recorded at room temperature in THF, using a Shimadzu UV3600 spectrophotometer and quartz cuvettes with 1 cm optical path length. Diffuse Reflectance Spectroscopy (DRS) was conducted using a double beam UV-Vis–NIR scanning spectrophotometer (Shimadzu UV-3600 plus,

Tokyo, Japan) equipped with a diffuse reflectance accessory (integrating sphere from BIS-603). The spectra were recorded in the wavelength range 220–2600 *nm*. The finely ground powder sample was uniformly pressed in a circular disk (with an external diameter of 0.2 *cm*) included in the sample holder; the latter was inserted in a special quartz cuvette and then fixed on a window of the integrating sphere for the reflectance measurements. $BaSO_4$ was the reflectance reference compound.

5.1.4 Electrochemical Analysis

The electrochemical studies of porphyrins in solution (*sections I and II*) were performed in a 4 *cm³* cell, with $5 \cdot 10^{-4}$ *M* solutions in DMF (Aldrich, 99.8%) with 0.1 *M* Tetrabutylammonium hexafluorophosphate (TBAPF$_6$, Fluka) as the supporting electrolyte. The solutions were deaerated by N_2 bubbling. The ohmic drop were compensated by the positive feedback technique.[155] The experiments were carried out using an AUTOLAB PGSTAT potentiostat (EcoChemie, The Netherlands) run by a PC with GPES software. Cyclic voltammetry (CV) investigations were carried out at scan rates typically ranging 0.05 to 2 *V s⁻¹*; differential pulse voltammetry (DPV) curves (step potential: 5 *mV*, modulation amplitude: 50 *mV*) were also recorded for each compound as both oxidative and reductive scans. The working electrode was a glassy carbon one (AMEL, diameter = 1.5 *mm*) cleaned by synthetic diamond powder (Aldrich, diameter = 1 *μm*) on a wet cloth (STRUERS DP-NAP); the counter electrode was a platinum disk or wire. The operating reference electrode was an aqueous saturated calomel electrode SCE, but the potentials were ultimately referred to the Fc⁺/Fc (104errocenium/ferrocene) couple. To prevent water and chloride leakage into the working solution a compartment filled with the operating medium and ending with a porous frit was interposed between the reference electrode and the cell. Differential pulse voltammetry (DPV) experiments were carried out under the same condition used for CV, to better identify the $E_{p,Ia}$ and $E_{p,Ic}$, affording the calculation of $E^{0'}_{Ia}$ and $E^{0'}_{Ic}$ by the following equations:

$$E^{0'}_{Ia} = E_{p,Ia} + \Delta E/2$$

$$E^{0'}_{Ic} = E_{p,Ic} - \Delta E/2$$

where ΔE is the modulation amplitude.

Voltametric studies of porphyrins of *section III* were performed in in a 22 *cm³* cell with 0.1M TBAPF$_6$/DMF, at a concentration of 0.5 *mM* of porphyrin. The working electrode was a 1 mm-diameter glassy carbon (Tokai) disk carefully polished using decreasing size of diamond paste (from 15 to 1 μm), ultrasonically rinsed in absolute ethanol and dried before use. The counter-electrode was a platinum wire, and the reference electrode was an aqueous SCE electrode. To prevent water and chloride leakage into the working solution a compartment filled with the operating medium and ending with a porous frit was interposed between the reference electrode and the cell. All experiments were carried out under argon or carbon dioxide atmosphere at 25 °C. Cyclic voltamograms were obtained by use of a Metrohm AUTOLAB instrument. Ohmic drop was compensated using the positive feedback compensation implemented in the instrument. The FOWA analysis required the extraction of i^0_p and E^0 from the CVs of all the considered porphyrins, at different PhOH concentration. The data were then used to obtain a graph of i/ i^0_p in function of $\frac{1}{1+\exp[\frac{F}{RT}(E-E^0)}$. Considering the linear part of this last graph it was possible to calculate the *k* considering that slope of the straight line is equal to $2.24\sqrt{\frac{RT}{Fv}}\sqrt{2KC_a}$. where *v* is the speed of the CV and C$_a$ is the concentration of the porphyrin. The method is exhaustively explained with examples in literature.[125,156] Controlled Potential Electrolysis were performed using a Princeton Applied Research (PARSTAT 2273) potentiostat. The experiments were carried out in a 22 *cm³* cell with 0.1M TBAPF$_6$/DMF, at a concentration of 0.5 *mM* of porphyrin, adding 500 *equivalents* of PhOH (total volume of the solution 3 *mL*). The reference electrode was an aqueous SCE electrode, and the counter electrode was a platinum wire in a bridge separated from the cathodic compartment by a glass frit, 0.1M TBAPF$_6$/DMF solution. The electrolysis solution was purged with CO$_2$ during 20 *min* prior to electrolysis. The ohmic drop between working and reference electrodes was using the feedback compensation technique. Gas chromatography analyses of gas evolved in the headspace during the electrolysis were performed with an Agilent Technologies 7820A GC system equipped with a thermal conductivity detector. CO and H2 production was quantitatively detected using a CPCarboPlot P7 capillary column (27.46 m in length and 25 μm internal diameter). Temperature was held at 150 °C for the detector and 34 °C for the oven. The carrier gas was argon flowing at 9.5 mL/min at constant pressure of 0.5 bars. Injection

was performed via a 250-μL gas-tight (Hamilton) syringe previously degassed with CO2. Conditions allowed detection of H2, O2, N2, CO, and CO2. Calibration curves for H2 and CO were determined separately by injecting known quantities of pure gas.

5.1.5 Nanocomposites Characterization and Sensing Test (*section II*)

The nanocomposites of *section II* were characterized by Diffuse Reflectance Spectroscopy (DRS), using a double beam UV-Vis–NIR scanning spectrophotometer (Shimadzu UV-3600 plus, Tokyo, Japan) equipped with a diffuse reflectance accessory (integrating sphere from BIS-603). The spectra were recorded in the wavelength range 220–2600 *nm*. The finely ground powder sample was uniformly pressed in a circular disk (with an external diameter of 0.2 *cm*) included in the sample holder; the latter was inserted in a special quartz cuvette and then fixed on a window of the integrating sphere for the reflectance measurements. $BaSO_4$ was the reflectance reference compound. Nanocomposites were deposited by a hot-spray method on glass interdigitated platinum electrodes (Pt-IDEs) and sensing tests were carried out using a custom-built stainless-steel cell, as deeply described in authors' previous works.[157,158] In particular, the electrode resistance was measured while flowing a simulated air (80% N_2 – 20% O_2) gas mixture (with total flow rate of 0.5 *L min^{-1}*) in the presence of different concentrations of acetone gaseous molecules. The flow of the target analyte was varied by dilution from a starting 500 ppm concentration (in N_2 gas mixture) keeping constant the total flow rate. The dynamic response was recorded by an Autolab PGStat30 (Eco Chemie, Utrecht, The Netherlands) potentiostat/galvanostat controlled by NOVA 2.0 software, applying a constant bias of +1.0 *V*. The sensor signal is reported as (R_{air} / $R_{acetone}$) – 1, together with the relative response and recovery times, according to previous literature.[157,158] All the tests were performed at relative humidity lower than 2% and at (120 ± 2) *℃*, and for some of them LED light (THORLABS, at fixed wavelength of 455 *nm*, power of 2 *W*) were also adopted.

5.1.6 DFT Calculations

In *section I,* the geometry optimization of the porphyrin structures was performed with Gaussian 09 A2.[159] First equilibrium geometries were computed in vacuo (restricted B3LYP-LANL2DZ) and the geometry output and wavefunction from such calculation were

used to refine the ground state geometry at the DFT-B3LYP/LANL2DZ level in THF described as a polarizable dielectric continuum model (Integral Equation Formalism Continuum Polarization Model, IEFCPM).[160] TD-DFT spectra were computed in THF at the B3LYP/6-311g(d)/LANL2DZ functional[161] by considering the first 30 lowest energy vertical excitations. Kohn Sham (KS) molecular orbitals were visualized as isodensity (isovalue 0.001) surfaces with Gaussview 5. Wavefunction analysis and EDDM of the optical transitions were obtained with Multiwfn 3.3.9.[162] *Ab initio* calculations of *section II* on the tetragonal rutile structure of SnO_2 were performed using DFT as implemented in the SIESTA code, choosing PBE as the exchange-correlation functional. Norm-conserving pseudopotentials for Sn and O were generated, based on the Troullier-Martins parameterization.[163] The basis set for both atoms is of DZP type with standard parameters. Bulk phase calculations were performed on a $22 \times 10 \times 7$ *k*-point grid in the 12 atoms tetragonal unit cell, using a 450 Ry as mesh cutoff. A suitable cell of SnO_2 for a reliable description of the adsorption of ZnTPP/ZnTPPF$_{20}$ has been chosen as a 6×3 (110) surface unit cell and 2 trilayers in direction perpendicular to the surface. This choice corresponds to mass ratios between the adsorbed porphyrins and the SnO_2 slab equal to 1/16 and ~1/10 for ZnTPP/SnO_2 and ZnTPPF$_{20}$/SnO_2, respectively. The vacuum amounts to 10 Å. The 2D periodic system is thus constituted by 72 Sn atoms and 144 O atoms. The Brillouin zone sampling is $4 \times 4 \times 1$ *k*-points. In order to overcome the heavy band gap underestimation typical of pure functionals such as PBE, if necessary, we applied to the oxygen pseudopotential the half-occupation technique described by Ferreira *et al.*,[164,165] which led to great improvements in the band gap value. After the treatment, the latter increased from 0.743 *eV* to 3.20 *eV*, which is much closer to the experimental gap 3.597 *eV* reported in literature.[166] *For section III* optimizations and frequency calculations were done using the Gaussian 16 software suite (Revision B.01; Gaussian, Inc.: Wallingford, CT, USA, 2016). All geometries were optimized using the B97D3 functional,[167] the def2-TZVP basis set[168] and W06 density fitting to increase computational efficiency.[169] Frequency calculations at this level of theory confirmed stationary points and transition states and were used to compute thermodynamic properties. Electrostatic potential maps were obtained via the Gaussian 16 cubegen standalone package and plotted using the Chemcraft graphical software (Version 1.8, build 682). In section IV we used the Gaussian16 suite of programs (Revision A.03;

Gaussian, Inc.: Wallingford, CT, USA, 2016) to perform DFT calculations. We optimized the molecular geometry with the 6-311G(d) basis set using the PBE0 functional in CH_2Cl_2, and we adopted the Polarized Continuum Model in its integral equation formalism (IEFPCM) to describe the solvent effect.[170] We modelled graphene as a single layer of 14 condensed benzene rings and we anchored the porphyrin moiety on the centre of the graphene-like system in order to minimize boundary effects. We computed the Second Harmonic Generation (SHG) first, $\beta(-2\omega; \omega, \omega)$ and second, $\gamma(-2\omega; \omega, \omega, 0)$), hyperpolarizability tensors by the Coupled Perturbed Kohn–Sham (CPKS) approach and by the Finite Field technique, respectively, at the same frequency of the EFISH experiments (1907 nm). We performed hyperpolarizability calculations at LC-BLYP/6-31G(d) level, in agreement with what was suggested by Wergifosse and Champagne in their thorough investigation on electron correlation effects on the first hyperpolarizability of push–pull π-conjugated systems with polyene and polyyne linkers.[171] We selected a pruned (99,590) grid for computation and use of two-electron integrals and their derivatives. From the full tensors β and γ, we derived the scalar quantities $\beta_\parallel$ and $\gamma_\parallel$, respectively, to have a meaningful comparison with the experimental data. $\beta_\parallel$ corresponds to 3/5 times β_λ, the projection along the dipole moment direction of the vectorial component of the β tensor, that is, $\beta_\parallel = (3/5) \sum_i (\mu_i \beta_i)/\mu$, where $\beta_i = (1/5)\sum_j(\beta_{ijj} + \beta_{jij} + \beta_{jji})$. $\Gamma_\parallel$ is related to the tensor components according to the following: $\gamma_\parallel = (1/15) [3(\gamma_{xxxx} + \gamma_{yyyy} + \gamma_{zzzz}) + 2(\gamma_{xxyy} + \gamma_{xxzz} + \gamma_{yyzz} + \gamma_{yyxx} + \gamma_{zzxx} + \gamma_{zzyy}) + (\gamma_{xyyx} + \gamma_{xzzx} + \gamma_{yzzy} + \gamma_{yxxy} + \gamma_{zxxz} + \gamma_{zyyz})]$.[172]

5.1.7 GNP and Hybrid Materials Characterization (*section IV*)

We characterized GNP by Scanning Electron Microscopy (SEM) analysis, carried out with a TESCAN VegaII at 10 KV of voltage acceleration with a working distance of 14.67 mm. (Tescan, Brno, Czech Republic). We recorded the UV–Vis electronic absorption spectra of ZnP-GNP and Fc-ZnP-GNP in CH_2Cl_2 solution at room temperature on a Shimadzu UV 3600 spectrophotometer (Shimadzu Corporation, Kyoto, Japan).

5.1.8 EFISH Measurements

For the EFISH experiments, we used freshly prepared 10^{-3} *M* solutions in CH_2Cl_2. We chose a 1.907 μm laser incident wavelength since its second harmonic (at 953 nm) is far

enough from the absorption bands of the chromophores in CH_2Cl_2 (see *paragraph 4.3.3*), that is a necessary requirement to avoid any resonance effect on the second order NLO response. We obtained the incident 1.907 *μm* wavelength by Raman shifting the 1.064 *μm* emission of a Q-switched Nd:YAG laser in a high pressure hydrogen cell (60 *bar*). The Maker fringe pattern, typical of the EFISH signal, was obtained through a liquid cell with thick windows in the wedge configuration. In the experiment, we synchronized the incident beam with a DC field applied to the solution, with 60 and 20 *ns* pulse duration, respectively, in order to break its centrosymmetry. We assumed the NLO response to be real because we neglected the imaginary part, and derived it from the experimental γ_{EFISH} value from the *equation 9* (see *section 4.1.2*)

$$\gamma_{EFISH} = \frac{\mu\beta_\lambda(-2\omega;\omega,\omega)}{5kT} + \gamma(-2\omega;\omega,\omega,0) \qquad (9)$$

We performed the EFISH experiments at the Department of Chemistry of the University of Milano (Italy), on a prototype apparatus made by SOPRA (Paris, France), recording firstly the second order response of the pure solvent, then the second order response of the chromophore in solution, and finally the second order response of the solvent again. The EFISH values reported in this paper are the average of twelve consecutive measurements performed on the same sample. The uncertainty of the measure is about ±15%, and the experimental EFISH $\beta_{1.907}$ values are defined according to the "phenomenological" convention.[173]

5.2| SYNTHETIC PROCEDURES of PORPHYRINS

5.2.1 *meso*-F19

Synthesis of TFP-N_3

In a dry Schlenk tube, under N_2 flow, 300 *mg* of TFP ($3.1 \cdot 10^{-1}$ *mmol*, 1.00 *eq.*) were dissolved in 15 *mL* of dry DMF and 20 *mg* of NaN_3 ($3.1 \cdot 10^{-1}$ *mmol*, 1.00 *eq.*) were added portion wise. The mixture was allowed to react under vigorous stirring at 60 *°C* overnight. After the removal of the solvent *in vacuo*, the solid was dissolved in CH_2Cl_2 and washed with water (3x20 *mL*). The organic layer was dried over Na_2SO_4 and the solvent evaporated. The crude was purified by column chromatography (eluent: *n*-hexane/CH_2Cl_2 7:3) leading to 141 *mg* of pure ZnTFP-N_3 (yield 47%).

^1H-NMR (400 *MHz*, CDCl$_3$, 25°C) δ, *ppm*: 8.94 (s, 8H), -2.88 (s, 2H)

^{19}F-NMR (400 *MHz*, CDCl$_3$, 25°C) δ, *ppm*: -136.79 (dd, 6F), -137.44 (dd, 2F), -151.55 (m, 3F), -151.85 (dd, 2F), -161.49 (m, 6F)

Synthesis of ZnTFP-*N$_3$*

In a two-neck round-bottomed flask, 115 *mg* of Zn(OAc)$_2$·*2H$_2$O* (5.2·10^{-1} *mmol*, 4.00 *eq.*) were added to a solution of 131 *mg* of TFP-*N$_3$* (1.3·10^{-1} *mmol*, 1.00 *eq.*) in CH$_3$OH (80 *mL*). The mixture was refluxed for 3h then cooled to RT and the solvent evaporated *in vacuo*. The crude was filtered over a Hirsch funnel and washed thoroughly with deionized water then dried overnight *under vacuum* affording ZnTFP-*N$_3$* as a purple powder in almost quantitative yield (139 *mg*).

^1H-NMR (400 *MHz*, CDCl$_3$, 25°C) δ, *ppm*: 9.02 (s, 8H)

^{19}F-NMR (400 *MHz*, CDCl$_3$, 25°C) δ, *ppm*: -137.07 (m, 6F), -137.66 (dd, 2F), -151.99 (dd, 3F) -152.35 (dd, 2F), 161.82 (m, 6F)

Synthesis of ZnTFP-*CHO*

In a dry Schlenk tube, 50 *mg* of ZnTFP-*N$_3$* (4.7·10^{-2} *mmol*, 1.00 *eq.*) and 15 *mg* of BTD-3 (5.6·10^{-2} *mmol*, 1.20 *eq.*) were dissolved in dry THF (10 *mL*) under nitrogen atmosphere. At the mixture were added two aqueous solutions prepared with degassed Milli-Q water: a) 14 *mg* of CuSO$_4$×*5H$_2$O* (5.6·10^{-2} *mmol*, 1.20 *eq.*) in 2 *mL* of H$_2$O; b) 11 *mg* of sodium ascorbate (SAA: 5.6·10^{-2} *mmol*, 1.20 *eq.*) in 2 *mL* of H$_2$O. After 48 hours at 50°C the solvent was removed under *vacuum,* the crude was extracted with 40 *mL* of CH$_2$Cl$_2$ and washed with water (3x20 *mL*). The collected organic phases were dried over Na$_2$SO$_4$ and the solvent evaporated. The pure product was purified by flash chromatography (eluent: n-hexane/AcOEt = from 9:1 to 8:2), yielding 26 *mg* of ZnTFP-*CHO* (yield 44%)

^1H-NMR (400 *MHz*, CDCl$_3$, 25°C) δ, *ppm*: 9.92 (s, 1H), 9.57 (s, 1H), 9.13 (d, 2H), 9.08 (d, 2H), 9.03 (s, 4H), 8.86 (d, 1H), 8.23 (d, 2H), 8.04 (m, 3H)

^{19}F-NMR (400 *MHz*, CDCl$_3$, 25°C) δ, *ppm*: -134.92 (m, 2F), -137.09 (m, 6F), -146.65 m, (2F), -152.12 (m, 3F), -161.96 (m, 6F)

*Synthesis of **meso*-F19**

In a dry Schlenk tube, under nitrogen flow, 65 *mg* of ZnTFP-*CHO* (4.9·10^{-2} *mmol*, 1.00 *eq.*)

were dissolved into 2 *mL* of toluene and 21 *mg* of cyanoacetic acid (CAA: $2.5 \cdot 10^{-1}$ *mmol*, 5.00 *eq.*) added to the mixture. After adding 48 *μL* of piperidine ($4.9 \cdot 10^{-1}$ *mmol*, 10.0 eq) and 9 *μL* of freshly distilled triethylamine ($6.4 \cdot 10^{-2}$ *mmol*, 1.30 *eq.*) the mixture was allowed to react at 90°C overnight. The reaction was quenched with 10 *mL* of $H_3PO_{4(aq)}$ 0.20 *M* and washed with CH_2Cl_2. The organic layer was dried over Na_2SO_4 and filtered across a silica plug starting to remove the impurities. The pure final product *meso*-F19 was collected with CH_2Cl_2/CH_3OH (9:1) by yielding, after solvents removal, a purple-greenish amorphous solid (61 *mg*, 87% yield).

^{1}H-NMR (400 *MHz*, THF-d_8, 25°C) *δ*, *ppm*: 9.76 (s, 1H), 9.28 (d, 2H), 9.17 (d, 2H), 9.13 (d, 4H), 8.92 (d, 1H), 8.37 (m, 3H), 8.26 (m, 3H)

^{19}F-NMR (400 *MHz*, THF-d_8, 25°C) *δ*, *ppm*: -138.72 (m, 2F), -139.83 (m, 6F), -149.72 (m, 2F), -156.25 (m, 3F), -165.50 (m, 6F)

MS-ESI(-): *m/e* 1390.41 [M]⁻ (calcd. for $C_{62}H_{17}F_{19}N_{10}O_2SZn$ 1390.02)

Anal. Calcd. (found): C, 53.49 (53.62); H 1.23 (1.23); N, 10.06 (10.04)

5.2.2 *meso*-F16

Synthesis of ZnTFP

In a two-neck round-bottomed flask, 433 *mg* of $Zn(OAc)_2 \cdot 2H_2O$ (1.97 *mmol*, 4.00 *eq.*) were added to a solution of 500 *mg* of TFP ($5.1 \cdot 10^{-1}$ *mmol*, 1.00 *eq.*) in CH_3OH (80 *mL*). The mixture was refluxed for 3h then cooled to RT and the solvent evaporated *in vacuo*. The crude was filtered over a Hirsch funnel and washed thoroughly with deionized water then dried overnight *under vacuum* ZnTFP as a purple powder in almost quantitative yield (520 *mg*).

^{1}H-NMR (400 *MHz*, CDCl₃, 25°C) *δ*, *ppm*: 9.03 (s, 8H)
^{19}F-NMR (400 *MHz*, CDCl₃, 25°C) *δ*, *ppm*: -136.73 (m, 8F), -151.75 (m, 4F), -161.9 (m, 8F)

Synthesis of Zn3DP

In a dry Schlenk tube, under nitrogen flow, 400 *mg* of ZnTFP ($3.9 \cdot 10^{-1}$ *mmol*, 1.00 *eq.*), 71 *mg* of $(CH_3)_2NH \cdot HCl$ (1.27 *mmol*, 3.30 *eq.*) and 71 *mg* of KOH (1.27 *mmol*, 3.30 *eq.*) were dissolved in 16 *mL* of dry DMF. The mixture was allowed to react at 110°C

overnight then the solvent removed under *vacuum*. The solid residue was dissolved in 20 *mL* of CH_2Cl_2 and washed with water (3x10 *mL*). After drying the organic phases over Na_2SO_4 the solvent was evaporated, and the product purified by flash chromatography (eluent: n-hexane/CH_2Cl_2 from 65:35 to 100% CH_2Cl_2) affording 205 *mg* of Zn3DP as a purple solid (yield 40%).

^1H-NMR (400 *MHz*, $CDCl_3$, 25 *°C*) *δ*, *ppm*: 9.14 (d, 2H), 9.12 (s, 4H) 9.02 (d, 2H), 3.29 (s, 18H)

^{19}F-NMR (400 *MHz*, $CDCl_3$, 25 *°C*) *δ*, *ppm*: -136.72 (m, 2F), -140.35 (m, 6F), -152.35 (m, 7F), -162.05 (m, 2F)

Synthesis of Zn3DP-*N₃*

In a dry Schlenk tube, under N_2 flow, 80 *mg* of Zn3DP (7.2·10^{-2} *mmol*, 1.00 *eq.*) were dissolved in 8 *mL* of dry DMF and 19 *mg* of solid NaN_3 (2.9·10^{-1} *mmol*, 4.00 *eq.*) were added portionwise. The mixture was allowed to react under vigorous stirring at 60 *°C* overnight. After the removal of the solvent the *in vacuo*, the solid was dissolved in CH_2Cl_2 and washed with water (3x20 *mL*). The organic layer was dried over Na_2SO_4 and the solvent evaporated leading to pure Zn3DP-*N₃* in almost quantitative yield (80 *mg*).

^1H-NMR (400 *MHz*, $CDCl_3$, 25 *°C*) *δ*, *ppm*: 9.02 (m, 6H), 8.93 (m, 2H), 3.30 (s, 18H)

^{19}F-NMR (400 *MHz*, $CDCl_3$, 25 *°C*) *δ*, *ppm*: -137.63 (m, 2F), -140.56 (m, 6F), -152.75 (m, 8F)

Synthesis of Zn3DP-*CHO*

In a dry Schlenk tube, 46 *mg* of Zn3DP-*N₃* (4.0·10^{-2} *mmol*, 1.00 *eq.*) and 13 *mg* of BTD-3 (4.9·10^{-2} *mmol*, 1.20 *eq.*) were dissolved in dry THF (10 *mL*) under nitrogen atmosphere. At the mixture were added two aqueous solutions prepared with degassed Milli-Q water: a) 12 *mg* of $CuSO_4×5H_2O$ (4.9·10^{-2} *mmol*, 1.20 *eq.*) in 2 *mL* of H_2O; b) 10 *mg* of sodium ascorbate (SAA: 4.9·10^{-2} *mmol*, 1.20 *eq.*) in 2 *mL* of H_2O. After 48 hours at 50 *°C* the solvent was removed under *vacuum,* the crude was extracted with 40 *mL* of CH_2Cl_2 and washed with water (3x20 *mL*). The collected organic phases were dried over Na_2SO_4 and the solvent evaporated. The pure product was purified by flash chromatography (eluent: n-hexane/AcOEt from 9:1 to 7:3), yielding 37 *mg* of Zn3DP-*CHO* (yield 66%).

^1H-NMR (400 *MHz*, CDCl$_3$, 25°C) *δ*, *ppm*: 9.78 (s, 1H), 9.51 (s, 1H), 9.16 (d, 2H), 9.10 (s, 4H), 9.06 (d, 2H), 8.70 (d, 1H), 8.14 (d, 2H), 7.945 (m, 3H), 3.31 (s, 18H)

^{19}F-NMR (400 *MHz*, CDCl$_3$, 25°C) *δ*, *ppm*: -134.88 (m, 2F), -140.50 (m, 6F), -147.08 m, (2F), -152.50 (m, 6F)

Synthesis of *meso*-F16

In a dry Schlenk tube, under N$_2$ flow, 60 *mg* of Zn3DP-*CHO* (4.3·10^{-2} *mmol*, 1.00 *eq.*) were dissolved in 2 *mL* of toluene and 18 *mg* of cyanoacetic acid (CAA: 2.1·10^{-1} *mmol*, 5.00 *eq.*) added to the mixture. After adding 42 *μL* of piperidine (4.3·10^{-2} *mmol*, 10.0 eq.) and 8 *μL* of freshly distilled triethylamine (5.8·10^{-2} *mmol*, 1.30 *eq.*) the mixture was allowed to react at 90°C overnight. The reaction was quenched with 10 *mL* of H$_3$PO$_{4(aq)}$ 0.20 *M* and the product extracted with CH$_2$Cl$_2$. The organic layer was dried over Na$_2$SO$_4$ and filtered across a silica plug to remove unreacted materials. The pure final product *meso*-F16 was collected using a mixture of CH$_2$Cl$_2$/CH$_3$OH (9:1) by yielding, after evaporation of the solvents, 50 mg of a dark purple powder (79%).

^1H-NMR (400 *MHz*, THF-d_8, 25°C) *δ*, *ppm*: 9.74 (s, 1H), 9.20 (d, 2H), 9.09 (d, 2H), 9.04 (s, 4H), 8.90 (d, 1H), 8.33 (m, 3H), 8.23 (m, 3H), 3.30 (d, 18H)

^{19}F-NMR (400 *MHz*, THF-d_8, 25°C) *δ*, *ppm*: -138.65 (m, 2F), -142.50 (m, 6F), -149.91 (m, 2F), -154.25 (m, 6F).

MS-ESI(-): *m/e* 1466.30 [M-1]$^-$ (calcd. for C$_{68}$H$_{35}$F$_{16}$N$_{13}$O$_2$SZn 1467.03)

Anal. Calcd. (found): C, 55.65 (55.79); H 2.40 (2.39); N, 12.41 (12.41)

5.2.3 β-F16

Synthesis of Zn4DP

In a dry Schlenk tube, under nitrogen flow, 500 *mg* of ZnTFP (4.8·10^{-1} *mmol*, 1.00 eq.), 157 *mg* of (CH$_3$)$_2$NH·HCl (1.9 *mmol*, 4.00 eq.), and 216 *mg* of KOH (3.8 *mmol*, 8.00 eq.), were dissolved in 20 *mL* of dry DMF. The solid residue was dissolved in 20 *mL* of CH$_2$Cl$_2$ and washed with water (3x10 *mL*). After drying the organic phases over Na$_2$SO$_4$ the solvent was evaporated, and the product purified by flash chromatography (eluent: 100% CH$_2$Cl$_2$) affording Zn4DP as a purple powder (80% yield).

^1H-NMR (400 MHz, CDCl$_3$, 25°C) δ, ppm: 8.96 (s, 8H) 3.31 (s, 24H)

^{19}F-NMR (400 MHz, CDCl$_3$, 25°C) δ, ppm: -139.97 (m, 8F), -152.13 (m, 8F)

Synthesis of Zn4DP-*Br*

In a round bottomed flask, 537 *mg* of Zn4DP ($4.7·10^{-1}$ *mmol*, 1.00 eq.) were dissolved in 250 *mL* of CH$_3$OH and 84 *mg* of NBS ($4.7·10^{-1}$ *mmol*, 1.00 eq.) were added. The solution was vigorous stirred overnight at room temperature then the solvent removed under *vacuum*. The solid residue was dissolved in 20 *mL* of CH$_2$Cl$_2$ and washed with water (3x10 *mL*). After drying the organic phases over Na$_2$SO$_4$ the solvent was evaporated, and the crude passed through a silica plug with CH$_2$Cl$_2$ providing a mixture of unreacted Zn4DP and brominated derivatives. The resulting purple powder, containing about 70% of the desired Zn4DP-*Br* (determined by NMR analysis), was used as obtained in the next step reaction.

^1H-NMR (400 MHz, CDCl$_3$, 25°C) δ, ppm: 9.17 (s, 1H), 9.06-9.02 (m, 6H), 3.32 (m, 24H)

^{19}F-NMR (400 MHz, CDCl$_3$, 25°C) δ, ppm: -140.15 (m, 6F), -140.50 (m, 2F), -152.15 (m, 6F), -153.10 (m, 2F)

Synthesis of Zn4DP-*Si*

In a microwave reaction tube equipped with a stirring bar, 50 *mg* of the mixture containing Zn4DP-*Br* (ca $2.8·10^{-2}$ *mmol*, 1.00 eq.), 25 *mg* of ethynyltrihexylsilane ($8.1·10^{-2}$ *mmol*, 2.89 eq) and 6 *mg* of Pd(PPh$_3$)$_4$ ($0.8·10^{-2}$ *mmol*, 0.30 eq) were dissolved in 1.5 *mL* of freshly distilled triethylamine and 1 *mL* of dry DMF. The resulting mixture was bubbled for 5 min with N$_2$ before sealing the tube then it was allowed to react in the microwave cavity at 60°C for 15 min. The solvents were removed under *vacuum,* the crude dissolved in 20 *mL* of CH$_2$Cl$_2$ and washed with water (3x10 *mL*). After drying the organic phases over Na$_2$SO$_4$ the solvent was evaporated and the crude passed through a silica plug, first with 100% hexane to remove unreacted silane, then with 100% CH$_2$Cl$_2$ to collect porphyrin fraction. The desired product Zn4DP-*Si* was then isolated by flash chromatography (eluent: n-hexane/CH$_2$Cl$_2$ from 8:2 to 100% CH$_2$Cl$_2$) as a purple amorphous solid (20 *mg*, 50% yield)

^1H-NMR (400 MHz, CDCl$_3$, 25°C) δ, ppm: 9.23 (s, 1H), 9.02 (m, 4H), 8.98 (d, 1H), 8.89 (d, 1H), 3.34 (s, 6H), 3.31 (s, 18H), 1.38-0.79 (m, 39H)

^{19}F-NMR (400 MHz, CDCl$_3$, 25°C) δ, ppm: -139.98 (m, 6F), -140.56 (m, 2F), -152.39 (m, 6F), -154.07 (m, 2F)

Synthesis of Zn4DP-CH

In a dry Schlenk tube, under N$_2$ flow, 0.079 mL of TBAF (1 M in THF; $7.9 \cdot 10^{-2}$ $mmol$, 2.00 eq.) were added dropwise to a stirring solution of 57 mg ($3.9 \cdot 10^{-2}$ $mmol$, 1.00 eq.) of Zn4DP-*Si* in 10 mL of THF. The mixture was stirred for 1 hour at RT, then the reaction was quenched with H$_2$O. The product was extracted with CH$_2$Cl$_2$ and washed with water (3x10 mL), the organic phase dried over Na$_2$SO$_4$ and the solvent evaporated *in vacuo*. The crude was purified by gravimetric chromatography (eluent: from n-hexane 100% to CH$_2$Cl$_2$ 100%) affording Zn4DP-*CH* as a purple powder in almost quantitative yield (50 mg).

^{1}H-NMR (400 MHz, CDCl$_3$, 25°C) δ, ppm: 9.32 (s, 1H), 9.12 (d, 1H), 9.04 (m, 5H), 3.63 (s, 1H), 3.28 (m, 24H)

^{19}F-NMR (400 MHz, CDCl$_3$, 25°C) δ, ppm: -140.50 (m, 6F), -140.90 (m, 2F), -152.60 (m, 6F), -153.93 (m, 2F)

Synthesis of Zn4DP-CHO

In a dry Schlenk tube, under N$_2$ flow, 50 mg of Zn4DP-*CH* ($4.0 \cdot 10^{-2}$ $mmol$, 1.00 eq.), 27 mg of BTD-1 ($8.0 \cdot 10^{-2}$ $mmol$, 2.00 eq.) and 7.5 mg of Pd(PPh$_3$)$_4$ ($0.6 \cdot 10^{-2}$ $mmol$, 0.15 eq.) were dissolved in 5 mL of freshly distilled triethylamine and 5 mL of dry THF. After bubbling N$_2$ for 10 min the mixture was allowed to react at 70°C overnight. After the evaporation of the solvent *in vacuo*, the mixture was dissolved in 20 mL of CH$_2$Cl$_2$ and washed with H$_2$O (3x10 mL). The organic phase was dried over Na$_2$SO$_4$ and the solvent evaporated. The pure Zn4DP-*CHO* was isolated as a purple-greenish powder (35 mg, 60% yield) by two consecutive gravimetric chromatography columns (*eluent 1*: toluene/AcOEt 99:1; *eluent 2*: from 100% n-hexane to n-hexane/AcOEt 3:1).

^{1}H-NMR (400 MHz, CDCl$_3$, 25°C) δ, ppm: 9.96 (s, 1H), 9.45 (s, 1H), 9.05 (m, 6H), 8.20 (d, 2H), 8.03 (d, 2H), 7.97 (d, 1H), 7.88 (d, 1H), 3.30 (m, 18H), 2.60 (m, 6H).

^{19}F-NMR (400 MHz, CDCl$_3$, 25°C) δ, ppm: -140.34 (m, 8F), -152.44 (m, 6F), -153.45 (m, 2F)

Synthesis of **β-F16**

In a dry Schlenk tube, under N_2 flow, 35 *mg* of Zn4DP-*CHO* ($2.5 \cdot 10^{-2}$ *mmol*, 1.00 eq.) were dissolved in 1 *mL* of toluene and 10 *mg* of cyanoacetic acid (CAA: 12.5 *mmol*, 5.00 eq.) added to the mixture. After adding 25 *μL* of piperidine ($2.5 \cdot 10^{-1}$ *mmol*, 10.0 eq.) and 5 *μL* of triethylamine ($3.3 \cdot 10^{-2}$ *mmol*, 1.30 eq.) the mixture was allowed to react at 90°C overnight. The reaction was quenched with 10 *mL* of $H_3PO_{4(aq)}$ 0.20 *M* and the product extracted with CH_2Cl_2. The organic layer was dried over Na_2SO_4 and filtered across a silica plug with CH_2Cl_2 to remove unreacted materials. The desired product β-F16 was collected using a mixture of CH_2Cl_2/CH_3OH (9:1) by yielding, after evaporation of the solvents, 32 mg of a purple- greenish amorphous solid (88%).

^1H-NMR (400 *MHz*, THF-d_8 + 1 drop of D_2O, 25°C) *δ, ppm*: 9.41 (s, 1H), 9.04 (m, 6H), 8.46 (s, 1H), 8.39 (d, 2H), 8.31 (d, 2H), 8.16 (d, 1H), 8.06 (d, 1H), 3.37 (m, 18H), 2.59 (s, 6H).

^{19}F-NMR (400 *MHz*, THF-d_8 + 1 drop of D_2O, 25°C) *δ, ppm*: -141.98 (m, 2F), -142.34 (m, 6F), -153.89 (m, 6F), -154.54 (m, 2F).

MS-ESI(-): *m/e* 1465.44 [M]$^-$ (calcd. for $C_{70}H_{39}F_{16}N_{11}O_2SZn$ 1465.20)

Anal. Calcd. (found): C, 57.29 (57.40); H 2.68 (2.67); N, 10.50 (10.49)

5.2.4 β-TFP

Synthesis of ZnTFP

In a two-neck round-bottomed flask, 433 *mg* of $Zn(OAc)_2 \cdot 2H_2O$ (1.97 *mmol*, 4 equivalents) were added to a solution of 500 *mg* of TFP (0.51 *mmol*, 1 equivalent) in methanol (80 *mL*), and the mixture was refluxed for 3h, then cooled to RT, and the solvent evaporated *in vacuo*. The crude was washed with purified water (30 *mL*), then dried over a Buchner filter, affording ZnTFPas a purple powder in almost quantitative yield.

^1H-NMR (400 *MHz*, CDCl$_3$, 25°C) *δ, ppm*: 9.03 (8H, s)

^{19}F-NMR (400 *MHz*, CDCl$_3$, 25°C) *δ, ppm*: -136.73 (8F, m), -151.75 (4F, m), -161.9 (8F, m)

Synthesis of ZnTFP-*Br*

In a round bottomed flask, 100 *mg* (0.096 *mmol*, 1 equivalent) of ZnTFP were dissolved in 50 *mL* of methanol. 17.1 *mg* (0.096 *mmol*, 1 equivalent) of NBS were added to the solution, which was left at room temperature and under vigorous stirring overnight. The crude was retrieved evaporating the methanol *in vacuo*, then it was dissolved in dichloromethane and washed three times with water (3x10*mL*), the organic phase was dried over Na_2SO_4 and the solvent evaporated *in vacuo*. The crude was purified by filtration on a silica plug, using Dichloromethane/ n-hexane = 3/7 as eluent. The process afforded a mixture of ZnTFP and ZnTFP-Br as a purple powder (99.7 *mg*, 75% yield of ZnTFP-Br determined by ^{1}H-NMR).

^{1}H-NMR (400 *MHz*, $CDCl_3$, 25°C) *δ*, *ppm*: 9.17 (1H, d, J = 12), 9.06 (6H, m)

^{19}F-NMR (400 *MHz*, $CDCl_3$, 25°C) *δ*, *ppm*: -136.67 (6F, m), -137.07 (2F, m), -151.79 (4F, m), -161.50 (4F, m), -162.67 (2F, m)

MS-ESI(-): *m/e* 1115.27 [M − 1] (calcd. for $C_{44}H_7BrF_{20}N_4Zn$ = 1116.07)

Synthesis of ZnTFP-*Si*

In a microwave reaction vial equipped with a stirring bar, 50 *mg* of ZnTFP-Br (0.04 *mmol*, 1 equivalent), 25 *mg* of ethynyltrihexylsilane (0.08 *mmol*, 2 equivalents) and 9.24 *mg* of palladium tetrakis (0.008 *mmol*, 0.2 equivalents) were dissolved in 1.5 *mL* of freshly distilled triethylamine and 2 *mL* of dry dimethylformamide. The resulting mixture was bubbled for 10 min with gaseous nitrogen to remove O_2, then 0.8 *mg* of CuI (0.004 *mmol*, 0.1 equivalents) were added. The vial was sealed, and the mixture was allowed to react in the microwave cavity for at 80°C for 5 minutes. The solvents were removed under *vacuum,* the crude dissolved in 20 *mL* of dichloromethane and washed with water (3x10 *mL*). The collected organic phases were dried over Na_2SO_4 and the solvent evaporated. The solid was filtrated trough a silica plug, first with 100% hexane to remove unreacted silane, then with 100% dichloromethane to collect porphyrin fraction. Finally, the pure ZnTFP-Si was obtained as a purple amorphous solid (33.6 *mg*, 62% yield) by flash chromatography (from 8/2 n-hexane/dichloromethane to 100% dichloromethane).

^{1}H-NMR (400 MHz, CDCl$_3$, 25°C) δ, ppm: 9.17 (1H, s), 8.98 (6H, m), 1.45 (24H, m), 0.94 (9H, m), 0.83 (6H, m)

^{19}F-NMR (400 MHz, CDCl$_3$, 25°C) δ, ppm: -136.56 (8F, m), -152.48 (4F, m), -161.56 (8F, m)

Synthesis of ZnTFP-*CH*

In a dry Schlenk tube, under nitrogen flow, TBAF 0.150 mL (solution 1 M in tetrahydrofuran; 0.055 $mmol$, 2 equivalents) were added dropwise under stirring to a solution of 150 mg (0.111 $mmol$, 1 equivalent) of ZnTFP-Si(hex)$_3$ in 5 mL of tetrahydrofouran. The mixture was stirred for 1 hour at RT, then the reaction was quenched with H$_2$O. The crude product was washed with water (3x10 mL) and dichlorometane (3x15 mL), the organic phase was dried over Na$_2$SO$_4$ and the solvent evaporated *in vacuo*. The crude was purified by gravimetric chromatography (eluent: from n-hexane 100% to dichloromethane 100%). Affording ZnTFP-CH as a purple powder (116.9 mg, 99% yield).

^{1}H-NMR (400 MHz, CDCl$_3$, 25°C) δ, ppm: 9.27 (1H, s), 9.01(6H, m), 3.70 (1H, s)

^{19}F-NMR (400 MHz, CDCl$_3$, 25°C) δ, ppm: -136.85 (8F, m), -151.99 (3F, m), -154.03 (1F, s), -161.92 (6F, s), -163.77 (2F, s)

Synthesis of ZnTFP-*CHO*

In a dry Schlenk tube, under nitrogen flow, 120 mg of ZnTFP-CH (0.113 $mmol$, 1 equivalent), 72 mg of 4-(7-bromobenzo[1,2,5]thiadiazol-4-yl)benzaldehyde (0.226 $mmol$, 2 equivalents) and 20 mg of palladium tetrakis (0.017 $mmol$, 0.15 equivalents) were dissolved in 7 mL of freshly distilled triethylamine and 7 mL of dry tetrahydrofuran. After bubbling gaseous N$_2$ into the solution for 10 min i to remove O$_2$ traces from the solvents, CuI 2 mg (0.011 $mmol$, 0.1 equivalents) were added. Then the mixture was kept at 70°C under vigorous stirring for 16 hours, under a nitrogen atmosphere. After the evaporation of the solvent in vacuo, the mixture in dissolved in 20 mL of Dichloromethane and washed with H$_2$O (3x10 mL). The organic phase was dried over Na$_2$SO$_4$ and the solvent evaporated. The crude was purified by gravimetric chromatography (eluent: from 100% n-hexane to 100% Dichloromethane). Pure ZnTFP-CHO was collected as a purple-greenish powder (123 mg, 83% yield).

^{1}H-NMR (400 *MHz*, CDCl$_3$, 25°C) δ, *ppm*: 10.14 (1H, s), 9.39 (1H, s), 9.00 (6H, m), 8.29 (2H, D, J = 8.1 *Hz*), 8.12 (2H, d, J = 8.1 *Hz*), 8.01 (1H, d, J = 7.3 *Hz*), 7.94 (1H, *d*, J = 7.3 *Hz*)

^{19}F-NMR (400 *MHz*, CDCl$_3$, 25°C) δ, *ppm*: -136.75 (8F, broad s), -151.81 (3F, m), -154.02 (1F, m), -162.37 (6F, broad s), -163.32 (2F, s)

Synthesis of **β-TFP**

In a dry Schlenk tube, under nitrogen flow, 44 *mg* of ZnTFP-CHO (0.033 *mmol*, 1 equivalent) were dissolved into 1 *mL* of toluene. 14.4 *mg* of cyanoacetic acid (0.169 *mmol*, 5 equivalents) was added under stirring. After the addition of 34 *μL* of piperidine (0.33 *mmol*, 10 equivalents) and 6 *μL* of triethylamine (0.33 *mmol*, 10 equivalents) the solution was heated at 90°C for 16h. After cooling down to RT the mixture was quenched with 5 *mL* of H$_3$PO$_4$ 2 *M* in water and washed with dichloromethane. The organic layer was dried over Na$_2$SO$_4$ and the solvents evaporated *in vacuo*. The crude was then purified by filtration on a silica plug starting with 100% dichloromethane to remove the impurities, and using then dichloromethane /methanol = 9/1 to collect β-TFP as a purple-greenish amorphous solid (33.5 *mg*, 73% yield)

^{1}H-NMR (400 *MHz*, THF-d$_8$ with 1 drop of D$_2$O, 25°C) δ, *ppm*: 9.54 (1H, s), 9.11 (6H, m), 8.40 (2H + 1H, A**B**, J = 8 *Hz*), 8.29 (2H, **A**B, J = 8 *Hz*), 8.19 (1H, A**B**, J = 8 *Hz*), 8.10 (1H, **A**B, J = 8 *Hz*)

^{19}F-NMR (400 *MHz*, THF-d$_8$ with 1 drop of D$_2$O, 25°C) δ, *ppm*: -136.62 (2F, d, J = 23 *Hz*),), -136.88 (6F, t, *J* = 30.1 Hz), -151.80 (3F, m), 152.97 (1F, m), -161.63 (6F, m), -162.58 (2F, m)

ESI-ITMS: *m/e* 1365.96 [M - 1]; 1368.05 [M + 1] (calcd. for C$_{62}$H$_{15}$F$_{20}$N$_7$O$_2$SZn = 1367.27)

Anal. Calcd. (found): C, 54.39 (54.54); H, 1.25 (1.26); N, 7.16 (7.15)

5.2.5 β-TPP

Synthesis of ZnTPP

A solution of 714 *mg* of Zn(OAc)$_2$·2H$_2$O (3.25 *mmol*, 4 equivalents) in CH$_3$OH (30 *mL*) was added dropwise to a solution of 500 *mg* of TPP (0.813 *mmol*, 1 equivalent) in 80 *mL* of

chloroform at reflux temperature. The mixture was then heated for another 3h. After removing the solvent in vacuo, the crude product was with methanol (30 mL) and dried over a Buchner to give ZnTPP as a purple powder in almost quantitative yield.

^{1}H-NMR (400 MHz, CDCl$_3$, 25°C) δ, ppm: 8.96 (8H, s, meso-H), 8.24 (8H, q, o-phenyl), 7.78 (12H, m, m,p-phenyl).

Synthesis of ZnTPP-*Br*

In a 250 mL round-bottom flask, 220 mg of *ZnTPP* (0.324 $mmol$, 1 equivalent) were dissolved in 150 mL of carbon tetrachloride. 0.069 mg of NBS (0.389 $mmol$, 1.2 equivalents) were added under vigorous stirring and the solution was refluxed overnight. After cooling down at RT, the solvent was evaporated *in vacuo*. The solid was then washed with methanol (30 mL) and dried over a Buchner. The process afforded a mixture of unreacted ZnTPP and ZnTPP-Br.

^{1}H-NMR (400 MHz, CDCl$_3$, 25°C) δ, ppm: 8.97 (1H, d), 8.80 (6H, m), 8.09 (8H, d, o-phenyl), 7.69 (12H, m, m,p-phenyl).

Synthesis of ZnTPP-*Si*

In a microwave quartz vessel, equipped with a magnetic stirrer, 249 mg (0.329 $mmol$, 1 equivalent) of ZnTPP-Br and 65.6 mg of Palladium Tetrakis (0.057 $mmol$, 0.1 equivalents) were added, and immediately dissolved in 14 mL of freshly distilled triethylamine, under nitrogen bubbling. 438 mg of trihexylsilylacetylen (1.64 $mmol$, 5 equivalents) e and 5 mL of dry dimethylformamide were added to the solution. Nitrogen was bubbled into the mixture for another 15 minutes and then 10 mg of CuI (0.066 $mmol$, 0.2 equivalents) were added. The vial was sealed, and the mixture was allowed to react in the microwave cavity for at 120°C for 1 hour. The crude was retrieved evaporating the solvents *in vacuo*, then it was washed with water (3x10 mL) and retrieved with DCM (3x15 mL), the organic phase was dried over Na$_2$SO$_4$ and the solvent evaporated *in vacuo*. The crude was purified by gravimetric chromatography (eluent: from 100% n-hexane, to 8/2 n-hexane/dichloromethane). 152.6 mg of the desired ZnTPP-Si(Hex)$_3$ were obtained as an oily product (47% yield).

^{1}H-NMR (400 *MHz*, CDCl$_3$, 25℃) *δ, ppm*: 9.25 (1H, s), 8.97-8.23 (6H, m), 8.21 (8H$_o$, m), 7.74 (12H$_{m,p}$, m), 1.54-1.36 (24H, m), 0.94 (9H, m), 0.72 (6H, s)

Synthesis of ZnTPP-*CH*

In a dry Schlenk tube, under nitrogen flow, 0.66 *mL* of tetrabutylammonium fluoride (solution 1 M in tetrahydrofuran; 0.66 *mmol*, 5 equivalents) were added dropwise under stirring to a solution of 125 *mg* of ZnTPP-Si(Hex)$_\mathbf{3}$ (0.132 *mmol*) in 8 *mL* of tetrahydrofuran. The mixture was stirred for 1 hour at RT, then the reaction was quenched with H$_2$O. The crude product was washed with water (3x10 *mL*) and dichloromethane (3x15 *mL*), the organic phase was dried over Na$_2$SO$_4$ and the solvent evaporated *in vacuo*. The crude solid was then washed with hexane and isopropyl ether and dried over a Buchner filter to collect ZnTPP-CH as purple powder (81.0 mg, 87% yield).

^{1}H-NMR (400 *MHz*, CDCl$_3$, 25℃) *δ, ppm*: 9.24 (1H, s), 8.93 (6H, m), 8.16 (8H$_o$, m), 7.73 (12H$_{m,p}$, m), 3.30 (1H, s)

Synthesis of ZnTPP-*CHO*

In a dry Schlenk tube, under nitrogen flow, 13.3 *mg* of palladium Tetrakis (0.012 *mmol*, 0.1 equivalents) were added to a solution of 81 *mg* of ZnTPP-CH (0.115 *mmol*, 1 equivalent) in 3.5 *mL* of freshly distilled triethylamine. 73.4 *mg* of 4-(7-bromobenzo[1,2,5]thiadiazol-4-yl)benzaldehyde (0.230 *mmol*, 2 equivalents) and 2.5 *mL* of THF were added to the mixture. After bubbling gaseous N$_2$ into the solution for 10 *min* to remove O$_2$ traces from the solvents, 2 *mg* of CuI (0.012 *mmol*, 0.1 equivalents) were added. Then the mixture was kept under vigorous stirring and heated at 70℃ for 24 hours, under a nitrogen atmosphere. The crude product was washed with water (3x10 *mL*) and then dichloromethane (3x15 *mL*), the organic phase was dried over Na$_2$SO$_4$ and the solvent evaporated *in vacuo*. The solid crude purified by gravimetric chromatography (eluent: from n-hexane/dichloromethane 5/5 to dichloromethane 100%), then washed with methanol (30 *mL*), and dried over a Buchner filter, affording ZnTPP-CHO as a purple-greenish powder (24.0 *mg*, 0.025 *mmol*, 51% yield).

^{1}H-NMR (400 *MHz*, CDCl$_3$, 25℃) *δ*, *ppm*: 10.13 (1H, s), 9.24 (1H, s), 8.85 (6H, m), 8.23 (12H, m), 7.66 (14H, m)

Synthesis of **β-TPP**

In a dry Schlenk tube, under nitrogen flow, 55.0 *mg* of ZnTPP-CHO (0.059 *mmol*, 1 equivalent) were dissolved into 4 *mL* of chloroform. A solution of 24.9 *mg* of cyanoacetic acid (0.293 *mmol*, 5 equivalents) in 0.80 *mL* of dry acetonitrile was then added under stirring. Piperidine (0.02 *mL*) was added to the mixture, which was refluxed overnight under vigorous stirring. After cooling down to RT the mixture was quenched with 5 *mL* of H$_3$PO$_4$ 2 *M* in water and washed with dichloromethane. The organic layer was dried over Na$_2$SO$_4$ and the solvents evaporated *in vacuo*. Then the solid was washed with methanol and the solvent filtered off to afford pure β-TPP (28.3 *mg*, 48% yield) as a purple-greenish powder.

^{1}H-NMR (400 *MHz*, THF-d$_8$, 25℃) *δ*, *ppm*: 9.27 (1H, s), 8.83-8.76 (6H, m), 8.23 (12H, m), 7.95 (1H, m), 7.66 (14H, m)

ESI-ITMS: *m/e* 1006.12 [M - 1] (calcd. for C$_{62}$H$_{35}$N$_7$O$_2$SZn = 1007.43)

Anal. Calcd. (found): C, 73.77 (73.98); H, 3.69 (3.68); N, 9.71 (9.70)

5.2.6 Free-base porphyrins 1-5

Synthesis of 1

In a dry two neck round-bottom flask, 150 *μL* of benzaldehyde (1.29 *mmol*, 1 equivalent) were dissolved, under argon flow, in 150 *mL* of dry CH$_2$Cl$_2$. 89.5 *μL* of freshly distilled pyrrole (1.29 *mmol*, 1 equivalent) were added to the solution. The round bottomed flask was then covered with aluminium foil to protect the reaction from ambient light, and 48 *μL* of BF$_3$(OEt)$_2$ (0.39 *mmol*, 0.3 equivalents) were added to the solution. The reaction was allowed to stir in dark, under argon atmosphere, at RT for 16 hours. After that time the aluminium foil and the argon flow were removed, 220 *mg* of DDQ (0.97 *mmol*, 0.75 equivalents) were added and the reaction was stirred 4 hours at RT exposed to air and ambient light. Finally, 180 *μL* of triethylamine (1.29 *mmol*, 1 equivalent) were added to the solution and let stir for 1 hour. The crude was retrieved evaporating the solvent *in*

vacuo, and the solid obtained was purified by gravimetric chromatography (eluent from dichloromethane/n-hexane = 1/1 to dichloromethane/n-hexane = 3/1) affording compound **1** as a purple powder (34 *mg*, 12% yield).

^{1}H NMR (400 MHz, CDCl$_3$) δ: 8.60 (s, 8H, H$_\beta$ pyrrolic), 8.14 – 7.91 (m, 8H, Ar-H), 7.67 – 7.51 (m, 8H, Ar-H), -2.70 (s, 2H, NH).

Synthesis of 2

In a dry two neck round-bottom flask, 250 *mg* of 2-bromo-6-fluorobenzaldehyde (1.23 *mmol*, 1 equivalent) were dissolved, under argon flow, in 125 *mL* of dry CH$_2$Cl$_2$. 85.0 *µL* of freshly distilled pyrrole (1.23 *mmol*, 1 equivalent) were added to the solution. The round bottomed flask was then covered with aluminium foil to protect the reaction from ambient light, and 41.5 *mg* of In(OTf)$_3$ (0.07 *mmol*, 0.06 equivalents) were added to the solution. The reaction was allowed to stir in dark, under argon atmosphere, at RT for 24 hours. After that time the aluminium foil and the argon flow were removed, 167 *mg* of DDQ (0.74 *mmol*, 1.5 equivalents) were added and the reaction was stirred 4 hours at RT exposed to air and ambient light. Finally, 342 *µL* of triethylamine (2.46 *mmol*, 2 equivalent) were added to the solution and let stir for overnight. The crude was retrieved evaporating the solvent *in vacuo*, and the solid obtained was purified by gravimetric chromatography (eluent dichloromethane/n-hexane = 3/1) affording compound **2** as a purple powder (12.5 *mg*, 4% yield).

^{1}H NMR (400 MHz, CDCl$_3$) δ 8.66 (s, 8H, H$_\beta$ *pyrrolic*), 7.80 (m, 4H, Ar-H), 7.61 (m, 4H, Ar-H), 7.46 – 7.40 (m, 4H, Ar-H), -2.70 (s, 2H, NH).

^{19}F NMR (376 MHz, CDCl$_3$) δ -103.44 (m, 4F).

Synthesis of 3

In a dry two neck round-bottom flask, 200 *mg* of 2-bromo-4-fluorobenzaldehyde (0.98 *mmol*, 1 equivalent) were dissolved, under argon flow, in 125 *mL* of dry CH$_2$Cl$_2$. 68.0 *µL* of freshly distilled pyrrole (0.98 *mmol*, 1 equivalent) were added to the solution. The round bottomed flask was then covered with aluminium foil to protect the reaction from ambient light, and 36 *µL* of BF$_3$(OEt)$_2$ (0.29 *mmol*, 0.3 equivalents) were added to the solution. The reaction was allowed to stir in dark, under argon atmosphere, at RT for 16

hours. After that time the aluminium foil and the argon flow were removed, 167 *mg* of DDQ (0.74 *mmol*, 0.75 equivalents) were added and the reaction was stirred 4 hours at RT exposed to air and ambient light. Finally, 137 *μL* of triethylamine (0.98 *mmol*, 1 equivalent) were added to the solution and let stir for 1 hour. The crude was retrieved evaporating the solvent *in vacuo*, and the solid obtained was purified by gravimetric chromatography (eluent dichloromethane/n-hexane = 1/1) affording compound **2** as a purple powder (104 *mg*, 40% yield).

^{1}H NMR (400 MHz, CDCl$_3$) δ 8.60 (s, 8H, H$_\beta$ *pyrrolic*), 8.18 – 7.93 (m, 4H, Ar-H), 7.70 (m, 4H, Ar-H), 7.38 – 7.28 (m, 4H, Ar-H), -2.77 (s, 2H, NH).

^{19}F NMR (376 MHz, CDCl$_3$) δ -111.29 (s, 4F).

Synthesis of 4

In a dry two neck round-bottom flask, 119 *μL* of 2-bromo-4-(trifluoromethyl)benzaldehyde (0.79 *mmol*, 1 equivalent) were dissolved, under argon flow, in 125 *mL* of dry CH$_2$Cl$_2$. 55.0 *μL* of freshly distilled pyrrole (0.79 *mmol*, 1 equivalent) were added to the solution. The round bottomed flask was then covered with aluminium foil to protect the reaction from ambient light, and 36 *μL* of BF$_3$(OEt)$_2$ (0.29 *mmol*, 0.3 equivalents) were added to the solution. The reaction was allowed to stir in dark, under argon atmosphere, at RT for 16 hours. After that time the aluminium foil and the argon flow were removed, 167 *mg* of DDQ (0.74 *mmol*, 0.75 equivalents) were added and the reaction was stirred 4 hours at RT exposed to air and ambient light. Finally, 137 *μL* of triethylamine (0.98 *mmol*, 1 equivalent) were added to the solution and let stir for 1 hour. The crude was retrieved evaporating the solvent *in vacuo*, and the solid obtained was purified by gravimetric chromatography (eluent dichloromethane/n-hexane = 1/1) affording compound **2** as a purple powder (45 *mg*, 19% yield).

^{1}H NMR (400 MHz, CDCl$_3$) δ 8.57 (s, 8H, H$_\beta$ *pyrrolic*), 8.30 – 8.10 (m, 8H, Ar-H), 7.88 (m, 4H, Ar-H), -2.74 (s, 2H, NH).

^{19}F NMR (376 MHz, CDCl$_3$) δ -62.27 (m, 12F).

5.2.7 Synthesis of Iron(III) porphyrins 1-5Fe

In a microwave vessel equipped with a stirring bar, the appropriate free-base porphyrin (1 mmol) was dissolved in dry DMF (5 mL) and Argon was bubbled into the solution. After 5 minutes bubbling, $FeBr_2$ (5 mmol) was added to the solution. The vessel was then sealed and heated under microwave irradiation (150 °C) for 15 *min*. After cooling down at room temperature the DMF solution was added dropwise to 15 mL of a 6M HCl_{aq}, causing the precipitation of the iron chloride porphyrin, which was collected by filtration. The solid was washed first with HCl_{aq} 3M and then several time with water. After carefully drying under vacuum, porphyrin **1Fe**-**5Fe** were collected in almost quantitatively yield as dark brownish solids.

5.3| FABRICATION OF CHEMIRESISTIVE SENSORS

5.3.1 Synthesis of SnO_2 nanoparticles

Tin dioxide nanoparticles were synthesized dissolving 2.93 *g* of $SnCl_4·6H_2O$ into 30 *mL* of MilliQ water and stirred for 3 hours. Concurrently, a solution containing 1.04 *g* of urea in 30 *mL* of water was prepared and transferred into a dropping funnel. The urea solution was added dropwise, taking about 30 minutes. The reaction mixture was then left under stirring for 3 hours, cooled down to room temperature and left to settle overnight. After a night at room temperature the gel was dried in oven at 70 °C for 5 days. A whitish and highly hygroscopic solid was obtained and rapidly calcined in oxidant atmosphere. Finally, a yellow solid was formed due to the decomposition of urea.

5.3.2 Synthesis of SnO_2-porphyrin hybrids

Once prepared the materials, namely SnO_2 and the Zn-tetraphenyl porphyrins, nanocomposites were fabricated by a simple dissolution/deposition method. The appropriate quantity of the different porphyrins were dissolved in 2 mL of dichloromethane and the specific amount of SnO_2 (in order to have 1:4, 1:32 and 1:64 porphyrin/metal oxide weight ratios) was dispersed in such solutions. The obtained mixtures were vigorously stirred for 3 hours at room temperature. Then, the solvent was removed by means of rotary evaporator under atmospheric pressure at 50 °C. The

composites were subsequently collected and kept under vacuum overnight to fully remove solvent residues.

GENERAL CONCLUSIONS AND
FUTURE PERSPECTIVES

In conclusion, my three-year exploration within the realm of porphyrin synthesis has been profoundly fulfilling. Under the guidance of the SunLab group, I've delved into diverse dimensions of porphyrin chemistry and its applications spanning across various disciplines, as elaborated in this thesis. Fundamentally, my PhD journey stands as a testament to the versatility and promise of porphyrins in diverse scientific realms, illustrating their capacity to propel innovation and confront critical challenges in energy, sensing, and materials science.

Acknowledging the "never-ending journey" nature of scientific inquiry, each of the four sections presented herein opens avenues for further investigation and refinement. Notably, ongoing endeavours within SunLab focus on synthesizing new *push-pull* structures crafted to exhibit enhanced charge separation, aiming to yield potentially superior dyes for DSPEC technology. Due to their push-pull structure, these macrocycles could also potentially be of interest for evaluation in the field of nonlinear optics. Furthermore, an expanded exploration into the acetone-sensing mechanism, as elucidated in *Section II*, will incorporate derivatives with pendant groups situated at the β-*pyrrolic* position, as previously discussed in *chapter 2.2*.

These ongoing processes underscore the continuous quest for progress and refinement in our understanding and application of porphyrins as crucial molecules in addressing the challenges of our society.

BIBLIOGRAPHY

1. Imran, M., Ramzan, M., Qureshi, A., Khan, M. & Tariq, M. Emerging Applications of Porphyrins and Metalloporphyrins in Biomedicine and Diagnostic Magnetic Resonance Imaging. *Biosensors (Basel)* **8**, 95 (2018).

2. S. Al Neyadi, S. *et al.* An Undergraduate Experiment Using Microwave-Assisted Synthesis of Metalloporphyrins: Characterization and Spectroscopic Investigations. *World Journal of Chemical Education* **7**, 26–32 (2019).

3. Hiroto, S., Miyake, Y. & Shinokubo, H. Synthesis and Functionalization of Porphyrins through Organometallic Methodologies. *Chem Rev* **117**, 2910–3043 (2017).

4. Gouterman, M. Spectra of porphyrins. *J Mol Spectrosc* **6**, 138–163 (1961).

5. Di Carlo, G., Orbelli Biroli, A., Pizzotti, M. & Tessore, F. Efficient Sunlight Harvesting by A4 β-Pyrrolic Substituted ZnII Porphyrins: A Mini-Review. *Front Chem* **7**, (2019).

6. Tsolekile, N., Nelana, S. & Oluwafemi, O. S. Porphyrin as Diagnostic and Therapeutic Agent. *Molecules* **24**, 2669 (2019).

7. Pargoletti, E., Tessore, F., Carlo, G. Di, Chiarello, G. L. & Cappelletti, G. Towards Low Temperature VOCs Chemoresistors: Graphene Oxide Versus Porphyrin-Based Materials. in *The 1st International Electronic Conference on Chemical Sensors and Analytical Chemistry* 60 (MDPI, Basel Switzerland, 2021). doi:10.3390/CSAC2021-10418.

8. Bonin, J., Chaussemier, M., Robert, M. & Routier, M. Homogeneous Photocatalytic Reduction of CO 2 to CO Using Iron(0) Porphyrin Catalysts: Mechanism and Intrinsic Limitations. *ChemCatChem* **6**, 3200–3207 (2014).

9. Costentin, C., Robert, M. & Savéant, J.-M. Current Issues in Molecular Catalysis Illustrated by Iron Porphyrins as Catalysts of the CO 2 -to-CO Electrochemical Conversion. *Acc Chem Res* **48**, 2996–3006 (2015).

10. Tessore, F., Biroli, A. O., Di Carlo, G. & Pizzotti, M. Porphyrins for second order nonlinear optics (NLO): An intriguing history. *Inorganics* vol. 6 Preprint at https://doi.org/10.3390/inorganics6030081 (2018).

11. Mahmood, A. *et al.* Recent progress in porphyrin-based materials for organic solar cells. *J Mater Chem A Mater* **6**, 16769–16797 (2018).

12. Orbelli Biroli, A. *et al.* Fluorinated Zn II Porphyrins for Dye-Sensitized Aqueous Photoelectrosynthetic Cells. *ACS Appl Mater Interfaces* **11**, 32895–32908 (2019).

13. Mondal, S., Pain, T., Sahu, K. & Kar, S. Large-Scale Green Synthesis of Porphyrins. *ACS Omega* **6**, 22922–22936 (2021).

14. Rothemund, P. A New Porphyrin Synthesis. The Synthesis of Porphin 1. *J Am Chem Soc* **58**, 625–627 (1936).

15. Adler, A. D. *et al.* A simplified synthesis for meso-tetraphenylporphine. *J Org Chem* **32**, 476–476 (1967).

16. Geier III, G. R. & Lindsey, J. S. Investigation of porphyrin-forming reactions. Part 1. Pyrrole + aldehyde oligomerization in two-step, one-flask syntheses of meso-substituted porphyrins †. *Journal of the Chemical Society, Perkin Transactions 2* 677–686 (2001) doi:10.1039/b009088n.

17. Littler, B. J., Ciringh, Y. & Lindsey, J. S. Investigation of Conditions Giving Minimal Scrambling in the Synthesis of trans -Porphyrins from Dipyrromethanes and Aldehydes. *J Org Chem* **64**, 2864–2872 (1999).

18. Arsenault, G. P., Bullock, E. & MacDonald, S. F. Pyrromethanes and Porphyrins Therefrom [1]. *J Am Chem Soc* **82**, 4384–4389 (1960).

19. Koifman, O. I. & Ageeva, T. A. Main Strategies for the Synthesis of meso-Arylporphyrins. *Russian Journal of Organic Chemistry* **58**, 443–479 (2022).

20. IPCC. Climate change widespread, rapid, and intensifying. https://www.ipcc.ch/2021/08/09/ar6-wg1-20210809-pr/.

21. United Nation. What is climate change? https://www.un.org/en/climatechange/what-is-climate-change.

22. European Environment Agency. Environmental impact of energy. https://www.eea.europa.eu/help/glossary/eea-glossary/environmental-impact-of-energy.

23. Armaroli, N. & Balzani, V. Solar Electricity and Solar Fuels: Status and Perspectives in the Context of the Energy Transition. *Chemistry – A European Journal* **22**, 32–57 (2016).

24. IEA. Electricity Information: Overview. *https://www.iea.org/reports/electricity-information-overview* (2021).

25. Hagfeldt, A., Boschloo, G., Sun, L., Kloo, L. & Pettersson, H. Dye-Sensitized Solar Cells. *Chem Rev* **110**, 6595–6663 (2010).

26. Shockley, W. The Theory of p-n Junctions in Semiconductors and p-n Junction Transistors. *Bell System Technical Journal* **28**, 435–489 (1949).

27. O'Regan, B. & Grätzel, M. A low-cost, high-efficiency solar cell based on dye-sensitized colloidal TiO2 films. *Nature* **353**, 737–740 (1991).

28. Instruments, G. DSSC: Dye Sensitized Solar Cells. https://www.gamry.com/application-notes/physechem/dssc-dye-sensitized-solar-cells/.

29. Hara, K. & Arakawa, H. Dye-Sensitized Solar Cells. in *Handbook of Photovoltaic Science and Engineering* 663–700 (Wiley, 2003). doi:10.1002/0470014008.ch15.

30. Brennaman, M. K. *et al.* Finding the Way to Solar Fuels with Dye-Sensitized Photoelectrosynthesis Cells. *J Am Chem Soc* **138**, 13085–13102 (2016).

31. Sapunkov, O., Pande, V., Khetan, A., Choomwattana, C. & Viswanathan, V. Quantifying the promise of 'beyond' Li–ion batteries. *Translational Materials Research* **2**, 045002 (2015).

32. Faunce, T. Towards a Global Solar Fuels Project-Artificial Photosynthesis and the Transition from Anthropocene to Sustainocene. *Procedia Eng* **49**, 348–356 (2012).

33. Yu, Z., Li, F. & Sun, L. Recent advances in dye-sensitized photoelectrochemical cells for solar hydrogen production based on molecular components. *Energy Environ Sci* **8**, 760–775 (2015).

34. FUJISHIMA, A. & HONDA, K. Electrochemical Photolysis of Water at a Semiconductor Electrode. *Nature* **238**, 37–38 (1972).

35. Duan, L., Tong, L., Xu, Y. & Sun, L. Visible light-driven water oxidation—from molecular catalysts to photoelectrochemical cells. *Energy Environ Sci* **4**, 3296 (2011).

36. Young, K. J. *et al.* Light-driven water oxidation for solar fuels. *Coord Chem Rev* **256**, 2503–2520 (2012).

37. Youngblood, W. J. *et al.* Photoassisted Overall Water Splitting in a Visible Light-Absorbing Dye-Sensitized Photoelectrochemical Cell. *J Am Chem Soc* **131**, 926–927 (2009).

38. Mussini, P. R. *et al.* Modulating the electronic properties of asymmetric push–pull and symmetric Zn(II)-diarylporphyrinates with para substituted phenylethynyl moieties in 5,15 meso positions: A combined electrochemical and spectroscopic investigation. *Electrochim Acta* **85**, 509–523 (2012).

39. Di Carlo, G., Biroli, A. O., Tessore, F., Caramori, S. & Pizzotti, M. β-Substituted ZnII porphyrins as dyes for DSSC: A possible approach to photovoltaic windows. *Coord Chem Rev* **358**, 153–177 (2018).

40. Di Carlo, G. *et al.* Tetraaryl Zn II Porphyrinates Substituted at β-Pyrrolic Positions as Sensitizers in Dye-Sensitized Solar Cells: A Comparison with meso -Disubstituted Push-Pull Zn II Porphyrinates. *Chemistry - A European Journal* **19**, 10723–10740 (2013).

41. Lu, F. *et al.* Influence of the additional electron-withdrawing unit in β-functionalized porphyrin sensitizers on the photovoltaic performance of dye-sensitized solar cells. *Dyes and Pigments* **139**, 255–263 (2017).

42. Pan, B., Zhu, Y.-Z., Ye, D. & Zheng, J.-Y. Improved conversion efficiency in dye-sensitized solar cells based on porphyrin dyes with dithieno[3,2-b:2',3'- d]pyrrole donor. *Dyes and Pigments* **150**, 223–230 (2018).

43. Berardi, S. *et al.* Electronic properties of electron-deficient Zn(II) porphyrins for HBr splitting. *Applied Sciences (Switzerland)* **9**, (2019).

44. Covezzi, A. *et al.* 4D–π–1A type β-substituted Zn II -porphyrins: ideal green sensitizers for building-integrated photovoltaics. *Chemical Communications* **52**, 12642–12645 (2016).

45. Materna, K. L. *et al.* Optimization of Photoanodes for Photocatalytic Water Oxidation by Combining a Heterogenized Iridium Water-Oxidation Catalyst with a High-Potential Porphyrin Photosensitizer. *ChemSusChem* **10**, 4526–4534 (2017).

46. Nayak, A. *et al.* Synthesis and photophysical characterization of porphyrin and porphyrin–Ru(ii) polypyridyl chromophore–catalyst assemblies on mesoporous metal oxides. *Chem Sci* **5**, 3115 (2014).

47. Moore, G. F. *et al.* A visible light water-splitting cell with a photoanode formed by codeposition of a high-potential porphyrin and an iridium water-oxidation catalyst. *Energy Environ Sci* **4**, 2389 (2011).

48. Berardi, S. *et al.* Electronic properties of electron-deficient Zn(II) porphyrins for HBr splitting. *Applied Sciences (Switzerland)* **9**, (2019).

49. Marchini, E., Caramori, S. & Carli, S. Metal Complexes for Dye-Sensitized Photoelectrochemical Cells (DSPECs). *Molecules* **29**, 293 (2024).

50. Mei, B., Mul, G. & Seger, B. Beyond Water Splitting: Efficiencies of Photo-Electrochemical Devices Producing Hydrogen and Valuable Oxidation Products. *Adv Sustain Syst* **1**, (2017).

51. Livshits, V., Ulus, A. & Peled, E. High-power H2/Br2 fuel cell. *Electrochem commun* **8**, 1358–1362 (2006).

52. Lee, C. *et al.* Novel Zinc Porphyrin Sensitizers for Dye-Sensitized Solar Cells: Synthesis and Spectral, Electrochemical, and Photovoltaic Properties. *Chemistry – A European Journal* **15**, 1403–1412 (2009).

53. Huang, C. *et al.* A Systematic Study of Electrochemical and Spectral Properties for the Electronic Interactions in Porphyrin–Triphenylamine Conjugates. *Eur J Inorg Chem* **2012**, 1038–1047 (2012).

54. Liang, L. & Astruc, D. The copper(I)-catalyzed alkyne-azide cycloaddition (CuAAC) "click" reaction and its applications. An overview. *Coord Chem Rev* **255**, 2933–2945 (2011).

55. Fresta, E. *et al.* BODIPY-Pt-Porphyrins Polyads for Efficient Near-Infrared Light-Emitting Electrochemical Cells. *Adv Photonics Res* **2**, (2021).

56. Damiano, C. *et al.* Iron and Ruthenium Glycoporphyrins: Active Catalysts for the Synthesis of Cyclopropanes and Aziridines. *Eur J Inorg Chem* **2019**, 4412–4420 (2019).

57. van Beurden, K., de Koning, S., Molendijk, D. & van Schijndel, J. The Knoevenagel reaction: a review of the unfinished treasure map to forming carbon–carbon bonds. *Green Chem Lett Rev* **13**, 349–364 (2020).

58. Pawar, H. S., Wagh, A. S. & Lali, A. M. Triethylamine: a potential N-base surrogate for pyridine in Knoevenagel condensation of aromatic aldehydes and malonic acid. *New Journal of Chemistry* **40**, 4962–4968 (2016).

59. Kadish, K. M., Han, B. C., Franzen, M. M. & Araullo-McAdams, C. Syntheses and spectroscopic characterization of (T(p-Me2N)F4PP)H2 and (T(p-Me2N)F4PP)M where T(p-Me2N)F4PP = the dianion of meso-tetrakis(o,o,m,m-tetrafluoro-p-(dimethylamino)phenyl)porphyrin and M = cobalt(II), copper(II), or nickel(II). Structures of (T. *J Am Chem Soc* **112**, 8364–8368 (1990).

60. Bajju, G. D. & Singh, N. Synthesis and Characterization of New Meso-Substituted and β-Substituted Unsymmetrical Metalloporphyrins. *Chem Sci Trans* **3**, 314–322 (2014).

61. Golf, H. R. A., Reissig, H.-U. & Wiehe, A. Regioselective Nucleophilic Aromatic Substitution Reaction of meso -Pentafluorophenyl-Substituted Porphyrinoids with Alcohols. *European J Org Chem* **2015**, 1548–1568 (2015).

62. Di Carlo, G. *et al.* Light-Induced Regiospecific Bromination of *meso* -Tetra(3,5-di- *tert* - butylphenyl)Porphyrin on 2,12 β-Pyrrolic Positions. *J Org Chem* **80**, 4973–4980 (2015).

63. Nikoloudakis, E. *et al.* Dye-Sensitized Photoelectrosynthesis Cells for Benzyl Alcohol Oxidation Using a Zinc Porphyrin Sensitizer and TEMPO Catalyst. *ACS Catal* **11**, 12075–12086 (2021).

64. *Volatile Organic Compounds in the Atmosphere*. (Wiley, 2007). doi:10.1002/9780470988657.

65. D.Lgs 3 aprile 2006 n.152. Norme in Materia Ambientale. Gazz. Uff. 2006, 1 (c), 172. Preprint at (2006).

66. Kamal, M. S., Razzak, S. A. & Hossain, M. M. Catalytic oxidation of volatile organic compounds (VOCs) – A review. *Atmos Environ* **140**, 117–134 (2016).

67. Ren, F. *et al.* Enhanced BTEX gas-sensing performance of CuO/SnO 2 composite. *Sens Actuators B Chem* **223**, 914–920 (2016).

68. Guo, Y., Wen, M., Li, G. & An, T. Recent advances in VOC elimination by catalytic oxidation technology onto various nanoparticles catalysts: a critical review. *Appl Catal B* **281**, 119447 (2021).

69. Lee, J. H. ;, Hwang, S. M. ;, Lee, D. W. ; & Heo, G. S. Determination of Volatile Organic Compounds (VOCs) Using Tedlar Bag/Solid-phase Microextraction/Gas Chromatography/Mass Spectrometry (SPME/GC/MS) in Ambient and Workplace Air. *Bull Korean Chem Soc* **23**, 488–496 (2002).

70. Pargoletti, E., Tessore, F., Carlo, G. Di, Chiarello, G. L. & Cappelletti, G. Towards Low Temperature VOCs Chemoresistors: Graphene Oxide Versus Porphyrin-Based Materials. in *The 1st International Electronic Conference on Chemical Sensors and Analytical Chemistry* 60 (MDPI, Basel Switzerland, 2021). doi:10.3390/CSAC2021-10418.

71. Saasa, V. *et al.* Sensing Technologies for Detection of Acetone in Human Breath for Diabetes Diagnosis and Monitoring. *Diagnostics* **8**, 12 (2018).

72. Sethi, S., Nanda, R. & Chakraborty, T. Clinical Application of Volatile Organic Compound Analysis for Detecting Infectious Diseases. *Clin Microbiol Rev* **26**, 462–475 (2013).

73. Tricoli, A., Nasiri, N. & De, S. Wearable and Miniaturized Sensor Technologies for Personalized and Preventive Medicine. *Adv Funct Mater* **27**, (2017).

74. Güntner, A. T., Koren, V., Chikkadi, K., Righettoni, M. & Pratsinis, S. E. E-Nose Sensing of Low-ppb Formaldehyde in Gas Mixtures at High Relative Humidity for Breath Screening of Lung Cancer? *ACS Sens* **1**, 528–535 (2016).

75. Pargoletti, E. *et al.* Engineering of SnO 2 –Graphene Oxide Nanoheterojunctions for Selective Room-Temperature Chemical Sensing and Optoelectronic Devices. *ACS Appl Mater Interfaces* **12**, 39549–39560 (2020).

76. Neri, G. First Fifty Years of Chemoresistive Gas Sensors. *Chemosensors* **3**, 1–20 (2015).

77. Quaranta, F. *et al.* Preparation and characterization of nanostructured materials for an artificial olfactory sensing system. *Sens Actuators B Chem* **84**, 55–59 (2002).

78. Varghese, S. S., Lonkar, S., Singh, K. K., Swaminathan, S. & Abdala, A. Recent advances in graphene based gas sensors. *Sens Actuators B Chem* **218**, 160–183 (2015).

79. Kaur, N., Singh, M. & Comini, E. One-Dimensional Nanostructured Oxide Chemoresistive Sensors. *Langmuir* **36**, 6326–6344 (2020).

80. Wei, Q., Sun, J., Song, P., Yang, Z. & Wang, Q. Synthesis of reduced graphene oxide/SnO2 nanosheets/Au nanoparticles ternary composites with enhanced formaldehyde sensing performance. *Physica E Low Dimens Syst Nanostruct* **118**, 113953 (2020).

81. Morsy, M., Yahia, I. S., Zahran, H. Y., Meng, F. & Ibrahim, M. Portable and Battery Operated Ammonia Gas Sensor Based on CNTs/rGO/ZnO Nanocomposite. *J Electron Mater* **48**, 7328–7335 (2019).

82. van den Broek, J., Abegg, S., Pratsinis, S. E. & Güntner, A. T. Highly selective detection of methanol over ethanol by a handheld gas sensor. *Nat Commun* **10**, 4220 (2019).

83. Pineau, N. J., Kompalla, J. F., Güntner, A. T. & Pratsinis, S. E. Orthogonal gas sensor arrays by chemoresistive material design. *Microchimica Acta* **185**, 563 (2018).

84. Tricoli, A., Righettoni, M. & Teleki, A. Semiconductor Gas Sensors: Dry Synthesis and Application. *Angewandte Chemie International Edition* **49**, 7632–7659 (2010).

85. Georgakilas, V. *et al.* Functionalization of Graphene: Covalent and Non-Covalent Approaches, Derivatives and Applications. *Chem Rev* **112**, 6156–6214 (2012).

86. Belkova, G. V. *et al.* The character of the response of ZnO and SnO2 sensors modified with porphyrins to volatile organic compounds. *Russian Journal of Physical Chemistry A* **82**, 2323–2328 (2008).

87. Paolesse, R., Nardis, S., Monti, D., Stefanelli, M. & Di Natale, C. Porphyrinoids for Chemical Sensor Applications. *Chem Rev* **117**, 2517–2583 (2017).

88. Erdélyi, M. & Gogoll, A. Rapid Homogeneous-Phase Sonogashira Coupling Reactions Using Controlled Microwave Heating. *J Org Chem* **66**, 4165–4169 (2001).

89. Anjali, K., Nishana, L. K., Christopher, J. & Sakthivel, A. Zinc-tetraphenylporphyrin grafted on functionalised mesoporous SBA-15: synthesis and utilisation for nitroaldol condensation. *Journal of Porous Materials* **27**, 1191–1201 (2020).

90. Americo, S. *et al.* Unveiling the acetone sensing mechanism by WO3 chemiresistors through a joint theory-experiment approach. *Electrochim Acta* **371**, 137611 (2021).

91. Sopiha, K. V., Malyi, O. I., Persson, C. & Wu, P. Chemistry of Oxygen Ionosorption on SnO 2 Surfaces. *ACS Appl Mater Interfaces* **13**, 33664–33676 (2021).

92. Cox, D. F., Fryberger, T. B. & Semancik, S. Oxygen vacancies and defect electronic states on the SnO2(110)- 1×1 surface. *Phys Rev B* **38**, 2072–2083 (1988).

93. Ritchie, H., Roser, M. & Rosando, P. CO₂ and Greenhouse Gas Emissions. *Our World in Data* (2020).

94. What is carbon neutrality and how can it be achieved by 2050? *News European Parliament*.

95. Jouny, M., Hutchings, G. S. & Jiao, F. Carbon monoxide electroreduction as an emerging platform for carbon utilization. *Nat Catal* **2**, 1062–1070 (2019).

96. Chen, Q., Tsiakaras, P. & Shen, P. Electrochemical Reduction of Carbon Dioxide: Recent Advances on Au-Based Nanocatalysts. *Catalysts* **12**, 1348 (2022).

97. Li, Y. C. *et al.* CO2 Electroreduction from Carbonate Electrolyte. *ACS Energy Lett* **4**, 1427–1431 (2019).

98. Liu, Z., Yang, H., Kutz, R. & Masel, R. I. CO2 Electrolysis to CO and O2 at High Selectivity, Stability and Efficiency Using Sustainion Membranes. *J Electrochem Soc* **165**, J3371–J3377 (2018).

99. Dinh, C.-T., García de Arquer, F. P., Sinton, D. & Sargent, E. H. High Rate, Selective, and Stable Electroreduction of CO 2 to CO in Basic and Neutral Media. *ACS Energy Lett* **3**, 2835–2840 (2018).

100. Bierhals, J. Carbon Monoxide. in *Ullmann's Encyclopedia of Industrial Chemistry* (Wiley, 2001). doi:10.1002/14356007.a05_203.

101. Nichols, E. M., Derrick, J. S., Nistanaki, S. K., Smith, P. T. & Chang, C. J. Positional effects of second-sphere amide pendants on electrochemical CO2 reduction catalyzed by iron porphyrins. *Chem Sci* **9**, 2952–2960 (2018).

102. Ishida, H. Electrochemical/Photochemical CO2 Reduction Catalyzed by Transition Metal Complexes. in *Carbon Dioxide Chemistry, Capture and Oil Recovery* (InTech, 2018). doi:10.5772/intechopen.75199.

103. Takeda, H., Cometto, C., Ishitani, O. & Robert, M. Electrons, Photons, Protons and Earth-Abundant Metal Complexes for Molecular Catalysis of CO 2 Reduction. *ACS Catal* **7**, 70–88 (2017).

104. Fukatsu, A., Kondo, M., Okabe, Y. & Masaoka, S. Electrochemical analysis of iron-porphyrin-catalyzed CO2 reduction under photoirradiation. *J Photochem Photobiol A Chem* **313**, 143–148 (2015).

105. Cui, X. & Zhang, X. P. Iron(III) meso -Tetraphenylporphine Chloride. in *Encyclopedia of Reagents for Organic Synthesis* (John Wiley & Sons, Ltd, Chichester, UK, 2012). doi:10.1002/047084289X.rn01388.

106. Gotico, P., Halime, Z. & Aukauloo, A. Recent advances in metalloporphyrin-based catalyst design towards carbon dioxide reduction: from bio-inspired second coordination sphere modifications to hierarchical architectures. *Dalton Transactions* **49**, 2381–2396 (2020).

107. Bonin, J., Maurin, A. & Robert, M. Molecular catalysis of the electrochemical and photochemical reduction of CO2 with Fe and Co metal based complexes. Recent advances. *Coord Chem Rev* **334**, 184–198 (2017).

108. Sen, P., Mondal, B., Saha, D., Rana, A. & Dey, A. Role of 2nd sphere H-bonding residues in tuning the kinetics of CO2 reduction to CO by iron porphyrin complexes. *Dalton Transactions* **48**, 5965–5977 (2019).

109. Williams, C. K., Lashgari, A., Tomb, J. A., Chai, J. & Jiang, J. J. Atropisomeric Effects of Second Coordination Spheres on Electrocatalytic CO 2 Reduction. *ChemCatChem* **12**, 4886–4892 (2020).

110. Gotico, P. *et al.* Second-Sphere Biomimetic Multipoint Hydrogen-Bonding Patterns to Boost CO 2 Reduction of Iron Porphyrins. *Angewandte Chemie International Edition* **58**, 4504–4509 (2019).

111. Azcarate, I., Costentin, C., Robert, M. & Savéant, J.-M. Through-Space Charge Interaction Substituent Effects in Molecular Catalysis Leading to the Design of the Most Efficient Catalyst of CO 2 -to-CO Electrochemical Conversion. *J Am Chem Soc* **138**, 16639–16644 (2016).

112. Bonin, J., Robert, M. & Routier, M. Selective and Efficient Photocatalytic CO 2 Reduction to CO Using Visible Light and an Iron-Based Homogeneous Catalyst. *J Am Chem Soc* **136**, 16768–16771 (2014).

113. Costa, P. J. The halogen bond: Nature and applications. *Physical Sciences Reviews* **2**, (2017).

114. Clark, T., Hennemann, M., Murray, J. S. & Politzer, P. Halogen bonding: the σ-hole. *J Mol Model* **13**, 291–296 (2007).

115. Scholfield, M. R., Zanden, C. M. Vander, Carter, M. & Ho, P. S. Halogen bonding (X-bonding): A biological perspective. *Protein Science* **22**, 139–152 (2013).

116. Wilcken, R., Zimmermann, M. O., Lange, A., Joerger, A. C. & Boeckler, F. M. Principles and Applications of Halogen Bonding in Medicinal Chemistry and Chemical Biology. *J Med Chem* **56**, 1363–1388 (2013).

117. Fave, C. & Schöllhorn, B. Electrochemical activation of halogen bonding. *Curr Opin Electrochem* **15**, 89–96 (2019).

118. Sutar, R. L. & Huber, S. M. Catalysis of Organic Reactions through Halogen Bonding. *ACS Catal* **9**, 9622–9639 (2019).

119. Azcarate, I., Costentin, C., Robert, M. & Savéant, J. M. Through-Space Charge Interaction Substituent Effects in Molecular Catalysis Leading to the Design of the Most Efficient Catalyst of CO2-to-CO Electrochemical Conversion. *J Am Chem Soc* **138**, 16639–16644 (2016).

120. Azcarate, I., Costentin, C., Robert, M. & Savéant, J.-M. Dissection of Electronic Substituent Effects in Multielectron–Multistep Molecular Catalysis. Electrochemical CO 2 -to-CO Conversion Catalyzed by Iron Porphyrins. *The Journal of Physical Chemistry C* **120**, 28951–28960 (2016).

121. Costentin, C., Robert, M. & Savéant, J.-M. Current Issues in Molecular Catalysis Illustrated by Iron Porphyrins as Catalysts of the CO 2 -to-CO Electrochemical Conversion. *Acc Chem Res* **48**, 2996–3006 (2015).

122. Engelage, E. *et al.* Towards redox-switchable organocatalysts based on bidentate halogen bond donors. *Physical Chemistry Chemical Physics* **23**, 4344–4352 (2021).

123. de F. Castro, K. A. D. *et al.* Synthesis of new metalloporphyrin derivatives from [5,10,15,20-tetrakis (pentafluorophenyl)porphyrin] and 4-mercaptobenzoic acid for homogeneous and heterogeneous catalysis. *Appl Catal A Gen* **503**, 9–19 (2015).

124. Orbelli Biroli, A. *et al.* Highly improved performance of Zn II tetraarylporphyrinates in DSSCs by the presence of octyloxy chains in the aryl rings. *J Mater Chem A Mater* **3**, 2954–2959 (2015).

125. Combellas, C. & Kanoufi, F. Reducibility of the carbon-fluorine bond in the trifluoromethyl group. *journal of electroanalytical Chemistry* **407**, 195–202 (1996).

126. Costentin, C., Drouet, S., Passard, G., Robert, M. & Savéant, J.-M. Proton-Coupled Electron Transfer Cleavage of Heavy-Atom Bonds in Electrocatalytic Processes. Cleavage of a C–O Bond in the Catalyzed Electrochemical Reduction of CO $_2$. *J Am Chem Soc* **135**, 9023–9031 (2013).

127. Costentin, C. & Savéant, J.-M. Heterogeneous Molecular Catalysis of Electrochemical Reactions: Volcano Plots and Catalytic Tafel Plots. *ACS Appl Mater Interfaces* **9**, 19894–19899 (2017).

128. Di Bella, S. *et al.* Coordination and Organometallic Complexes as Second-Order Nonlinear Optical Molecular Materials. in 1–55 (2010). doi:10.1007/978-3-642-01866-4_1.

129. Lecours, S. M., Guan, H.-W., Dimagno, S. G., Wang, C. H. & Therien, M. J. *Push-Pull Arylethynyl Porphyrins: New Chromophores That Exhibit Large Molecular First-Order Hyperpolarizabilities*. https://pubs.acs.org/sharingguidelines (1996).

130. Karki, L., Vance, F. W., Hupp, J. T., Lecours, S. M. & Therien, M. J. *Electronic Stark Effect Studies of a Porphyrin-Based Push-Pull Chromophore Displaying a Large First Hyperpolarizability: State-Specific Contributions To*. https://pubs.acs.org/sharingguidelines (1998).

131. Bruni, S. *et al.* Determination of the quadratic hyperpolarizability of trans-4-[4-(dimethylamino)styryl]pyridine and 5-dimethylamino-1,10-phenanthroline from solvatochromism of absorption and fluorescence spectra: a comparison with the electric-field-induced second-harmonic generation technique. *Spectrochim Acta A Mol Biomol Spectrosc* **57**, 1417–1426 (2001).

132. Pizzotti, M. *et al.* A multitechnique investigation of the second order NLO response of a 10,20-diphenylporphyrinato nickel(II) complex carrying a phenylethynyl based push-pull system in the 5- and 15-positions. *J Porphyr Phthalocyanines* **08**, 1311–1324 (2004).

133. Suslick, K. S., Chen, C. T., Meredith, G. R. & Cheng, L. T. Push-pull porphyrins as nonlinear optical materials. *J Am Chem Soc* **114**, 6928–6930 (1992).

134. Pizzotti, M. *et al.* A critical evaluation of EFISH and THG non-linear optical responses of asymmetrically substituted meso-tetraphenyl porphyrins and their metal complexes. *Inorganica Chim Acta* **340**, 70–80 (2002).

135. Yeung, M. *et al.* Facile Synthesis and Nonlinear Optical Properties of Push–Pull 5,15-Diphenylporphyrins. *J Org Chem* **63**, 7143–7150 (1998).

136. Levine, B. F. & Bethea, C. G. Molecular hyperpolarizabilities determined from conjugated and nonconjugated organic liquids. *Appl Phys Lett* **24**, 445–447 (1974).

137. Rojo, G. *et al.* Novel unsymmetrically substituted push–pull phthalocyanines for second-order nonlinear optics. *Chem Phys* **245**, 27–34 (1999).

138. Ledoux, I. & Zyss, J. Influence of the molecular environment in solution measurements of the Second-order optical susceptibility for urea and derivatives. *Chem Phys* **73**, 203–213 (1982).

139. Dworczak, R. & Kieslinger, D. Electric field induced second harmonic generation (EFISH) experiments in the swivel cell: New aspects of an established method. *Physical Chemistry Chemical Physics* **2**, 5057–5064 (2000).

140. Oudar, J. L. Optical nonlinearities of conjugated molecules. Stilbene derivatives and highly polar aromatic compounds. *J Chem Phys* **67**, 446–457 (1977).

141. Boyd, R. W. & Fischer, G. L. Nonlinear Optical Materials. in *Encyclopedia of Materials: Science and Technology* 6237–6244 (Elsevier, 2001). doi:10.1016/B0-08-043152-6/01107-4.

142. PRASAD, P. N. & WILLIAMS DAVID J. Origin of Microscopic Nonlinearity in Organic Systems . in *INTRODUCTION TO NONLINEAR OPTICAL EFFECTS IN MOLECULES AND POLYMERS* 35–58.

143. Limosani, F. *et al.* Designing Cascades of Electron Transfer Processes in Multicomponent Graphene Conjugates. *Angewandte Chemie International Edition* **59**, 23706–23715 (2020).

144. Xu, Y. *et al.* A Graphene Hybrid Material Covalently Functionalized with Porphyrin: Synthesis and Optical Limiting Property. *Advanced Materials* **21**, 1275–1279 (2009).

145. Flavin, K., Chaur, M. N., Echegoyen, L. & Giordani, S. Functionalization of Multilayer Fullerenes (Carbon Nano-Onions) using Diazonium Compounds and "Click" Chemistry. *Org Lett* **12**, 840–843 (2010).

146.   Imahori, H. *et al.* Long-Lived Charge-Separated State Generated in a Ferrocene– *meso* , *meso* - Linked Porphyrin Trimer–Fullerene Pentad with a High Quantum Yield. *Chemistry – A European Journal* **10**, 3184–3196 (2004).

147.   Limosani, F., Tessore, F., Di Carlo, G., Forni, A. & Tagliatesta, P. Nonlinear Optical Properties of Porphyrin, Fullerene and Ferrocene Hybrid Materials. *Materials* **14**, 4404 (2021).

148.   Maggini, M., Scorrano, G. & Prato, M. Addition of azomethine ylides to C60: synthesis, characterization, and functionalization of fullerene pyrrolidines. *J Am Chem Soc* **115**, 9798–9799 (1993).

149.   Pierantoni, L. *et al.* Broadband Microwave Attenuator Based on Few Layer Graphene Flakes. *IEEE Trans Microw Theory Tech* **63**, 2491–2497 (2015).

150.   Di Carlo, G., Pizzotti, M., Righetto, S., Forni, A. & Tessore, F. Electric-Field-Induced Second Harmonic Generation Nonlinear Optic Response of A4 β-Pyrrolic-Substituted ZnII Porphyrins: When Cubic Contributions Cannot Be Neglected. *Inorg Chem* **59**, 7561–7570 (2020).

151.   Albert, I. D. L., Marks, T. J. & Ratner, M. A. Large Molecular Hyperpolarizabilities in "Push–Pull" Porphyrins. Molecular Planarity and Auxiliary Donor–Acceptor Effects. *Chemistry of Materials* **10**, 753–762 (1998).

152.   Pizzotti, M. *et al.* An EFISH, Theoretical, and PGSE NMR Investigation on the Relevant Role of Aggregation on the Second Order Response in CHCl $_3$ of the Push–Pull Chromophores [5-[[4'-(Dimethylamino)phenyl]ethynyl]-15-[(4''-nitrophenyl)ethynyl]-10,20-diphenylporphyrinate] M(II) (M = Zn, Ni). *The Journal of Physical Chemistry C* **113**, 11131–11141 (2009).

153.   Orbelli Biroli, A. *et al.* Intriguing Influence of −COOH-Driven Intermolecular Aggregation and Acid–Base Interactions with *N* , *N* -Dimethylformamide on the Second-Order Nonlinear-Optical Response of 5,15 Push–Pull Diarylzinc(II) Porphyrinates. *Inorg Chem* **56**, 6438–6450 (2017).

154.   Planells, M., Pizzotti, M., Nichol, G. S., Tessore, F. & Robertson, N. Effect of torsional twist on 2nd order non-linear optical activity of anthracene and pyrene tricyanofuran derivatives. *Phys. Chem. Chem. Phys.* **16**, 23404–23411 (2014).

155.   Limosani, F. *et al.* Nonlinear Optical Properties of Zn(II) Porphyrin, Graphene Nanoplates, and Ferrocene Hybrid Materials. *Materials* **16**, 5427 (2023).

156.   Bard, Faulkner & White. *Electrochemical Methods: Fundamentals and Applications*. (2022).

157.   Costentin, C., Drouet, S., Robert, M. & Savéant, J.-M. Turnover Numbers, Turnover Frequencies, and Overpotential in Molecular Catalysis of Electrochemical Reactions. Cyclic Voltammetry and Preparative-Scale Electrolysis. *J Am Chem Soc* **134**, 11235–11242 (2012).

158.   Pargoletti, E. *et al.* Room-temperature photodetectors and VOC sensors based on graphene oxide-ZnO nano-heterojunctions. *Nanoscale* **11**, (2019).

159.   Americo, S. *et al.* Unveiling the acetone sensing mechanism by WO_3 chemiresistors through a joint theory-experiment approach. *Electrochim Acta* **371**, (2021).

160.   Frisch, M. J. & et all. Gaussian 09, Revision A.02; Preprint at (2009).

161.   Klamt, A., Moya, C. & Palomar, J. A Comprehensive Comparison of the IEFPCM and SS(V)PE Continuum Solvation Methods with the COSMO Approach. *J Chem Theory Comput* **11**, 4220–4225 (2015).

162.   Morello, G. R. Accurate prediction of emission energies with TD-DFT methods for platinum and iridium OLED materials. *J Mol Model* **23**, 174 (2017).

163.   Lu, T. & Chen, F. Multiwfn: A multifunctional wavefunction analyzer. *J Comput Chem* **33**, 580–592 (2012).

164.   Troullier, N. & Martins, J. L. Efficient pseudopotentials for plane-wave calculations. *Phys Rev B* **43**, 1993–2006 (1991).

165.   Ferreira, L. G., Marques, M. & Teles, L. K. Approximation to density functional theory for the calculation of band gaps of semiconductors. *Phys Rev B* **78**, 125116 (2008).

166. Ferreira, L. G., Marques, M. & Teles, L. K. Slater half-occupation technique revisited: the LDA-1/2 and GGA-1/2 approaches for atomic ionization energies and band gaps in semiconductors. *AIP Adv* **1**, 32119 (2011).

167. Zhou, W., Liu, Y., Yang, Y. & Wu, P. Band Gap Engineering of SnO 2 by Epitaxial Strain: Experimental and Theoretical Investigations. *The Journal of Physical Chemistry C* **118**, 6448–6453 (2014).

168. Grimme, S., Ehrlich, S. & Goerigk, L. Effect of the damping function in dispersion corrected density functional theory. *J Comput Chem* **32**, 1456–1465 (2011).

169. Weigend, F. & Ahlrichs, R. Balanced basis sets of split valence, triple zeta valence and quadruple zeta valence quality for H to Rn: Design and assessment of accuracy. *Physical Chemistry Chemical Physics* **7**, 3297 (2005).

170. Weigend, F. Accurate Coulomb-fitting basis sets for H to Rn. *Physical Chemistry Chemical Physics* **8**, 1057 (2006).

171. Scalmani, G. & Frisch, M. J. Continuous surface charge polarizable continuum models of solvation. I. General formalism. *J Chem Phys* **132**, (2010).

172. de Wergifosse, M. & Champagne, B. Electron correlation effects on the first hyperpolarizability of push–pull π-conjugated systems. *J Chem Phys* **134**, (2011).

173. Kurtz, H. A. & Dudis, D. S. Quantum Mechanical Methods for Predicting Nonlinear Optical Properties. in 241–279 (1998). doi:10.1002/9780470125892.ch5.

174. Willetts, A., Rice, J. E., Burland, D. M. & Shelton, D. P. Problems in the comparison of theoretical and experimental hyperpolarizabilities. *J Chem Phys* **97**, 7590–7599 (1992).

RINGRAZIAMENTI

Un percorso di tre anni, così intenso e sfaccettato richiederebbe un capitolo intero per ringraziare singolarmente tutte le persone che hanno contribuito in vario modo alla sua realizzazione. Iniziando con ordine, un sincero grazie va alla professoressa La Rosa, per essere stata un prezioso tramite e per avermi incoraggiata ad intraprendere questa avventura.

Subito dopo, ovviamente, vanno menzionati i miei tutor: la professoressa F. Tessore e il professor G. Di Carlo, che, se fossero stati due tutor ordinari, i ringraziamenti potrebbero anche fermarsi qua. Invece, è difficile trovare le parole giuste per esprimere la mia gratitudine per aver reso questi tre anni un'occasione fantastica di crescita e di apprendimento. Grazie Francesca per essere stata un riferimento e un esempio, per aver dimostrato sempre grande apertura mentale, fantastica ironia e per lo spirito positivo con cui mi hai insegnato ad affrontare ogni giorno, lavorativo ma non solo. Grazie Gabriele per la dimostrazione quotidiana di quanta passione si possa mettere nel proprio lavoro; grazie per la bella musica in laboratorio e per i caffè al lampone. Un grazie speciale va al mio collega di dottorato Manuel: fin dal suo arrivo compagno di ogni esperienza, dalle sintesi non riuscite, ai danni nascosti (scusa Gabri), fino alle pause caffè a parlare di arrampicata, fisica quantistica o cibo, passando per i lunghi pomeriggi di sfaso a gridare sottovoce "ce la faremooo!". Infine, il gruppo SunLab non sarebbe tale senza tutti gli studenti che sono passati nei suoi laboratori, quindi un grazie immenso va a: Claudia, Giuditta, Gabriele, Maura, Giovanni, Lorenzo T., Riccardo, Matteo, Lorenzo R., Francesco A., Paolo e Simone. Nei mesi che abbiamo passato insieme spero di aver insegnato qualcosina a ciascuno di voi, ma vi assicuro che non è nulla rispetto a quello che voi avete insegnato a me.

Doveroso un ringraziamento a tutti i vicini di casa che hanno reso il "Primo Piano - Corpo A" un posticino magico, quindi grazie a Francesco (dottorando, ormai post-doc, in affido), Alessandro, Silvio, Stefano, Elisa, Luca, per tutte le pause pranzo in Malatesta, le birrette e gli aperitivi, le pizze da 85 con la successiva condivisione dello stato comatoso pomeridiano che ne deriva.

Un grand merci va à la "famille française". Les six mois que j'ai passés à Paris ont été une occasion unique et spéciale d'apprentissage et de découverte, donc merci au professeur Robert, à la docteure Fave et aux professeurs Anxolabéhère-Mallart, Bonin et Schollhorn. Mais si je me souviens de ces mois avec tant de plaisir, c'est grâce à mes collègues que j'ai trouvés là-bas. Donc merci à Lauriane pour avoir travaillé côte à côte avec moi, merci à Shiem et Ester pour vos sourires et votre gentillesse. Un immense merci à Francesco,